Alma Mater Studiorum · Università di Bologna

Scuola di Scienze
Dipartimento di Fisica e Astronomia
Corso di Laurea Magistrale in Fisica

The Cosmic Ray Tagger of the Short Baseline Neutrino experiment at Fermilab

Relatore:
Prof. Sergio Bertolucci

Correlatori:
Dott. Alessandro Montanari
Dott.ssa Laura Pasqualini

Presentata da:
Francesco Poppi

Anno Accademico 2018/2019

Abstract

The Short Baseline Neutrino (SBN) program at Fermilab will search for new physics in the neutrino oscillations parameters. The far detector will be interested by a ∼25 kHz rate of cosmic ray events. An external cosmic ray tagging system will be implemented in order to prevent possible misidentification in the liquid argon time projection chamber.
This thesis is focused on the activities performed on the top cosmic ray tagging modules of the SBN experiment. The front-end electronics and the data acquisition software were tested and debugged. The performance evaluation techniques were first developed on the prototype module in Bologna and then applied to the assembled modules at the Frascati National Laboratories.

Sommario

Il programma di ricerca sulle oscillazioni di neutrini in esperimenti a *Short-Baseline* a Fermilab (*SBN*) permetterà di trovare possibili evidenze di nuova fisica nei parametri di oscillazione dei neutrini. Il *Far detector* sarà interessato da un rate di raggi cosmici di $\sim$25 kHz, un sistema esterno di identificazione dei raggi cosmici (*CRT*) verrà implementato per prevenire possibili misidentificazioni nella *time projection chamber* ad argon liquido.
Questa tesi è incentrata sulle attività compiute sui moduli per l'identificazione dei raggi cosmici dell'esperimento SBN a Fermilab. Gli studi iniziali sono stati effettuati sull'elettronica di front end e sul software di acquisizione dati. Le metodologie di valutazione sono state prima sviluppate sul prototipo costruito nei laboratori di Bologna (Modulo 0) e poi applicate sui moduli assemblati presso i Laboratori Nazionali di Frascati.

Contents

Introduction

The *Short-Baseline Neutrino* program (SBN) was proposed to confirm or rule out the hypothesis of sterile neutrinos at eV mass scale, whose existence was hinted by several experimental anomalies found in neutrino oscillation experiments. The experiment consists of three *Liquid Argon Time Projection Chambers* (LArTPCs) detectors located along the *Booster Neutrino Beam* (BNB) at Fermilab. The far detector, ICARUS-T600, will be located 600 m from the beam target at ground level. The LArTPC will be exposed to a rate of $\sim$25 kHz of cosmic muons and, due to 1 ms TPC readout, on average 11 cosmic rays tracks are expected over the full T600 in coincidence of every 1.6 μs beam trigger window. In order to prevent possible misidentification in the event reconstruction, an external *Cosmic Ray Tagging* (CRT) system will identify the cosmic events entering the TPC. The CRT system will provide a 4π coverage of the detector an it is divided in three subsystems (Bottom, Lateral and Top).

In this thesis I was deeply involved on the design, assembling and characterisation of the top modules of the CRT system. A module is composed of two orthogonal layers of scintillator bars of different thicknesses. Wavelength-shifting fibres (WLS) are embedded along the longitudinal direction of the scintillator bars, in order to collect the scintillation light and guide it to the silicon-photomultipliers (SiPMs). A timing resolution test of the front-end board was carried out. The characterisation of the modules was performed in terms of light yield and efficiency measurements.
This thesis is organized as follows: in Chapter 1 an introduction to neutrino oscillation physics is provided with special attention to the anomalies observed in some experiments. The Short-Baseline Neutrino program at Fermilab is introduced in Chapter 2, along with a brief description of the LArTPCs and an analysis of the cosmogenic background at the Far site. In Chapter 3 the top CRT system of the ICARUS-T600 Far detector is described. The results of the detector timing resolution are reported in Chapter 4 along with the light yield measurements performed on the CRT Module 0 and on a module assembled at the Frascati National Laboratories. Efficiency measurements are discussed in Chapter 5.

Chapter 1

Introduction to neutrino oscillations

1.1 Neutrino introduction

Modern physics was born at the beginning of the 20th century, when the advent of quantum mechanics and special relativity allowed the transition towards a new paradigm. This new approach to physics provided a description of "catastrophic" events not included in the classical model as such as photoelectric effects and the black-body radiation. The first particles discovered were the electron by Thompson in 1897 [1] and the proton by Rutherford in 1918 [2]. According to the Rutherford atomic model, presented in 1911, the atom consists in a cluster of protons surrounded by a cloud of orbiting electrons. Experiments on the β decay emissions of thorium (Meitner and Hahn in 1912 [3]) and radium (Chadwick in 1914 [4]) showed that the process had a continuous energy spectrum, not consistent with the predicted discrete spectrum of a two-body decay.

Neutrinos were introduced on December 4 in 1930, when Wolfgang Pauli, in order to explain the continuous energy spectrum in the radioactive β decay, proposed the existence of a new particle emitted with the electron. The particle proposed by Pauli was a very light weighted neutral particle with a spin $1/2$. The particle, initially called "neutron", was a "desperate remedy" to preserve the principle of conservation of energy and angular momentum in the β decay. In 1932 Chadwick discovered a neutral particle confined within the nucleus with mass similar to the proton, that was called neutron [5]. Pauli's "neutron" was predicted with a mass not larger than 0.01 proton mass, hence different from the Chadwick's one. In 1933 Fermi renamed Pauli's neutron to "neutrino".
The Fermi theory of beta decay, proposed in 1933, describes the beta decay of a neutron by the direct coupling of the neutron with a proton, an electron and a neutrino, Figure 1.1 [6]. Fermi's interaction was an effective theory able to provide predictions for experimental observables (decay rate, electron energy spectrum, mean life and others) of β decays and many other weak processes. The decay constant for the beta decay can be evaluated using the so called "Fermi's Golden Rule":

$$\lambda = \frac{2\pi}{\hbar} |\langle f|\widehat{V}_{int}|i\rangle|^2 \rho(E_f) \ , \tag{1.1}$$

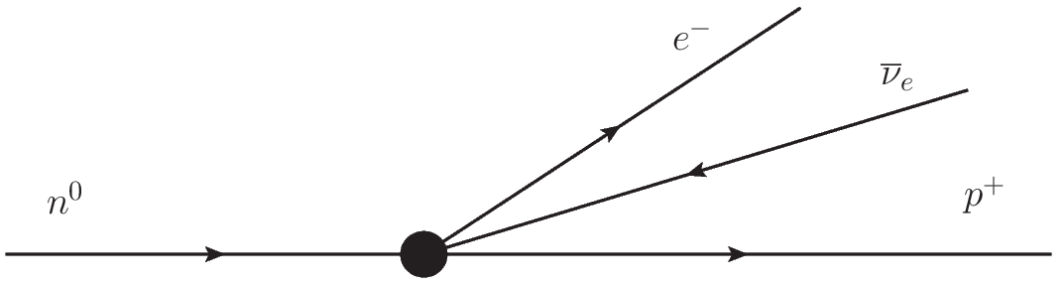

Figure 1.1: Fermi's 4-fermions beta-decay model.

where λ is the decay constant, $\widehat{V}_{int}$ is a perturbative approximation of the weak interaction evaluated between the initial and the final states and $\rho(E_f)$ is the density of the final allowed quantum states with energy E_f. If we introduce the neutrino hypothesis, the final states density will depend on the electron and anti-neutrino energy spectrum, thus Equation 1.1 can be rewritten emphasising the decay constant dependence on the electron momentum:

$$\frac{d\lambda}{dP_e} = \frac{2\pi}{\hbar} |\langle f|\widehat{V}_{int}|i\rangle|^2 \frac{dn_e dn_\nu}{dP_e dE} \propto \sqrt{(E-E_e)^2 - m_{\overline{\nu}}^2 c^4} \ , \tag{1.2}$$

where P_e is the electron momentum, n_e and n_ν are respectively electron and neutrino density and E is the energy available for the electron-antineutrino couple.
The Fermi interaction was the precursor to the theory of weak interaction, the V-A theory [7][8]. This new model introduced charged-current (CC) and neutral-current (NC) gauge mediators, the $W^\pm$ and the Z bosons. According the theory of weak interaction, the β^- decay can be described as the decay of a neutron into a proton and an electron and electron antineutrino couple by the emission of an intermediate W^- boson, Figure 1.2.

In 1946 Bruno Pontecorvo suggested that they could be detected via the interaction [9]:

$$\nu_e + {}^{37}Cl \rightarrow {}^{37}Ar + e^- \ ,$$

in which, exploiting the inverse β decay, a neutrino hitting a chlorine nucleus would turn it into an argon nucleous. In 1956, on June 14, electron anti-neutrinos were discovered by

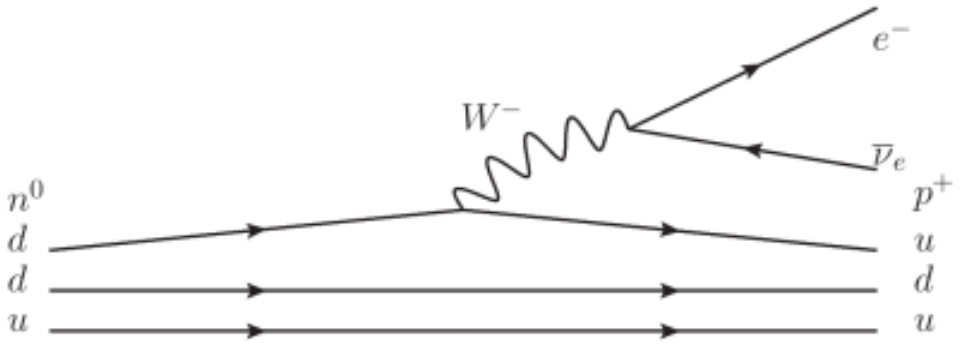

Figure 1.2: Leading order Feynman diagram for β^- decay.

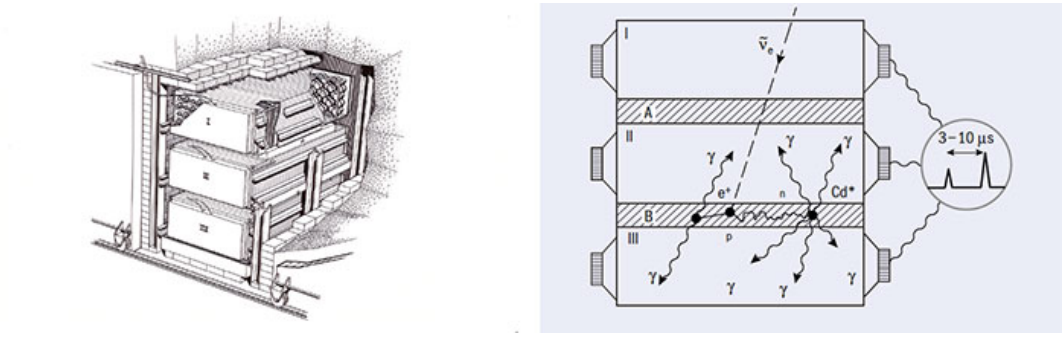

Figure 1.3: (Left) The Savannah River detector, it consisted in three tanks of scintillator each viewed by 100 phototubes. (Right) The principle of the delayed-coincidence method exploited to detect the electron antineutrino.

Reines and Cowan at the Savannah River nuclear reactor in the inverse β process [10]:

$$\bar{\nu}_e + p \rightarrow n + e^+ \ .$$

The detector consisted of a target of cadmium chloride dissolved in 1400 liters of water and surrounded by scintillators. The Savannah River nuclear reactor produced an intense anti-neutrino flux via β decay. The signal of an $\bar{\nu}$ was identified through the detection of the light emitted from the positron annihilation and the subsequent neutron capture emission few microseconds later, Figure 1.3.

The existence of a second type of neutrino, the muon neutrino, ν_μ, was discovered in 1962 by Schwartz, Lederman and Steinberger with an experiment at the Brookhaven AGS (Alternating Gradient Synchrotron at the Brookhaven National Laboratories) [11]. The new neutrino was produced in the pion decay:

$$\pi^- \rightarrow \mu^- + \bar{\nu}_\mu$$

and it was detected via charged-current (CC) interaction in a gas-filled spark chambers array.

A third type of neutrino, the tau neutrino, ν_τ, was detected in 2000 by the DONUT experiment at Fermilab [12], 25 years after the discovery of a third leptonic family (the τ family) at the SPEAR collider in Stanford [13].

1.2 Neutrinos in the Standard Model

The Standard Model (SM) is a successful gauge theory based on the symmetry group $SU(3)_C \oplus SU(2)_L \oplus U(1)_Y$. It describes the strong, weak and electromagnetic interactions via the exchange of the corresponding spin-1 gauge fields. The $SU(2)_L \oplus U(1)_Y$ group describes the electroweak sector, the L index represents the left chirality of the particles and Y represents their hypercharge, the corresponding bosons are photons, $W^\pm$ and Z. The $SU(3)_C$ group describes the strong interaction, the C index refers to the quark "color" charge, the corresponding bosons are the eight gluons.

The SM is divided in two distinct particle categories, bosons (integer spin) and fermions (half-integer spins). Bosons of the SM are reported Table 1.1. In the SM, fermions are classified in three different generations, each including two quarks and two leptons. The fermionic

	RelatedSymmetry	Particles
Electroweak bosons	$U(1)_Y$	γ
	$SU(2)_L$	$W^{\pm}$,Z
Strong Bosons	$SU(3)_C$	g

Table 1.1: Bosonic content of the SM.

	$SU(2)_L$ doublets	$SU(2)_L$ singlets
Quarks	$\begin{pmatrix} u_L \\ d_L \end{pmatrix}, \begin{pmatrix} c_L \\ s_L \end{pmatrix}, \begin{pmatrix} t_L \\ b_L \end{pmatrix}$	u_R,d_R,s_R,c_R,t_R,b_R
Leptons	$\begin{pmatrix} \nu_{eL} \\ e_L \end{pmatrix}, \begin{pmatrix} \nu_{\mu L} \\ \mu_L \end{pmatrix}, \begin{pmatrix} \nu_{\tau L} \\ \tau_L \end{pmatrix}$	e_R,μ_R,τ_R

Table 1.2: Fermionic content of the SM.

content of the SM is reported in Table 1.2, note that the right-handed neutrino ν_R is not included in the model.

Experimental evidences of the three fermionic families have been observed at e^+e^- LEP collider [14]. The analysis of the Z boson decay width in the neutrino channels confirmed the existence of only three families of neutrinos with $M_\nu \leq M_Z/2$, Figure 1.4.
The masses of the particles that compose the SM are provided by the BEH mechanism (from the names of the theorists, Brout, Englert and Higgs, that introduced it). In this model, a new scalar field associated with a spin-0 particle (the Higgs boson) couples with the SM bosons and fermions mass is obtained via spontaneous symmetry breaking of the couplings and it's proportional to the interaction between particles and anti-particles of opposite chirality. In June 2012, the ATLAS and CMS collaborations at LHC, announced the discovery of a particle with the expected characteristics for the Higgs boson [15].

So far, no evidences of right handed neutrinos of any flavour have been observed, hence, as they are currently described in the SM, neutrinos are massless.

1.3 Neutrino mass

In the SM neutrinos are two component Weyl fields and they do not couple with the Higgs field, hence they do not acquire mass terms.
From Eq. 1.2 it is possibile to obtain the so-called Kurie function:

$$K(E_e) = G\sqrt{(E - E_e)\sqrt{(E - E_e)^2 - m_\nu^2 c^4}} \ , \tag{1.3}$$

where G is a numerical constant. In the beta decay, if neutrinos are massless as predicted from the SM, Eq. 1.3 describes a straight line with a negative slope:

$$K(E_e) = G(E - E_e) \ . \tag{1.4}$$

Experimental measurements of the Kurie plot of different β-decays show that the endpoint of the slope is not linear, hence the neutrinos have mass and the current limit from observational cosmology is set to $m_\nu < 0.2$ eV. The future experiment KATRIN will study the Kurie plot of the tritium β-decay with a sensibility better than 0.2 eV [16][17].

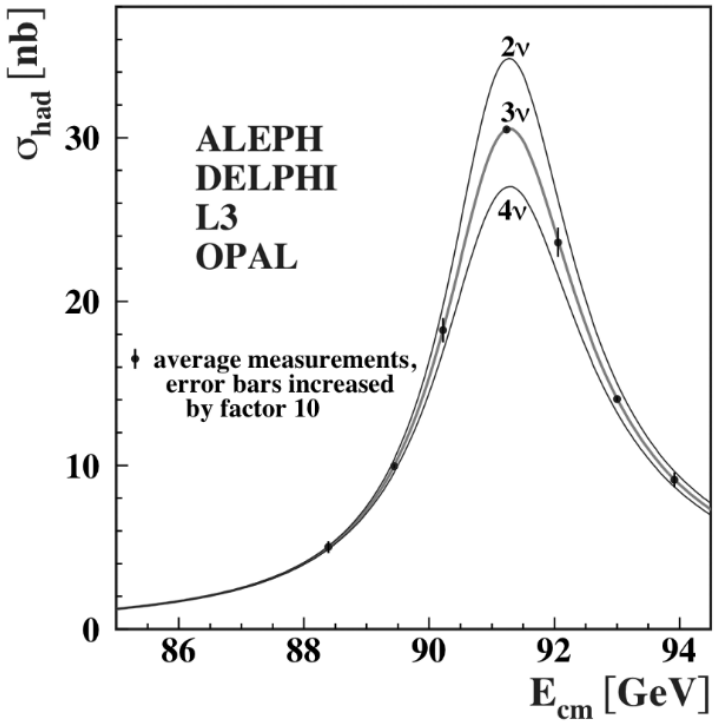

Figure 1.4: Measurement of the hadron production cross-section as a function of the LEP centre-of-mass energy around the Z-boson resonance. Curves represent the predictions for two, three and four neutrino families.

The first experimental evidence of the neutrino mass is the phenomenon of the neutrino oscillations, which will be discussed in the next section.
As previously stated, the SM does not account for massive neutrinos, hence a new paradigm has to be achieved. This new sector of physics is evidence of *BSM* physics (*Beyond the Standard Model*). The mechanism that assigns a mass term to neutrinos is still unknown and several hypothesis are considered.
If neutrinos are Dirac particles, $\nu \neq \bar{\nu}$, we can introduce a neutrino of right chirality ν_R and an anti-neutrino of left chirality $\bar{\nu}_L$. By doing so, we introduce a new coupling to the Higgs scalar field described by the Lagrangian mass term:

$$\mathcal{L}_D = -m_D(\bar{\psi}_L\psi_R + \bar{\psi}_R\psi_L) \ , \tag{1.5}$$

where the index D refers to a Dirac particle. For neutrinos:

$$\mathcal{L}_D = -m_D(\bar{\nu}_L\nu_R + \bar{n\nu}_R\nu_L) \ , \tag{1.6}$$

the quantum leptonic number is conserved. As previously said there is no so far experimental evidence of right handed neutrinos or left handed anti-neutrinos.

If neutrinos are Majorana particles, up to a phase there is no distinction with their antiparticles, $\nu = \bar{\nu}$. If this assumption is correct they can be described solely by one chirality component:

$$\psi = \psi_R + \psi_R^c = \psi^c \tag{1.7}$$

or

$$\psi = \psi_L + \psi_L^c = \psi^c \ , \tag{1.8}$$

where ψ^c is the corresponding antiparticle ($\psi^c = \mathcal{C}(\psi)$). For a Majorana particle, it is possible to write a mass term using the left chirality component only:

$$\mathcal{L}_{M,L} = -\frac{1}{2} m_M \bar{\psi}_L^c \psi_L \ . \tag{1.9}$$

Neutrinos are a good Majorana particle candidates and the corresponding mass term would be:

$$\mathcal{L}_{M,L} = -\frac{m_L}{2}(\bar{\nu}_L (\nu_L)^c + \bar{\nu}_L^c \nu_L) \ , \tag{1.10}$$

as a consequence of the Majorana hypothesis, the quantum leptonic number is violated.
Understanding whether neutrinos are Dirac or Majorana particles would provide a necessary

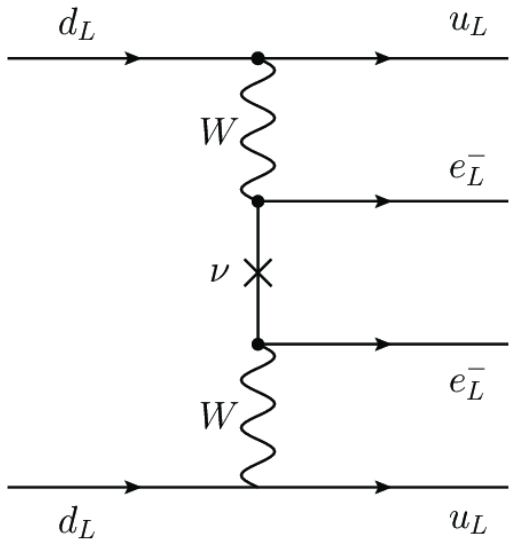

Figure 1.5: Diagram showing how any neutrinoless double beta decay process induces a ν-to-$\bar{\nu}$ transition, experimental signature of a Majorana particle.

tool in discovering the origin of their masses. The neutrinoless double beta decay reported in Figure 1.5 offers a unique experimental handle in solving this problem.
Another possible solution to the problem would be considering a unified approach by introducing a Majorana mass term of right chirality (m_R):

$$\mathcal{L}_{M,R} = -\frac{m_R}{2}(\bar{\nu}_R (\nu_R)^c + \bar{\nu}_R^c \nu_R) \ , \tag{1.11}$$

by doing so, both the right and left chirality components can participate in the Dirac mass term described previously. This unified Majorana-Dirac approach is called *see-saw* and its Lagrangian is:

$$\mathcal{L}_{D+M} = \mathcal{L}_{M,L} + \mathcal{L}_{M,R} + \mathcal{L}_D = -\frac{1}{2}\begin{pmatrix}\bar{\nu}_L & \bar{\nu}_R^C\end{pmatrix}\begin{pmatrix}m_L & m_D \\ m_D & m_R\end{pmatrix}\begin{pmatrix}\nu_L \\ \nu_R^C\end{pmatrix} + h.c. \ . \tag{1.12}$$

By diagonalizing the mass matrix, we obtain two Majorana neutrinos, one heavier than the other:

$$m_\pm = \frac{1}{2}\left[m_L + m_R \pm \sqrt{(m_L - m_R)^2 + m_D^2}\right] \ . \tag{1.13}$$

In the simplest version of this mechanism (called *seesaw type-I*), m_L is zero; the right-handed neutrinos do not take part in weak interactions and their masses can be very large ($m_R \gg m_D$). From these assumptions, it follows that from Eq. 1.13:

$$m_+ \simeq m_R \,, \ \ m_\nu = m_- \simeq \frac{m_D^2}{m_R} \ . \tag{1.14}$$

Type-I seesaw model can be in agreement with the Standard Model under the assumption that m_R is at the GUT scale ($\sim 10^{16}$ GeV). If this hypothesis is correct, there are three heavy sterile neutrinos with a mass order of m_R and three light neutrinos, whose mass is suppressed by a factor m_D/m_R with respect to m_D.

1.4 Neutrino oscillation puzzle

The Homestake Chlorine experiment was designed to study solar neutrinos produced in the nuclear reactions inside the Sun, according to the *Standard Solar Model*. In order to measure the solar neutrino flux, the experiment exploited the interaction

$$^{37}Cl + \nu_e \rightarrow {}^{37}Ar + e^- \ . \tag{1.15}$$

According to the first results published in 1965, the measured flux was only one third of the predicted value, this was later called the *solar neutrino problem*. In order the provide a solution to this issue, in 1967 B. Pontecorvo suggested the hypothesis of a $\nu \rightarrow \bar{\nu}$ oscillation, described as the mixing of two Majorana neutrinos [18].

1.4.1 Neutrino oscillations

The hypothesis of Pontecorvo was accepted and improved by Maki, Nakagawa and Sakata. In analogy to the quark mixing described by the CKM matrix, the neutrino mixing is described by the unitary *PMNS* matrix (Pontecorvo-Maki-Nakagawa-Sakata) [19]. According to this model, the oscillations between the three flavour eigenstates (ν_e, ν_μ and ν_τ) are the consequence of the linear combination between different mass eigenstates (ν_1, ν_2 and ν_3):

$$|\nu_\alpha\rangle = \sum_i U_{\alpha i}\,|\nu_i\rangle \qquad \alpha = e, \nu, \tau \qquad i = 1, 2, 3 \ , \tag{1.16}$$

where the matrix U is the PMNS matrix.
Considering oscillations in vacuum, the evolution at the time t of the flavour eigenstates ν_α is:

$$|\nu_i(t)\rangle = \sum_i U_{\alpha i}\,|\nu_i(t)\rangle \ \ , \tag{1.17}$$

where

$$|\nu_i(t)\rangle = e^{-iE_i t}\,|\nu_i(0)\rangle \quad . \tag{1.18}$$

The probability that a neutrino of flavour α oscillates to a different flavour at the time t is:

$$P(\nu_\alpha \to \nu_\beta) = |\,\langle \nu_\beta | \nu_\alpha(t)\rangle\,|^2 \ , \tag{1.19}$$

from which:

$$\left|\textstyle\sum_i U_{\beta i} e^{-E_i t} U^*_{\alpha i}\right| \tag{1.20}$$

$$= \sum_i \sum_j U^*_{\alpha i} U_{\beta i} U_{\alpha j} U^*_{\beta j} e^{-(E_i - E_j)t} \tag{1.21}$$

$$\equiv \sum_{i,j} J^{ij}_{\alpha\beta} e^{-i\Delta_{ij}} \ , \tag{1.22}$$

where we define $J^{ij}_{\alpha\beta} = U^*_{\alpha i} U_{\beta i} U_{\alpha j} U^*_{\beta j}$ and $\Delta_{ij} = (E_i - E_j)t \simeq \Delta m^2_{ij}/(2p)$, where $\Delta m^2_{ij} = m^2_i - m^2_j$ is the mass squared difference between the mass eigenstates ν_i and ν_j. In the approximation of ultra-relativistic neutrinos, $t \simeq L$ and $p \simeq E$, hence:

$$\Delta_{ij} \simeq \frac{\Delta m^2_{ij}}{2E} L \ , \tag{1.23}$$

where L is the distance traveled by the neutrinos and E is the neutrino energy. Under the assumption of the approximation in Eq. 1.23, the oscillations probability becomes:

$$\begin{aligned} P(\nu_\alpha \to \nu_\beta) &= \delta_{\alpha\beta} \\ -4 \sum_{i>j} \mathcal{R}(U^*_{\alpha i} U_{\beta i} U_{\alpha j} U^*_{\beta j} \sin^2[1.27 \Delta m^2_{ij}(L/E)]) \\ +2 \sum_{i>j} \mathcal{F}(U^*_{\alpha i} U_{\beta i} U_{\alpha j} U^*_{\beta j} \sin^2[2.54 \Delta m^2_{ij}(L/E)]) \ . \end{aligned}$$

If we consider a simplified scenario with only two flavours involved in the transition, the oscillation probability becomes:

$$P(\nu_\alpha \to \nu_\beta) = \sin^2 2\theta \sin^2\left[\tfrac{\Delta m^2 L}{4E}\right] \ , \tag{1.24}$$

or

$$P(\nu_\alpha \to \nu_\beta) = \sin^2 2\theta \sin^2\left[1.27 \tfrac{\Delta m^2[eV^2] L[km]}{E[GeV]}\right] \ . \tag{1.25}$$

From Eq. 1.24, the oscillation probability is defined by the amplitude of the oscillation $\sin^2 2\theta$, where θ is the corresponding mixing angle; the transition amplitude depends only on the ratio L/E. The maximum probability to find the neutrino in the ν_β state is at the distance $L/2 = 2\pi E/\Delta m^2$, after a full oscillation length the neutrino will be again at its initial state.

If we extend the mixing to three neutrino eigenstates, the PMNS matrix becomes:

$$\begin{aligned} U_{PMNS} = &\begin{pmatrix} 1 & 0 & 0 \\ 0 & c_{23} & s_{23} \\ 0 & -s_{23} & c_{23} \end{pmatrix} \times \begin{pmatrix} c_{13} & 0 & s_{13} e^{-i\delta} \\ 0 & 1 & 0 \\ -s_{13} e^{i\delta} & 0 & c_{13} \end{pmatrix} \\ &\times \begin{pmatrix} .c_{12} & s_{12} & 0 \\ -s_{12} & c_{12} & 0 \\ 0 & 0 & 1 \end{pmatrix} \times \begin{pmatrix} e^{i\alpha_1/2} & 0 & 0 \\ 0 & e^{i\alpha_2/2} & 0 \\ 0 & 0 & 1 \end{pmatrix} \ , \end{aligned} \tag{1.26}$$

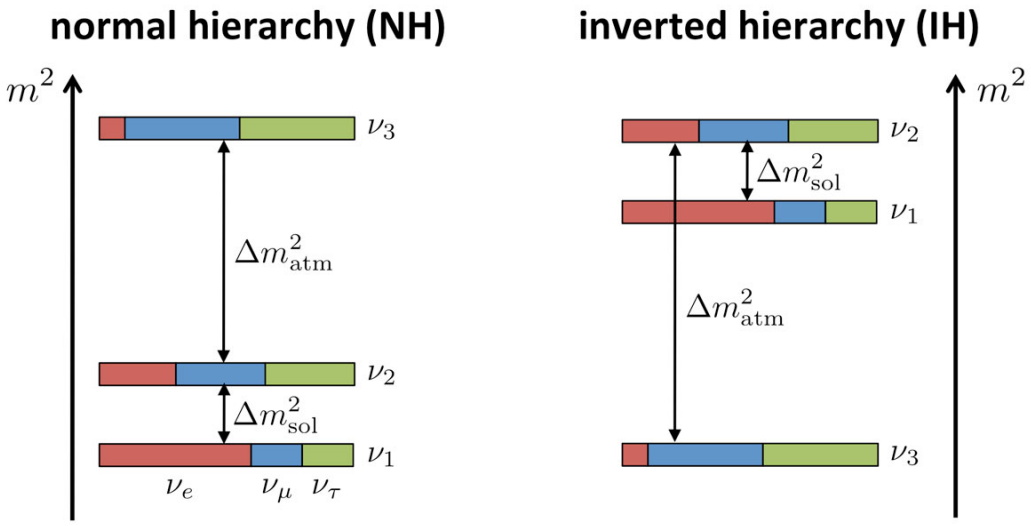

Figure 1.6: Two potential mass orderings of neutrinos: the normal ordering (normal hierarchy) and the inverted ordering (inverted hierarchy).

where c_{ij} and s_{ij} represent $\cos\theta_{ij}$ and $\sin\theta_{ij}$ respectively, $\delta = [0, 2\pi]$ is a Dirac CP violation phase and $\alpha(i = 1, 2)$ are the Majorana phases.
This parametrization in four matrices is suitable to the study of neutrino oscillations in different sectors, in particular: the first matrix contains the leading parameters for ν oscillations in the atmospheric sector, the second is associated with the reactor neutrino oscillations, the third with the solar neutrino experiments and the fourth contains the Majorana phases that can be studied with the neutrinoless double beta decay.

To summarize what has been described so far, the neutrino oscillation of three different flavour eigenstates is a phenomenon described by 3 angles (θ_{12},θ_{23} and θ_{13}, in U_{PMNS}), one CP phase (δ, in U_{PMNS}), two Majorana phases (α_1 and α_2, in U_{PMNS}) and two signed Δm^2 (Δm^2_{12} and Δm^2_{13}, from Eq. 1.24). As fas as the Δm^2, neutrino oscillations do not provide any information about the sign of the square mass difference. Two scenarios consistent with the experimental measurements are possibile: normal hierarchy and inverted hierarchy. In normal hierarchy neutrino mass eigenstates are ordered $m_1 < m_2 \ll m_3$, while in inverted hierarchy $m_3 \ll m_2 < m_1$, as shown in Figure 1.6.
The description of the oscillation of neutrinos that travel in matter is different from the probability calculated in vacuum. Although neutrinos interactions with matter have a very low cross section, coherent forward scattering from particles can modify the oscillation probability. The scattering can be induced by both a charged current (CC) and neutral current (NC) interaction, reported in Figure 1.7. CC and NC scattering introduce an additional term in the Hamiltonian, respectively:

$$V_{CC} = \sqrt{2} G_F N_e \quad V_{NC} = -\frac{1}{2}\sqrt{2} G_F N_n \ , \tag{1.27}$$

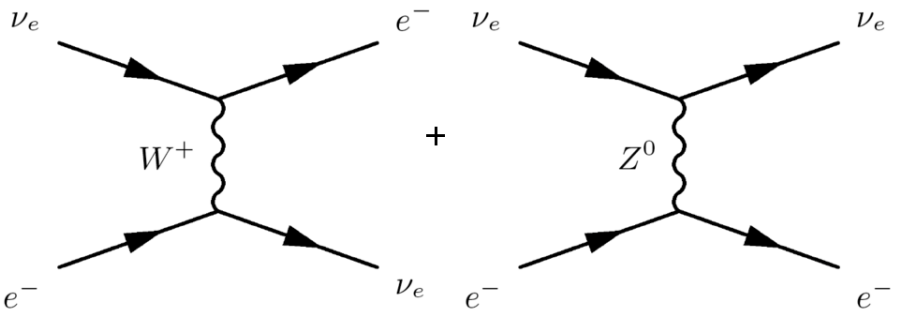

Figure 1.7: Feynman tree-level diagram for charged (left) and neutral current (right) components of $\nu_e + e^- \to \nu_e + e^-$ scattering, to be extended to the other flavours.

where G_F is the Fermi constant, N_e is the electron density and N_n is the neutron density. For ν_μ and ν_τ only NC scattering have to be considered since μ and τ are not present in ordinary matter. These coherent scattering effects are called *matter effects*.
Oscillation experiments are divided in different sectors based on the neutrino source they use, which can be artificial, like reactors or accelerators, or natural, like solar ($\odot$) or atmospheric (atm) neutrinos. Different sources allow to study different L/E ratios and access with different sensitivity the various parameters of the *PMNS* matrix.
Another distinction between oscillation experiments is based on the type of measurement performed:

- *Appearance* experiments measure the oscillation probability of a neutrino with flavour α at the source in a neutrino of different flavour ($P(\nu_\alpha \to \nu_\beta)$, with $\alpha \neq \beta$).
- *Disappearance* experiments measure the decrease in the flux of the neutrino flavour at the source, it is the survival probability of a given flavour ($P(\nu_\alpha \to \nu_\alpha) = 1 - \sum_{\beta \neq \alpha} P(\nu_\alpha \to \nu_\beta)$).

1.4.2 Solar sector

Neutrinos are abundantly produced in the core of the Sun and they originate from two different nuclear reactions: *pp* chain and *CNO* cycle.

For solar neutrinos, the ratio L/E allows mainly the mixing between ν_1 and ν_2, hence oscillations terms proportional to Δm^2_{31} are subdominant. With this approximation, Solar neutrinos experiments are the leading candidate to access with the best sensitivity the parameters $\sin^2\theta_{12}$ and Δm^2_{12}, for this reason the θ_{12} angle is also called *solar mixing angle* ($\theta_\odot$) and $\Delta m^2_{12} = \Delta m^2_\odot$.

The first Solar neutrinos experiments used chlorine (like Homestake [20]) or, more recently, gallium (like SAGE [21] and Gallex/GNO [22]) to measure the ν_e flux. Modern experiments are based on Cherenkov detectors and the two most famous exempla are Super-Kamiokande and Borexino. Super-Kamiokande is a 50 kton of pure water Cherenkov detector built in a mountain in Kamioka, Japan [23]. Borexino is a $\sim$ 300 ton of organic scintillator (pseudocumene) Cherenkov detector situated in Laboratori Nazionali del Gran Sasso (LNGS), Italy [24]. Another Cherenkov based experiment is SNO (Sudbury Neutrino Observatory), Canada, it used 1 kton of heavy water (D_2O) to produce Cherenkov light [25].
The SNO experiment measured the CC $\nu_e d \to p + p + e^-$ and the NC $\nu_x d \to p + n + \nu_x$ interactions. The first interaction is sensitive only tu ν_e, hence the electron neutrino flux $\Phi(\nu_e) = \Phi_{CC}$. The other interactions are sensitive to all the other neutrino flavours, hence the total neutrino flux $\Phi(\nu_e + \nu_\mu + \nu_\tau) = \Phi_{NC}$. The observed ratio $\Phi_{CC} = \Phi_{NC}$ was $\sim$1/3, in accordance with the Homestake results presented in section 1.4.
Super-Kamiokande and Borexino studied an energy range spanning from hundreds of keV to some MeV. The same region is accessible by reactor neutrinos experiments.

1.4.3 Atmospheric sector

The θ_{12} and Δm^2_{12} parameters are dominant in the Solar sector, while atmospheric neutrinos experiments can access with good sensitivity the parameters θ_{23} and Δm^2_{23}, hence $\theta_{23} = \theta_{atm}$ and $\Delta m^2_{23} = \Delta m^2_{atm}$.

Atmospheric neutrinos are produced as decay products in hadronic showers resulting from collisions of cosmic rays with nuclei in the atmosphere. Pions and kaons decay mainly in the $\pi^+ \to \mu^+\nu_\mu$ and $K^+ \to \mu^+\nu_\mu$ channels, while electron neutrinos are produced in the muon decay $\mu^+ \to \nu_e\bar{\nu}_\mu$. The ratio between the muon to electron neutrinos is known with a precision of 5%:

$$R = \frac{N_{\nu_\mu} + N_{\bar{\nu}_\mu}}{N_{\nu_e} + N_{\bar{\nu}_e}} \simeq 2 \ . \tag{1.28}$$

Oscillations from atmospheric neutrinos can be identified as differences between R and the measured value.
The most important experiments that studied oscillations from atmospheric neutrinos were Soudan-2, MACRO and Super-KamiokaNDE.
Soudan-2 was an iron tracking calorimeter placed in the Soudan Mine in North Minnesota. The experiment measured the ratio R and it was smaller then the predicted value, it was consistent with the hypothesis of an oscillation of $\nu_\mu \to \nu_\tau$ with maximal mixing at $\Delta m^2_{23} = 5.2 \times 10^{-3}$ eV^2 [26].
The MACRO experiment was situated at LNGS and it consisted in three sub-detectors: liquid scintillation counters, limited streamer tubes and nuclear track detectors. According to Soudan-2, MACRO measured a lower then expected ratio R and confirmed the hypothesis of $\nu_\mu \to \nu_\tau$ oscillation. It measured a maximal mixing at $\Delta m^2_{23} = 2.3 \times 10^{-3}$ eV^2 and ruled out the hypothesis of non oscillations with 5σ [27].

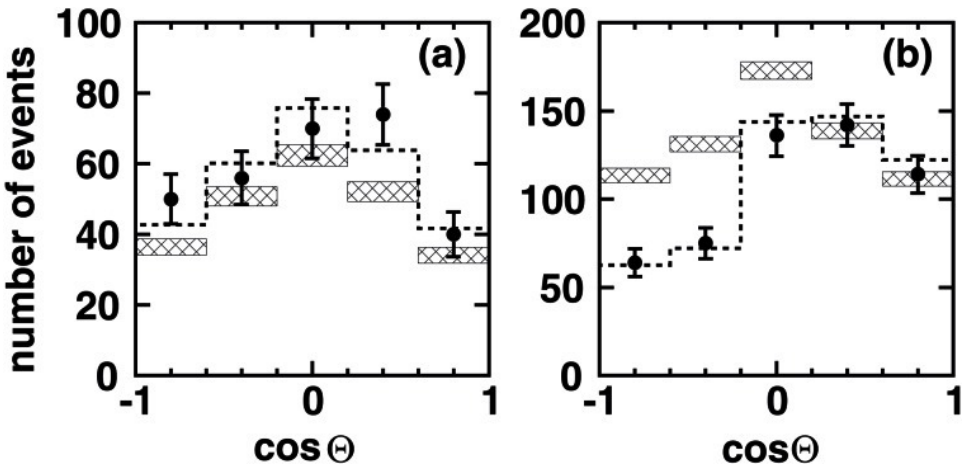

Figure 1.8: Zenith angle distributions for multi-GeV atmospheric neutrino events based on 535 days exposure of the Super-Kamiokande detector. Coloured areas are the predicted MC events and dots are the experimental measurements. The left and right panels show the distributions for e-like and μ-like events. Θ shows the zenith angle, and $\cos\Theta = 1$ and -1 represent events whose direction is vertically downward-going and upward-going, respectively.

Super-KamiokaNDE was a Cherenkov detector suitable for detection of neutrinos of different sources. This experiment observed a zenith angle dependence that supported the $\nu_\mu \rightarrow \nu_\tau$ oscilation hypothesis at 6.2σ Super-KamiokaNDE measurement are shown in Figure 1.8 [28].

1.4.4 Nuclear reactor neutrinos

Nuclear reactors emits $\bar{\nu}_e$ via fission reactions, with an energy of the order of few MeV. Their low energy does not allow to produce charged leptons heavier than the electron in CC interactions, hence the reactor anti-neutrino oscillation can be studied in the disappearance channel only.
The $\bar{\nu}_e$ energy spectrum is derived from the β-decay spectrum of the fissile elements in the reactor core. Through comparison between the observed rate of positrons from the inverse β-decay measurements and the predicted rate, reactor neutrino experiments can measure the oscillation parameters.

Reactor neutrinos experiments can access the θ_{13} parameters and several experiments like Daya Bay (China), RENO (South Korea) and Double Chooz (France) did it [29] [30][31]. The combined analysis is shown in Figure 1.9 and the best fit of the combined experiments is $\theta_{13} = 8.60 \pm 0.13°$.
Another important reactor neutrino experiment is KamLAND (Kamioka Liquid scintillator Anti-Neutrino Detector), positioned in the KamiokaNDE cavity. The site is surrounded by 53 Japanese commercial nuclear reactors at an average distance of 180 km. This experiment was able to investigate an L/E value typical of Solar neutrinos, hence it accessed and measured with high sensitivity the θ_{12} and Δm^2_{12} parameters. The result of the combined analysis of KamLAND and the Solar neutrino experiments are shown in Figure 1.10 [32].

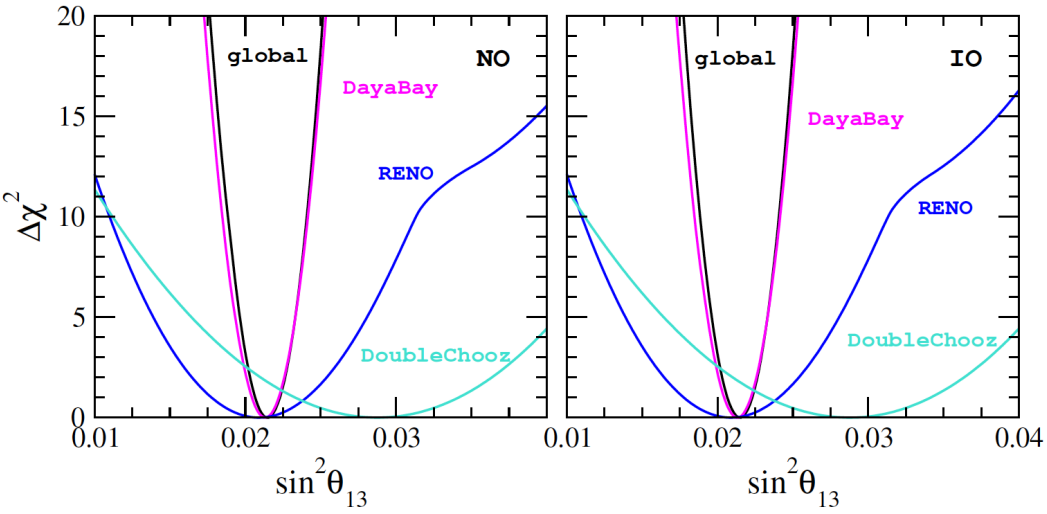

Figure 1.9: Profile of $\Delta\chi^2$ as a function of $\sin\theta_{13}{}^2$ from the analysis of global data (black line) and the various reactor experiments in normal mass ordering (left) and inverted mass ordering (right).

1.4.5 Accelerator experiments

Precise measurements on neutrino oscillations can be made using neutrino beams. High energy neutrino beams are produced by accelerating protons up to tens or hundreds of GeV and by directing them on a target, secondary particles of the desired momentum are then selected via lensing devices and then focused in a parallel beam towards the decay pipe. One of the great advantages of using accelerator neutrinos lies in the fact that the entire experiment can be designed and controlled by physicist, hence, since different parameters of the neutrino oscillations are accessed by different values of the L/E ratio, by tuning the energy and placing detectors at different oscillation length most of the parameters can be accessed.

Long baseline experiments

Long baseline accelerator experiments are characterised by a long length L and are designed to perform precision measurements of the oscillation parameters, with a characteristic ratio of:

$$\frac{L}{E} \lesssim 10^3 \; km/GeV \implies \Delta m^2 \gtrsim 10^{-3} \; eV^2 \; . \tag{1.29}$$

Long baseline experiments can operate both in the appearance and in the disappearance channels. These experiments consist of two detectors: a *near* detector to analyse the neutrino energy spectrum before the oscillation and a *far* detector to analyse the energy spectrum of oscillated neutrinos.
The first long baseline disappearance experiments were K2K and MINOS.

K2K (KEK to Kamioka) was an experiment which directed a muon neutrino beam of $\langle E_\nu \rangle \sim 1$ GeV from the accelerator facilities (KEK) to the Kamioka observatory. The near detector was situated ∼300 meters from KEK and Super-KamiokaNDE was used as the far

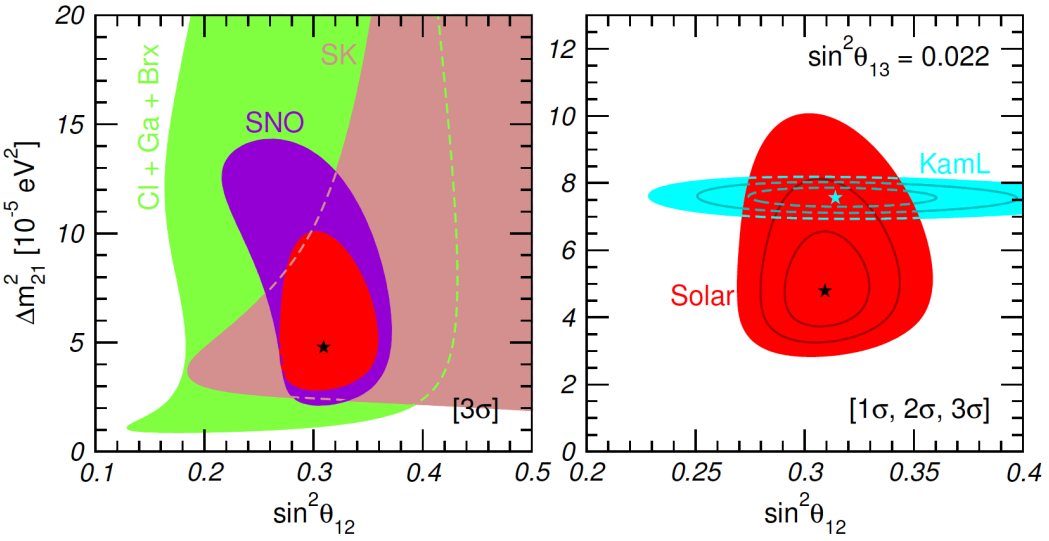

Figure 1.10: Allowed regions of θ_{12} and Δm^2_{12} from the global fit of the solar neutrino data (red) as well as KamLAND (blue), for θ_{13} fixed to the best fit of the reactor experiments. In the left panel regions restricted by individual experiments are shown.

detector, at the distance of 250 km. K2K confirmed the atmospheric oscillations [33].
MINOS operated on the NuMI beam from FNAL (Fermilab National Accelerator Laboratories) in Chicago towards the Soudan Mine facilities, at a distance of 735 km. The beam consisted in $\langle E_\nu \rangle \sim 2$ GeV muon neutrinos and precision measurements were obtained using equivalent near and far detectors. MINOS, again, confirmed the atmospheric oscillations and explored the parameter region with great sensitivity [34].
Important long baseline appearance experiments were OPERA and ICARUS-T600 at LNGS and both operated on the CNGS muon neutrino beam from the Cern SPS to LNGS, a long baseline of 732 km with $\langle E_\nu \rangle \sim 17$ GeV.
The OPERA experiment was designed to search for ν_τ appearance using nuclear emulsion with micro-metric resolution. The experiment recorded events corresponding to 1.8×10^{19} pot (protons on target) and reported the observation of 5 ν_τ candidates [35]. With a background of 0.25 events, OPERA could establish the appearance of ν_τ in the CNGS beam with a significance exceeding 5 σ.
The ICARUS experiment, described in section 2.6, operated in the same appearance channel as OPERA.
The current experiments T2K (K2K successor) and NOvA (MINOS successor) are dedicated to a precision measurement of the $\nu_\mu \to \nu_\mu$ disappearance and $\nu_\mu \to \nu_e$ appearance channels [36][37]. In Figure 1.11 are reported the results of these experiments and they are compared with those obtained from atmospheric experiments.

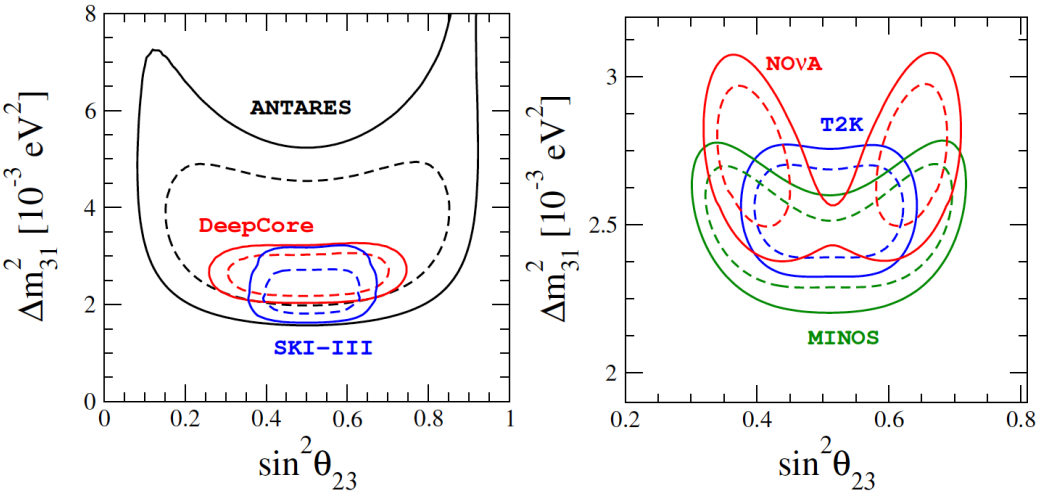

Figure 1.11: 90% (straight line) and 99% (dashed line) C.L. allowed regions in the $\sin^2\theta_{23} - \Delta m^2_{31}$ plane obtained from atmospheric (left) and long baseline accelerator (right) experiments, in the normal mass hierarchy assumption.

Short baseline experiments

Short baseline accelerator experiments are characterised by the study of neutrinos at short oscillation lengths, with a characteristic ratio of:

$$\frac{L}{E} \lesssim 1\ km/GeV \implies \Delta m^2 \gtrsim 1\ eV^2\ . \tag{1.30}$$

Short baseline experiments can operate both in disappearance and appearance channel and no one had a near and far detector structure. The first short baseline accelerator experiments were NOMAD and CHORUS at CERN on the WANF muon neutrino beamline [38][39]. These two experiments studied the $\nu_\mu \to \nu_\tau$ oscillations. No oscillations were observed by either of the experiments; the exclusion plots are reported in Figure 1.12.

1.4.6 Neutrino anomalies

In recent years, several experimental anomalies have been reported which, if experimentally confirmed, could be hinting additional physics beyond the Standard Model. Anomalies are divided in two distinct classes: apparent disappearance signal in low energy $\bar{\nu}_e$ and evidence for an electron-like excess in interactions coming from muon neutrinos and $\bar{\nu}$ from particle accelerators.
The short baseline neutrino oscillation anomalies can be explained by introducing an additional squared-mass difference (Δm^2_{SBL}) much larger than the solar and the atmospheric squared-mass differences. The additional mass difference term Δm^2_{SBL} would be $\sim$1 eV^2.

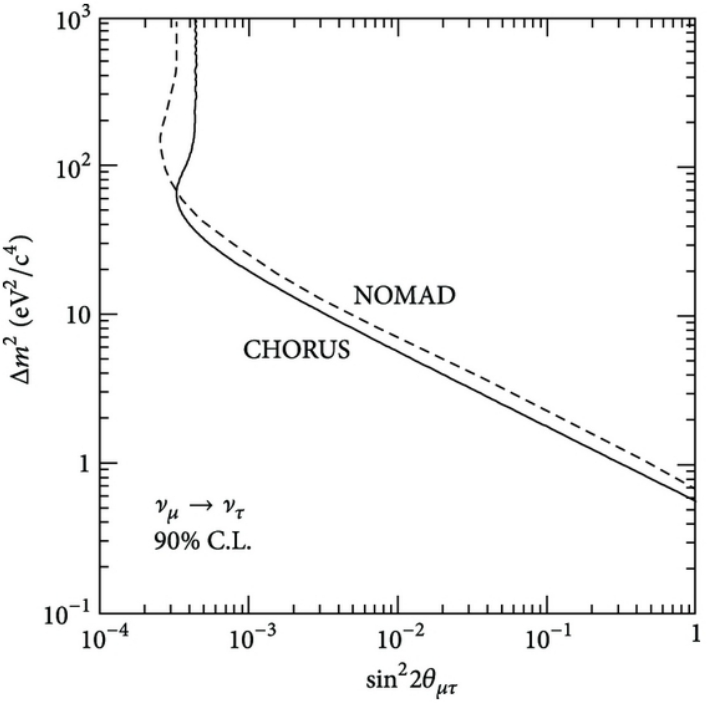

Figure 1.12: Exclusion plot showing the combined final result of the NOMAD and CHORUS experiments in the $\nu_\mu \rightarrow \nu_\tau$ oscillation channel.

Reactor neutrino anomalies

The *reactor anomaly* refers to the deficit of $\bar{\nu}_e$ observed in numerous detectors few meters away from the nuclear reactors, compared to the predicted rates, with $R_{avg} = N_{obs}/N_{pred} = 0.927 \pm 0.023$ [40]. Recent updates have changed the predictions slightly giving a ratio $R_{avg} = N_{obs}/N_{pred} = 0.938 \pm 0.023$, a 2.7σ deviations from unity.

Gallium anomaly

The *Gallium anomaly* refers to electron neutrino disappearance recorded by the SAGE and GALLEX solar neutrino experiments measuring the calibration signal from a Mega-Curie radioactive source. The combined ratio between the detected and predicted neutrino rates from sources is $R = 0.86 \pm 0.05$, again 2.7σ deviations from unity [41].

LSND anomaly

The *LSND anomaly* refers to an electron-like excess in neutrino interactions observed by the LSND experiment. LSND (*Liquid Scintillator Neutrino Detector*) was a short baseline accelerator experiment at the Los Alamos National Laboratories. The experiment consisted in a baseline of 30 m and in a decay-at-rest pion beam to produce muon anti-neutrino with

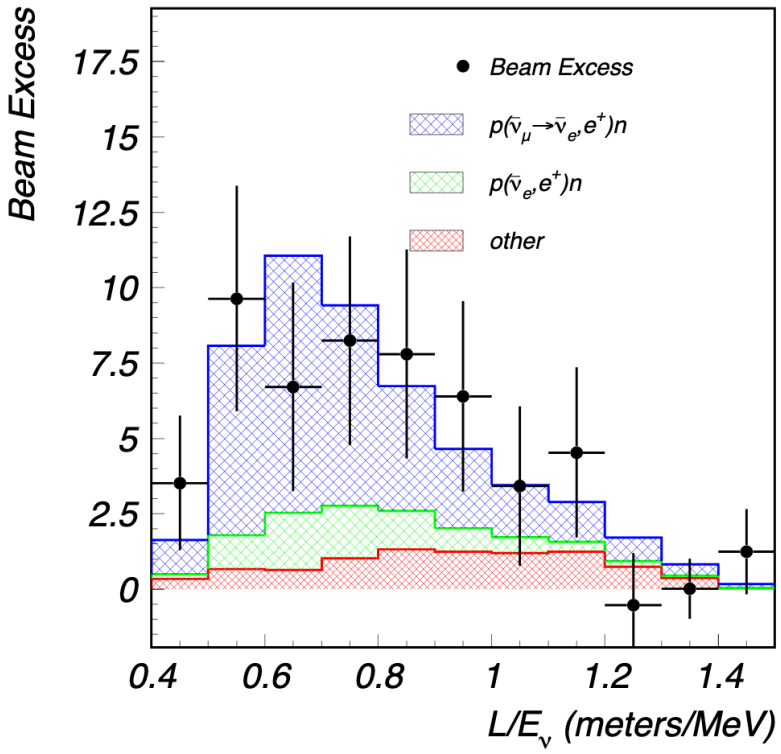

Figure 1.13: Excess of electron neutrino candidate events observed by the LSND experiment.

energies in the range of 20-200 MeV, making it sensitive to mass squared differences of the order of 1 eV^2. After 5 years of data taking, $89.7 \pm 22.4 \pm 6.0$ $\bar{\nu}_e$ candidates were observed above backgrounds, corresponding to 3.8σ evidence for $\bar{\nu}_\mu \to \bar{\nu}_e$ oscillations. This excess, shown in Figure 1.13, cannot be accommodated with the three Standard Model neutrinos, the resulting mass squared difference of $\Delta m^2 \simeq 1$ eV^2 would be incompatible with the ones resulting from other neutrino oscillation experiments, since, in the actual oscillation framework, there can be only two independent mass squared differences in the case of three neutrino flavours [42][43].

MiniBooNE

The MiniBooNE experiment at Fermilab was a short baseline experiment consisting in an 800 ton Cherenkov detector placed at 540 metes from the Boosted Neutrino Beam (BNB) facility. MiniBooNE was design to inspect the same LSND L/E ratio, in order to confirm its observations by studying both the $\bar{\nu}_\mu \to \bar{\nu}_e$ and the $\nu_\mu \to \nu_e$ transitions. From 2002 to 2017, MiniBooNE collected a total of 11.27×10^{20} pot in antineutrino mode and 12.84×10^{20} in neutrino mode, the combined analysis of these two dataset observed a ν_e excess in both the running modes of 460.5 ± 99.0 events, corresponding to 4.7σ. The Mini-BooNE allowed

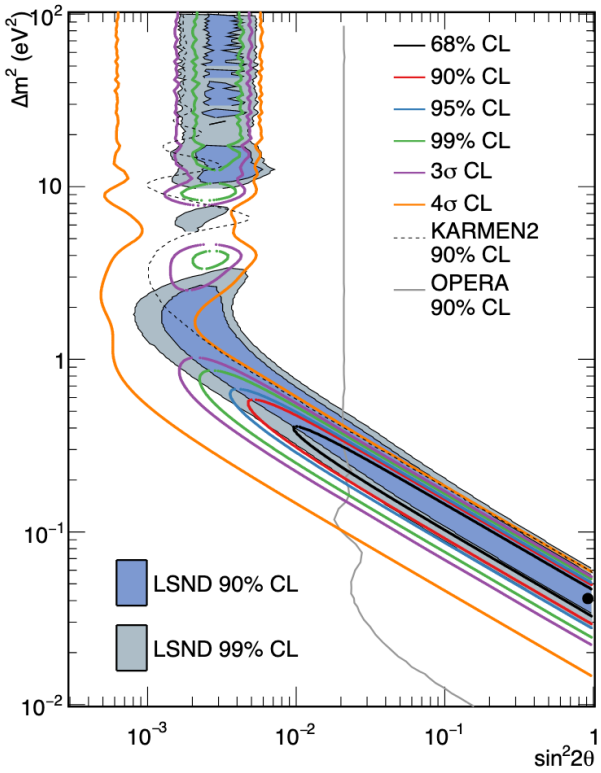

Figure 1.14: MiniBooNE allowed regions for a combine neutrino and antineutrino mode within a two-neutrino oscillation model. The shaded areas show the 90% and 99% confidence level LSND $\bar{\nu}_\mu \to \bar{\nu}_e$ allowed regions.

region from a two-neutrino oscillation fit to the data, shown in Figure 1.14, is consistent with the allowed region reported by the LSND experiment, the significance of the combined LSND and MiniBooNE excesses is 6.0σ. A two-neutrino oscillation interpretation of the data would require at least four neutrino types [44].

Appearance and disappearance

The results of global fit of appearance and disappearance data are presented in Figure 1.15 [45]. The oscillation parameters sensitive to the oscillation anomalies are $\sin^2 2\theta_{e\mu}$ and, eventually, Δm^2_{41}.

A strong tension between the appearance and the ν_e and ν_μ disappearance data can be observed in the global fit. The current status of the global fit of appearance and disappearance data indicates that the interpretation of the results of some experiment or group of experiments in terms of neutrino oscillations is not correct. Future experiments will explore with high sensitivity the short baseline parameter region and will provide a definitive solution to the oscillation anomalies.

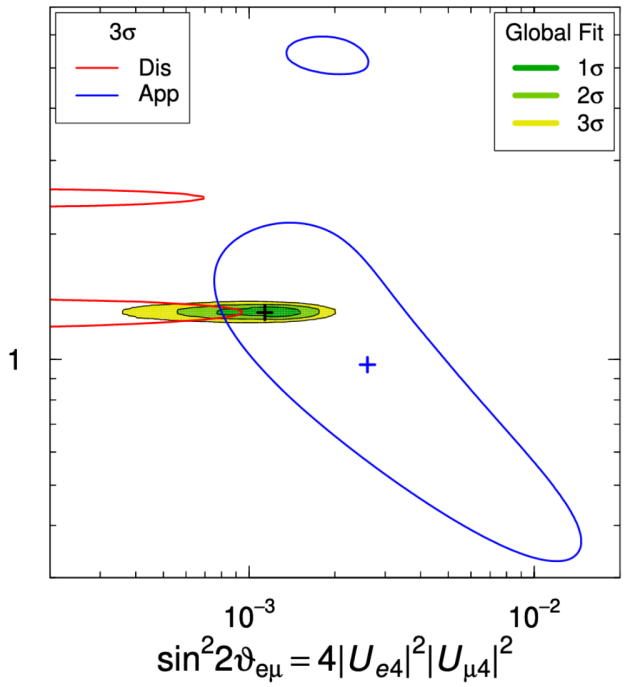

Figure 1.15: Global fit of appearance (App) and disappearance (Dis) data. The Dis lines exclude the region on their right at 3σ, while the App lines enclose the 3σ allowed regions. The shaded regions are allowed by the global combined fit.

1.5 Light sterile neutrinos

The hypothesis of a light sterile neutrino was introduced in order to explain the anomalies described in the previous section. Sterile neutrinos are neutral leptons that do not interact weakly with the W and Z bosons (to avoid clashing with the number of active neutrinos measured by LEP in Figure 1.4), but participate in the neutrino mixing. Heavy sterile neutrinos predicted from the type-I seesaw model are not able to describe the measured excess, which could be easily described by the existence of a light sterile neutrino.
The minimal scheme that can describe short baseline anomalies, includes one light sterile neutrino and its called "*3+1 model*". In order to explain the data of the current *neutrino-Standard Model* (νSM) three of the mass states must have very little mixture of sterile neutrino (as illustrated in Figure 1.16).
In the 3+1 framework, a new generalisation of the PMNS matrix has to be made in order to include the light sterile neutrino in the mixing:

$$\begin{pmatrix} \nu_e \\ \nu_\mu \\ \nu_\tau \\ \nu_s \end{pmatrix} = \begin{pmatrix} U_{e1} & U_{e2} & U_{e3} & U_{e4} \\ U_{\mu 1} & U_{\mu 2} & U_{\mu 3} & U_{\mu 4} \\ U_{\tau 1} & U_{\tau 2} & U_{\tau 3} & U_{\tau 4} \\ U_{s1} & U_{s2} & U_{s3} & U_{s4} \end{pmatrix} \begin{pmatrix} \nu_1 \\ \nu_2 \\ \nu_3 \\ \nu_4 \end{pmatrix} \quad . \tag{1.31}$$

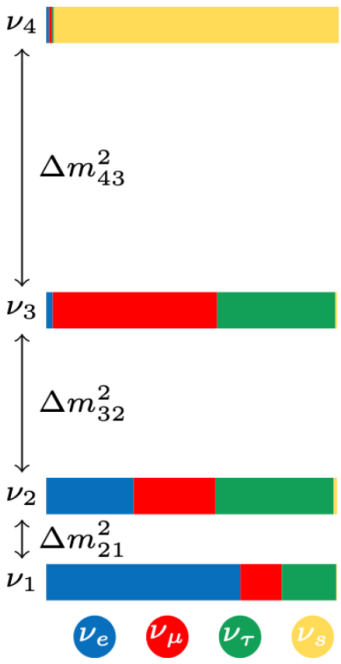

Figure 1.16: Illustration of normal neutrino mass ordering and mixing for the four neutrino picture.

We can parametrise this new matrix in terms of six mixing angles and three CP violating phases. In this new model, six new parameters are added: the angles θ_{14}, θ_{24} and θ_{14} (corresponding to the $\nu_s \to \nu_e$, $\nu_s \to \nu_\mu$ and $\nu_s \to \nu_\tau$ mixings), a new mass squared difference $\Delta m^2_{41} = m^2_4 - m^2_1$ and two CP violating phases δ_{14} and δ_{24}.

In order to describe the current neutrino oscillation in a 3+1 model, several criteria have to be fulfilled. The newly introduced non standard massive neutrino ν_4 has to be mostly sterile with an highly suppressed mixing with the ordinary neutrinos, otherwise solar, atmospheric and long baseline oscillations experiments would have observed the oscillation anomalies. The required constraints on the mixing parameters are

$$|U_{\alpha 4}|^2 \ll 1 \ \ (\alpha = e, \mu, \tau) \tag{1.32}$$

and

$$|U_{s4}|^2 \sim 1 \ , \tag{1.33}$$

while as far as the squared mass differences $|\Delta m_{21}|^2 \ll |\Delta m_{31}|^2 \ll |\Delta m_{41}|^2$.
In short-baseline experiments the effect of the small $|\Delta m_{21}|^2$ and $|\Delta m_{31}|^2$ are negligible because they generate oscillations at larger distances, therefore in these experiments the oscillation probability can be approximated as:

$$P^{SBL}_{\nu_\alpha \to \nu_\beta} \cong |\delta_{\alpha\beta} - \sin^2 2\theta_\alpha\beta \sin^2(\frac{\Delta m^2_{41} L}{4E})| \ . \tag{1.34}$$

1.5.1 Search for sterile neutrinos

Worldwide experimental efforts toward the search for light sterile neutrinos have been constantly growing since 2011. Preliminary results excluding part of the allowed range of parameters and debated hints for new oscillation signals have already been published. Several new short-baseline experiments are expected to start in the upcoming years. The SBN program, which will be described in the next chapter, is going to be one of the leading experiments in this research field. Example of other experiments that will provide a detailed search for sterile neutrinos are NEOS, Neutrino-4, STEREO and SoLid.
NEOS is a $\sim$ 0.8 ton gadolinium based liquid scintillator experiment located 23.7 m from a 2.8 GW reactor unit in the Hanbit Nuclear Power Complex in Yeong-gwang, Korea [46]. The NEOS detector has an energy resolution of 5% at 1 MeV which allows a suitable spectral analysis. NEOS took data from August 2015 to May 2016 and reported important limits on the sterile neutrino parameters. The NEOS detector resumed data taking since September 2018.
Neutrino-4 is again a 1.8 m^3 gadolinium based liquid scintillator consisting of 50 liquid scintillator sections, it is installed near the 100 MW research reactor in Dimitrovgrad, Russia [47]. The detector is installed on a movable platform and the baseline ranges from 6 to 12 meters. The obtained L/E dependence of the inverse β-decay rate, normalized to the rate averaged over all distances, fits with an oscillation signal with the following parameters: $\sin^2\theta_{ee} = 0.35$ and $\Delta m^2_{41} = 7.22$ eV^2. The 3σ significance of the fit is in tension with the limits obtained by other reactor measurements.
STEREO is a gadolinium based liquid scintillator experiment located 11 m from the reactor core of the 58 MW High Flux Reactor of the Laue-Langevin Institute in France [48]. The detector consists of six optically separated cells readout by four PMTs and separated by passive and active shielding. STEREO is a running experiment that already released the first results based on a 66 days the reactor activity. Based on this data-set, STEREO excluded a significant portion of the sterile neutrino parameter space.
SoLid is an experiment in preparation using 12800 cells made of PVT cubes of 5×5×5 cm^3 in dimensions, partially coated with thin sheets of $^6LiF : ZnS(Ag)$ to capture and detect neutrons [49]. The detector is installed 6 m away from the 60 MW SCK-CEN BR2 research reactor in Belgium. The detector energy resolution is $\sigma_E/E \sim 14\%$ at $E = 1$ MeV. The detector is now in operational and taking data.

Chapter 2

The Short Baseline Neutrino experiment

The *Short-Baseline Neutrino* program (SBN) at Fermilab consists of three LArTPCs (Liquid Argon Time Projection Chambers) detectors located along the *Booster Neutrino Beam* (BNB). An illustration of the detectors location is shown in Figure 2.1. This experiment will be able to perform the most sensitive search for sterile neutrinos at the eV mass-scale through the analysis of both the appearance and disappearance oscillation channels. The experiment was approved in 2015 and it is expected to begin its first data acquisition run in 2020 [50][51].

2.1 The SBN Physics program

SBN is designed to address the possible existence of 1 eV mass-scale sterile neutrinos, which, if they exist, can introduce additional neutrino oscillations accessible with a short baseline oscillation experiment. The search for sterile neutrinos at Fermilab is motivated by the anomalous results obtained in previous short baseline experiments, namely the *LSND and MiniBooNE anomalies*, presented in section 1.4.6.
SBN will be the first short-baseline neutrino experiment that will take advantage of a near and far detector structure with similar technologies: multiple LArTPC detectors at different baselines along the BNB will allow to search for high-Δm^2 neutrino oscillation in the $\nu_\mu \to \nu_e$ (*Appearance*) and $\nu_\mu \to \nu_\mu$ (*Disappearance*) channels.
In the assumption of a *3+1 model*, the $\nu_\mu \to \nu_e$ appearance channel will be able the span the Δm^2_{41} parameter range within 0.3 eV^2 and 1.5 eV^2, with a mixing angle in the range of $0.002 \lesssim \sin^2\theta_{\mu e} \lesssim 0.0015$. In Figure 2.2 the oscillation probability at the different parameter range of SBN is presented.

The SBN program is expected to acquire data for three years in order to have sufficient statistics to cover, at $\geq 5\sigma$, the full 99% allowed region of the original LSND result, as shown in Figure 2.3. The experiment is divided in two different phases. The initial stage is characterised by the data acquisition of one LArTPC only called MicroBooNE. This detector is situated 470 m from the BNB target facilities, it consists in a 170 ton total mass (89 ton active mass) liquid argon TPC. MicroBooNE begin its data acquisition in October 2015 and

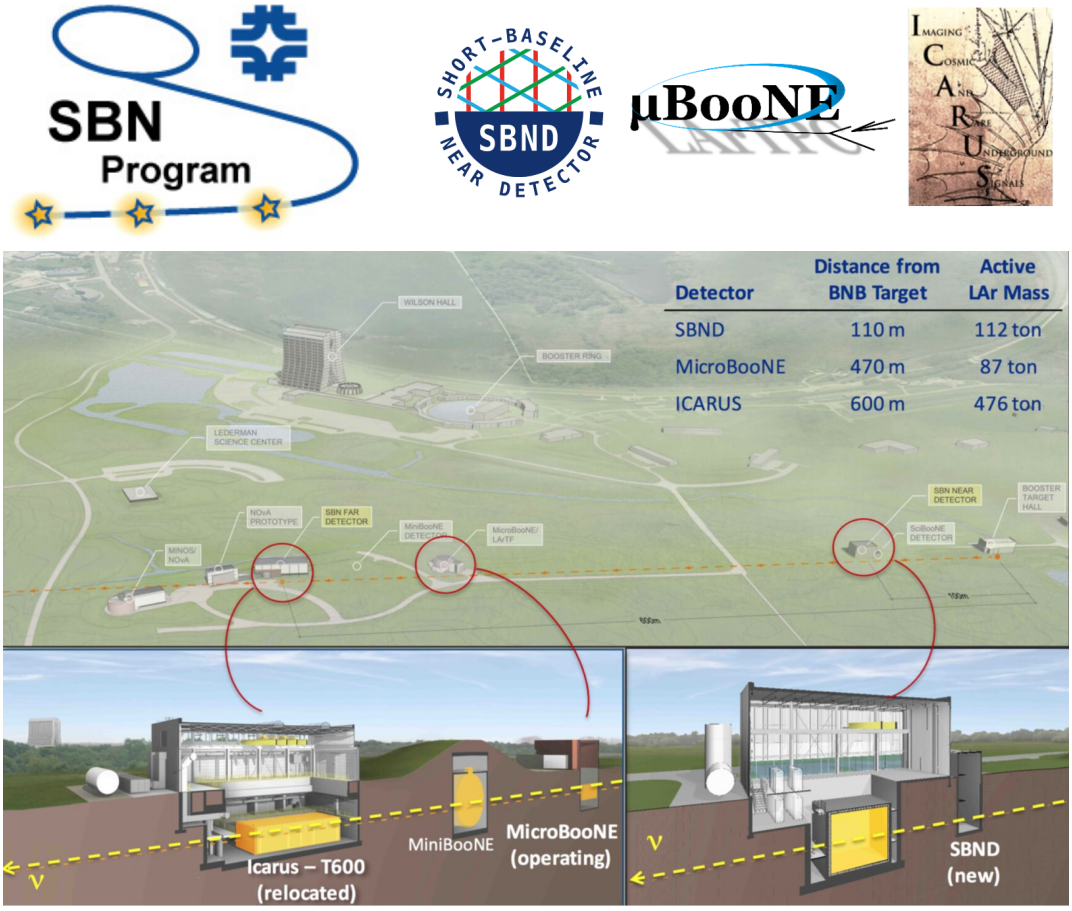

Figure 2.1: (*Top*) Logos of the different detectors that compose the SBN experiment. (*Bottom*) aerial illustration of the SBN experimental area at Fermilab, along the ν beam three detectors are placed: SBND, MicroBooNE and ICARUS-T600.

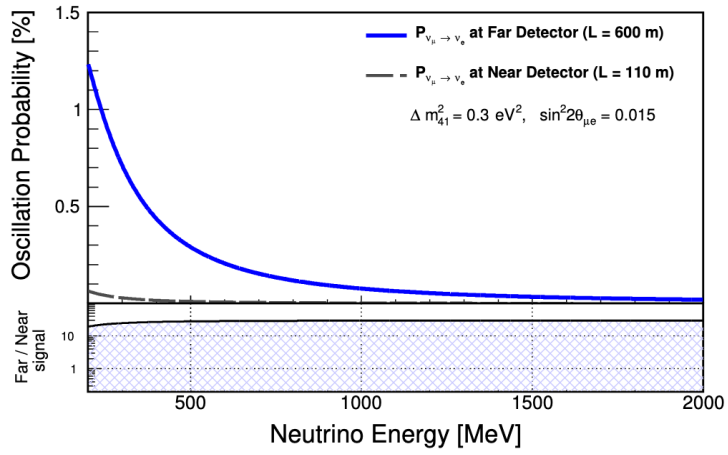

(a)

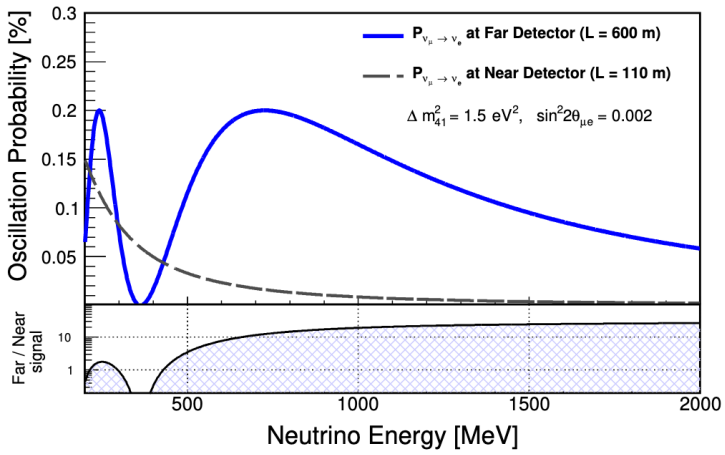

(b)

Figure 2.2: $\nu_\mu \to \nu_e$ oscillation probabilities at 110 m and 600 m for two different benchmark points in a *3+1* sterile neutrino model, (*a*) $\Delta m^2_{41} = 0.3$ eV^2 and (*b*) $\Delta m^2_{41} = 1.5$ eV^2.

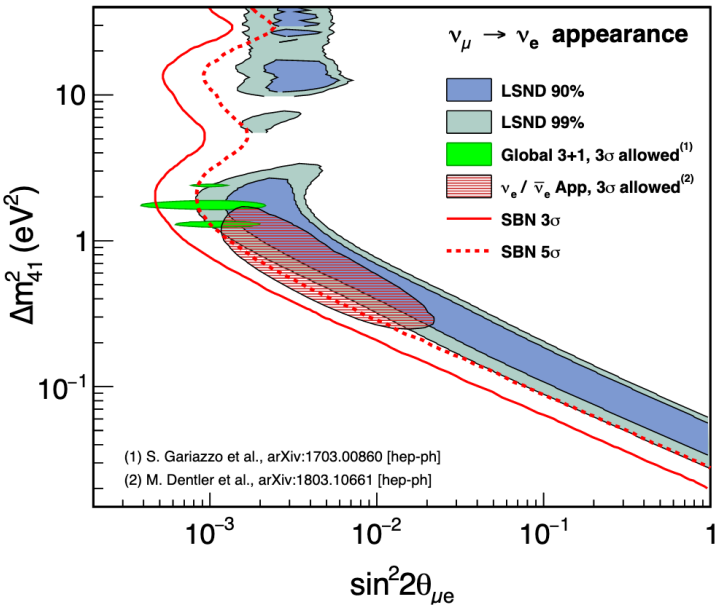

(a)

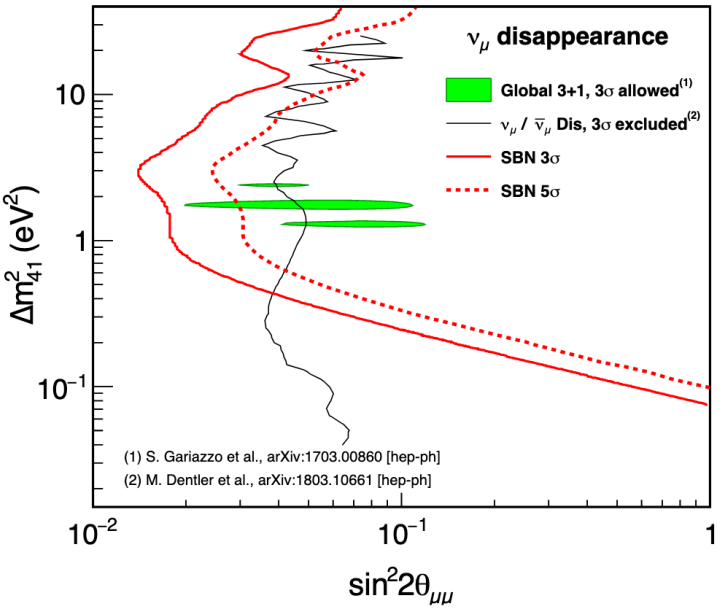

(b)

Figure 2.3: SBN sensitivities to a light sterile neutrino in the $\nu_\mu \rightarrow \nu_e$ appearance channel (a) and $\nu_\mu \rightarrow \nu_\mu$ disappearance channel (b).

Detector	Distance from BNB target	LAr total mass	LAr active mass
SBND	110 m	220 ton	112 ton
MicroBooNE	470 m	170 ton	89 ton
ICARUS	600 m	760 ton	476 ton

Table 2.1: Summary of the SBN detector locations and masses.

it is designed to search for the excess of low energy ν_e-like events observed by MiniBooNE. MicroBooNE will pioneer the software analysis tool that will be used in the phase 2 by the other detectors. It will provide better understanding of the detector effects (as such as noise, diffusion, recombination and more) and will develop fully automated ν_e and single photons selections.
In phase 2, the SBN program will implement the near and far detector structure with the SBND and ICARUS detectors, MicroBooNE will continue its data acquisition run and it will participate as a second far detector. The near detector called SBND is located 110 m from the BNB target. With a total active mass of 112 t of LAr its main role is to characterise the muon-neutrino beam before the oscillation. The Far detector, the ICARUS TPC, is situated 600 m from the beryllium target and has an active target mass of 476 ton liquid argon (total mass will be 760 ton). Near and far detector will be better described in upcoming sections. A summary of the SBN detectors is presented In Table 2.1 .
The expected beam-related background in the ν_eCC and ν_μCC channels is shown in Figure 2.4, corresponding to 6.6×10^{20} pots for SBND and ICARUS and 1.32×10^{21} pots for MicroBooNE.

2.1.1 Secondary goals

In addition to the neutrino oscillation searches, SBN is planned to perform neutrino-argon cross section measurements. In the SBN near detector, more than 2 million neutrino interactions per year will be collected in the active volume.
In addition to the measurements on the BNB neutrino beam, ICARUS detector is placed 6° off-axis of the higher energy NuMi beam, produced by 120 GeV protons from the Fermilab Main Injector onto a carbon target. ICARUS will be able to collect a large neutrino sample in the 0-3 GeV energy range with an enriched component of electron neutrinos. The SBN far detector will be able to collect $100,000$ ν_μ and $10,000$ ν_e NUMI off axis events per year. The combined high-precision measurements of the ν-Ar interactions will provide a crucial model for future LArTPCs experiments as such as DUNE.

2.2 The neutrino beam

The *Booster Neutrino Beam* (BNB) is created by extracting 8 GeV protons from the booster accelerator and impacting them on a 1.7λ beryllium target, to produce a secondary beam of hadrons, mainly pions. Charged secondaries are focused by a single toroidal aluminum alloy focusing horn that surrounds the target. It is supplied with 174 kA in 143 μs pulses in coincidence with the proton delivery. The horn will be able to be pulsed in both polarities,

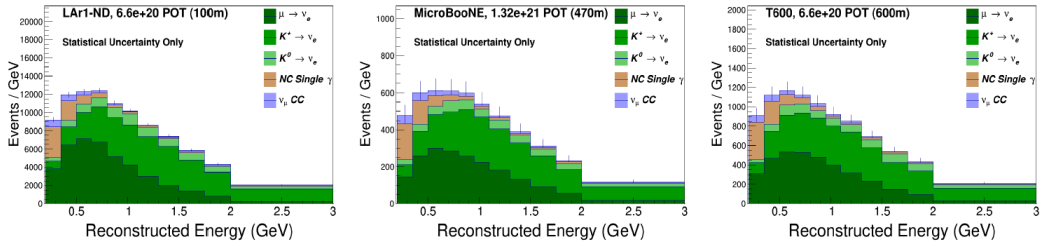

(a)

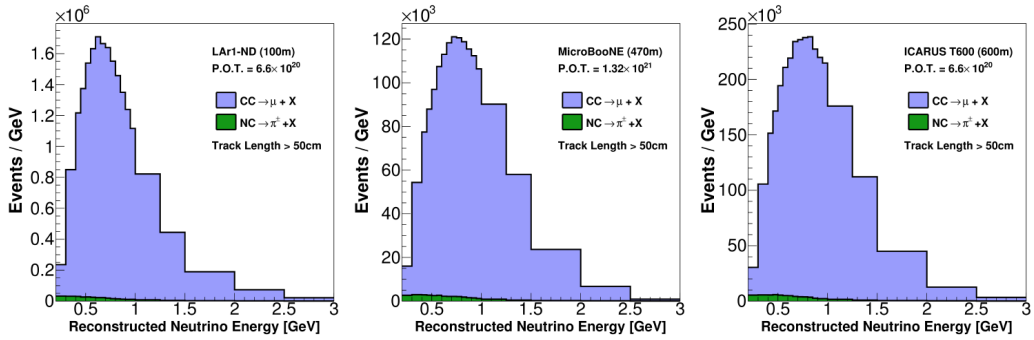

(b)

Figure 2.4: Beam related (*a*) ν_eCC candidate events and (*b*) ν_μCC candidate events in SBND (*left*), MicroBooNE (*center*) and ICARUS-T600 (*right*).

hence focusing either positive or negative mesons. This will be crucial in order to operate in anti-neutrino mode. Focused mesons pass through a collimator and then are allowed to propagate in the decay tunnel, a 50 m long, 0.91 m radius air-filled volume. In the decay tunnel the majority of the focused mesons will decay to produce muon and electron neutrinos. At the end of the tunnel, a 25 m concrete and steel plates wall will stop residual particles. The Booster spill length is 1.6 μs with $\sim 5 \times 10^{12}$ protons per spill delivered to the beryllium target. The main Booster RF is operated at 52.8 MHz, the beam is extracted into the BNB using a fast-rising kicker that extracts all of the particles in a single turn. The resulting structure is a series of 81 bunches of protons each $\sim$ 2 ns wide and 19 ns apart. This bunched beam structure can be exploited in order to obtain a more precise trigger for the LAr-TPCs.

The composition of the flux in neutrino mode (by focusing positive mesons) is energy dependent, but is dominated by ν_μ (93.6%), followed by $\bar{\nu}_\mu$ (5.9%), with an intrinsic $\nu_e/\bar{\nu}_e$ contamination at the level of 0.5% at energies below 1.5 GeV. The neutrino fluxes observed at the three different SBN detector locations are shown in Figure 2.5 and the $\langle E_\nu \rangle \sim 700$ MeV.

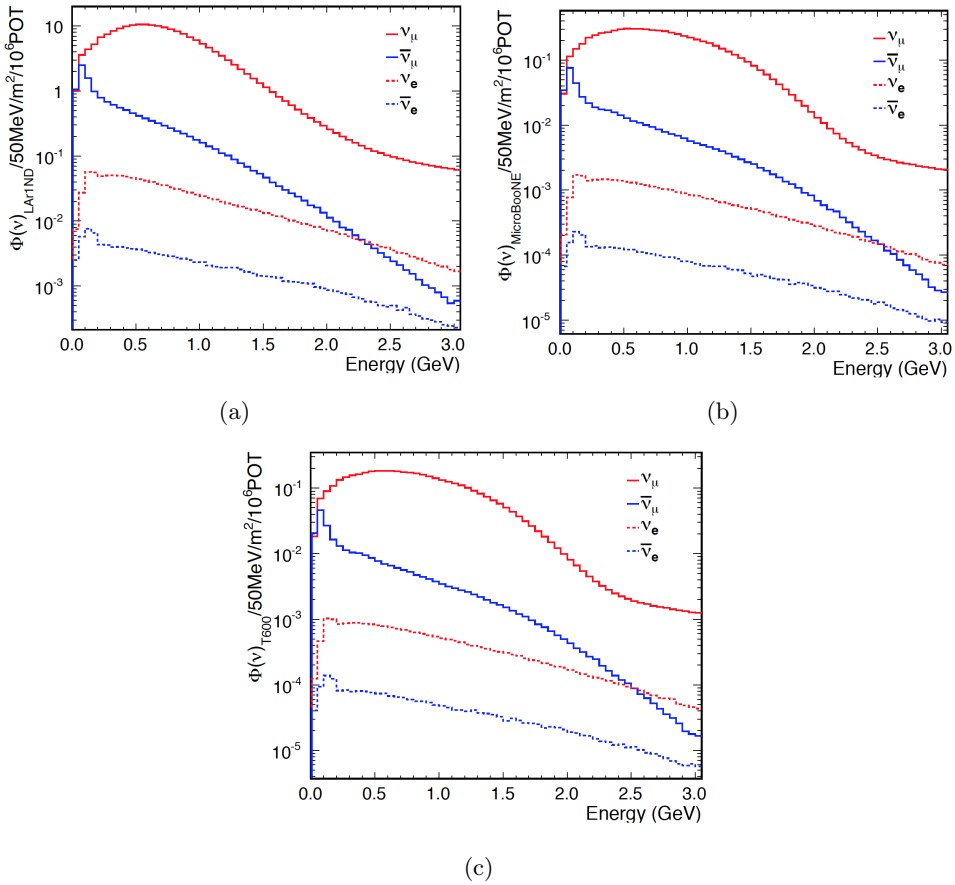

Figure 2.5: The Booster Neutrino Beam flux at the three SBN detectors: *(a)* SBND, *(b)* MicroBooNE and *(c)* ICARUS.

2.3 The liquid argon time projection chambers

The liquid argon time projection (LArTPC) chamber for neutrino detection is a design proposed by Carlo Rubbia in 1977 [52]. The detector consists in a large volume of pure liquid argon at the constant temperature of 87 K. The active argon mass is surrounded by a high voltage cathode surface on one side and an anode surface on the other side. Incoming neutrinos interact weakly with the liquid argon via both charged-currents and neutral-current interactions, the resulting charged particles ionize and excite argon atoms as they move in the medium. The ionization electrons are transported by the uniform electric field between the anode and the cathode surface, the uniformity is obtained by using an external field cage surrounding the active volume. A typical field strength is $\sim$ 500 V/cm. The drifting electron clouds generate small currents in the sensing wires collocated at the anode side of the detector. The wire pitch is usually between 3-5 mm. To obtain a 3-D reconstruction of the particle trajectories, multiple wire surfaces at different angles are used.

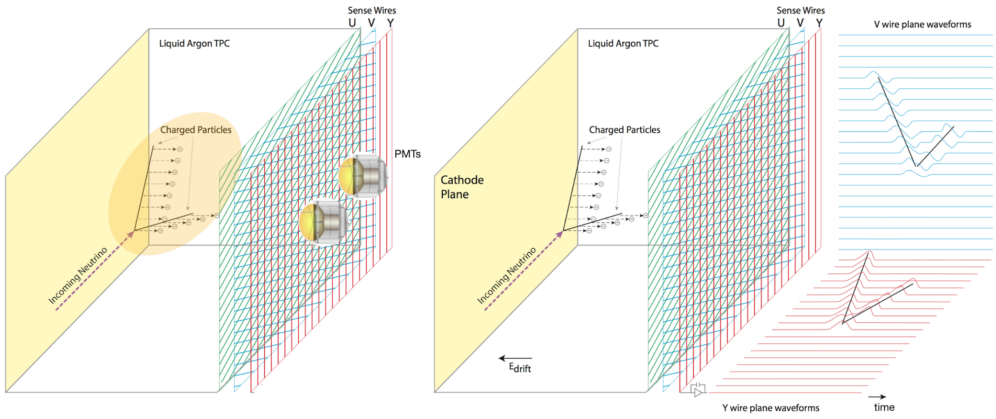

Figure 2.6: Operating principle of a LArTPC.

As drifting electrons go through the different wire surfaces, they produce a signal proportional to the total ionization of the emission location, hence, this detector can also provide detailed calorimetric measurements. In Figure 2.6 it's shown the operating scheme of a LArTPC.

The LArTPC is a totally active and continuously self-triggering detector characterised by high granularity and spatial resolution and able to provide 3D imaging of any ionizing event within the chamber. A downside of these detectors, due to the huge dimensions, is the readout-time: electron drift speeds are slow, around 1.6 mm/μs, hence for a detector of typically 2-3 m across, the readout time would be a continuous $\sim$ 1-2 milliseconds.
Excited argon atoms can scintillate by emitting light in the *vacuum ultraviolet region* (VEV), at λ =128 nm with E=9.69 eV, the liquid argon phton yield is $\sim$40000 γ/MeV. Light collection systems in LAr rely on wavelength shifting components as such as TPB (tetraphenyl butadiene) to obtain visible scintillation photons. A fast light signal is crucial in a time projection chamber as it would mark the t_0 of an interaction within the active volume, in order to measure the position along the drifting directions thanks to the constant electric field.

2.4 Near detector

The near detector is called *Short-Baseline Near Detector* (SBND) and its key role will be measuring the unoscillated BNB neutrino flux. The SBND hall is situated 110 m from the target facilities, the detector has an active volume of 5.0 m (L) $\times$ 4.0 m (W) $\times$ 4.0 m (H), divided in two different drift regions of 2 m, with a central cathode and two wire readout planes, as shown in the illustration in Figure 2.7.
The drift direction is perpendicular to the neutrino beam and the maximal drift length corresponds to about 1.3 ms drift time for the nominal drift field of 500 V/cm. Each drift node volume wire readout is built from two interconnected Anode Plane Assemblies (APAs). Each APA consists of three planes of 150 μm copper-beryllium wires at pitch and plane spacing of 3 mm. The second and third wire layer are rotated of $\pm$ 60° angles. The electronics readout consists of custom pre-amplifiers, commercial ADC's and motherboard with onboard FPGA

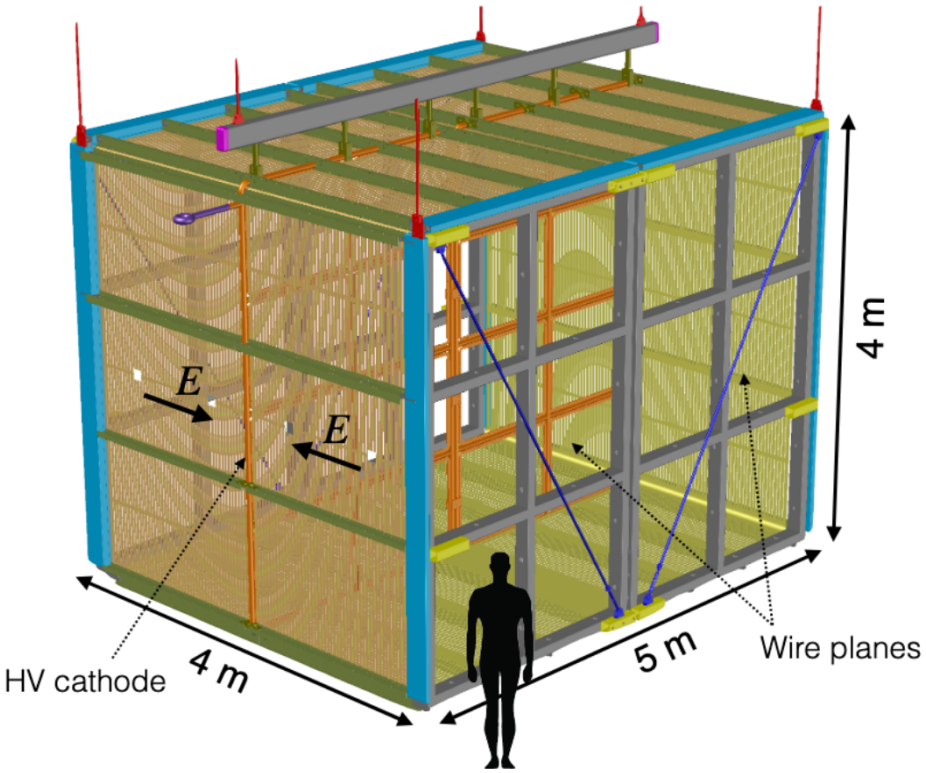

Figure 2.7: Sketch of the SBND TPC.

connected to the end of each wire plane and operating in liquid argon. The cathode bias will be −100 kV. The LArTPC will be encased in the field cage and then lowered inside a membrane cryostat [53].
SBND will use a composite photo-detection system: an array of 120 Hamamatsu R5912-mod PMTs, mounted behind the TPC wires and covered in wavelength shifting TPB, and the innovative ARAPUCA photon trap. ARAPUCA is a photon collection device composed of dichroic filter windows on a highly internal reflective box instrumented with silicon photomultipliers (SiPMs) [54].

SBND facilities are located in the surface, hence the fairly high cosmic ray contribute will have to be included in the background. In order to mitigate this background, SBND will be surrounded on all sides by planes of scintillator strips readout by SiPMs, which will act as a cosmic muon tagger. On top of this cosmic muon tagging system, the SBND facility will be covered with a 3 m concrete layer to reduce the cosmic rays. In Figure 2.8 it's presented the expected integrated total ν_eCC events background spectrum at the SBN near detector at the end of the data acquisition period, corresponding to 6.6×10^{20} protons on target; without an efficient cosmic background identification (on the left) and with a 95% cosmic background rejection (on the right).
The SBND detector is currently under construction and it is expected to begin commissioning in late 2020.

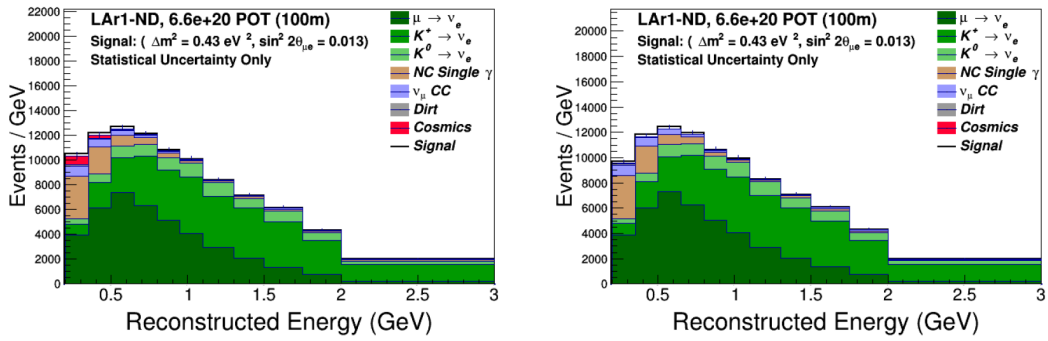

Figure 2.8: Electron neutrino charged current candidate distribution in SBND as a function of reconstructed neutrino energy. In the left only muon proximity and dE/dx cuts have been used to reject cosmogenic background events. In the right, a combination of the internal light collection system and external cosmic ray tagging system are assumed to identify 95% of the triggers with a cosmic muon in the beam spill time and those events are rejected. Oscillation signals are modelled on the $3+1$ LSND-like electron neutrino excess.

2.5 MicroBooNE

MicroBooNE is an 170 ton LArTPC and it is located 470 m from the neutrino beam target [55]. A picture of the detector is presented in Figure 2.9. The active region of the TPC is a rectangular volume of $2.33 \times 2.56 \times 10.37$ m^3 and its design allows ionization electrons from charged particle tracks to drift up to 2.56 m to a three-plane wire chamber [55].
MiniBooNE was a Cherenkov based detector and it was limited by photon misidentification background, by using a LArTPC technology. MicroBooNE was originally meant to be a standalone detector, aimed at lowering the background and improve the detection efficiency despite having five times less active mass compared to the previous experiment. The detector began its data acquisition run in 2015 and at the end of the data taking it will have enough statistic to provide sensitivity to a MiniBooNE-type signal at 3 or 5 σ above background. It is currently running in the same neutrino mode where MiniBooNE observed the electron neutrino excess and at nearly the same baseline of the previous experiment, allowing tests of models that predict a dependence of the MiniBooNE excess on the distance from neutrino source to detector.
MicroBooNE will participate as an intermediate baseline between the near and the far detector. At the end of the SBN program, MicroBooNE is expected to receive an exposure of 1.32×10^{21} pots protons on target in neutrino running mode from BNB, it will also record interactions from off-axis components of the NuMI neutrino beam.

Figure 2.9: Picture of the fully assembled MicroBooNE detector.

2.6 Far detector

The far detector is called ICARUS-T600 and currently this detector is the biggest LArTPC in the world, in Figure 2.10 it is shown a picture of the detector. This TPC has a total active mass of 476 liquid argon tons and it represents the major milestone towards the realization of multi-kiloton LArTPCs as such as DUNE. ICARUS (*Imaging Cosmic And Rare Underground Signals*) consists in a large cryostat split into two identical adjacent modules (T300), each module houses two TPCs made of three parallel wire planes, 3 mm apart and with the second and third rotated of $\pm$ 60° angles, the same design that was later proposed for SBND. Wires are made of stainless-steel and have a diameter of 150 μm. Each of the two T300 modules have a volume of 18.0 m (L) $\times$ 3.2 m (H) $\times$ 3.0 m (W). The maximal drift length is 1.5 m, equivalent to a $\sim$ 1 ms drift time for the nominal electric drift field of 500 V/cm [56].

2.6.1 ICARUS at LNGS

The ICARUS-T600 detector was first built and tested in Pavia, then, in 2004 it was moved in the hall B of LNGS. From October 2010 to December 2012, ICARUS collected about 3000 neutrino events on the CNGS neutrino beam, corresponding to 8.6×10^{19} protons on target. Neutrino events in the 10-30 GeV energy range have been recorded with unprecedented resolution, as it can be seen in Figure 2.11, demonstrating the high-level technical performances and the physical potentialities of LArTPCs. The events collected demonstrate also that the LArTPCs are very suitable detectors to the study of rare events, as such as neutrino events and proton decay searches, thanks to the high spatial granularity (resolution of $\sim$ 1 mm^3) and to the good homogeneous calorimetric response ($\sigma_E/E \approx 3\%/\sqrt{E(GeV)}$ for e.m. showers and $\sigma_E/E \approx 30\%/\sqrt{E(GeV)}$ for hadronic showers) [57].
After the testing run at LNGS, ICARUS was first disassembled and then, in 2014 it was

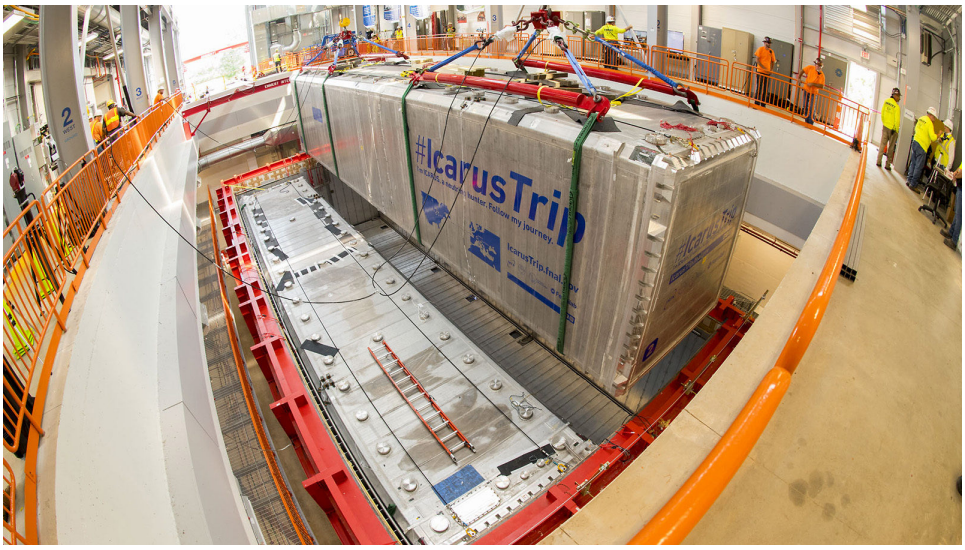

Figure 2.10: Picture of the ICARUS TPC being lowered in the Fermilab SBN far detector facilities, 2017.

moved to CERN and underwent a significant overhauling. The TPC received significant upgrades as such as an improved readout electronic, new scintillation light detection systems (the same PMTs installed in SBND) and the refurbishments of the cryostats and argon purification system.

2.6.2 ICARUS at FNAL

ICARUS will be the Far detector of the SBN experiment located in its dedicated facility 600 m from the BNB target. At the time of the writing of this thesis, ICARUS is installed inside the cryostats, operations of liquid argon filling will begin in the upcoming month, in Figure 2.12 it is shown a recent picture of the far detector TPC encased in the cryostat and waiting

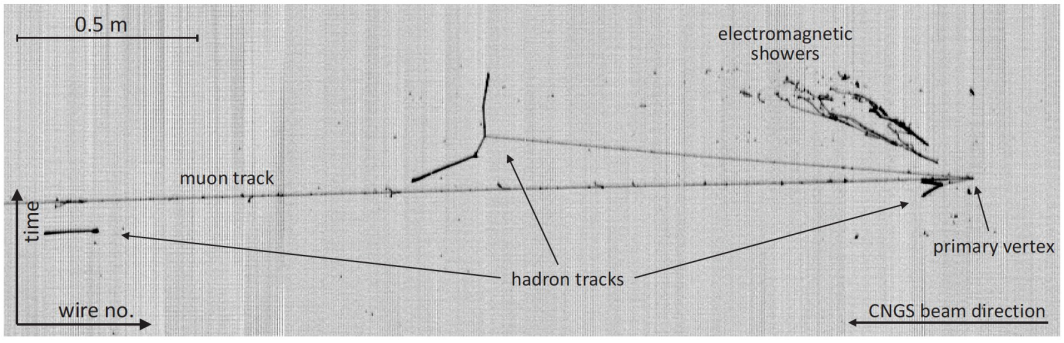

Figure 2.11: CNGS ν_μ CC interaction at the ICARUS T600 detector at LNGS.

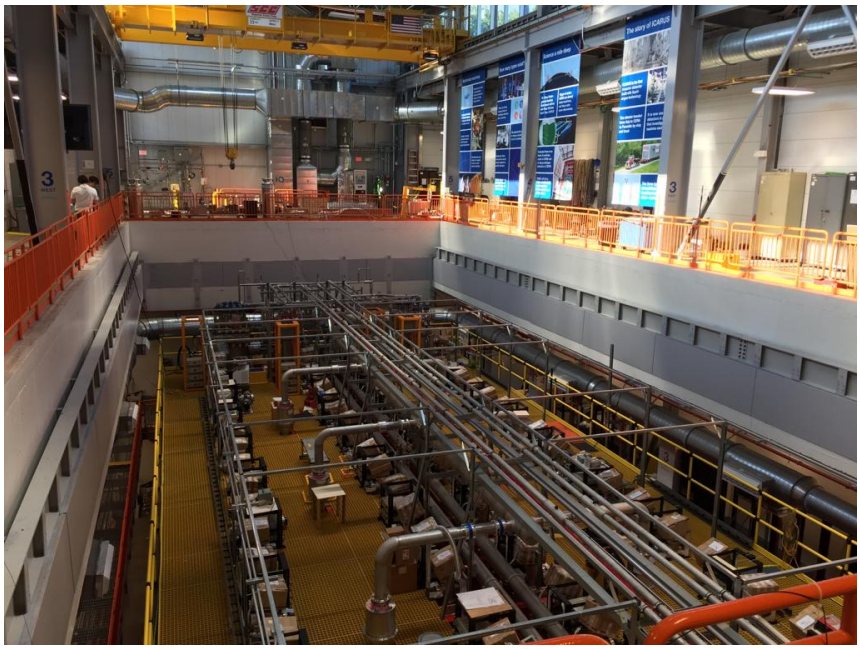

Figure 2.12: Recent picture of the SBN far detector facility. The ICARUS TPC is already encased in the cryostat.

for the liquid argon.
ICARUS-T600 was first designed to operate in the low cosmic background and deep underground conditions of the LNGS, covered by 1400 m of Gran Sasso rocks. The SBN conditions will be completely different, at Fermilab the detector will be placed few meters deep and the cosmic rays background may induce several additional and uncorrelated triggers during the ∼1 ms readout window of the huge TPC. This will be a problem since, in order to reconstruct the position of the track in the TPC, it is necessary to associate the different timings of each track in the reconstructed image to their own specific delay with respect to the trigger. High energy cosmic muons that create secondary showers may also produce isolated ionizing background electrons or positrons with similar energies. The far detector facility is covered with a 3 m concrete roof to mitigate some of the cosmic rays.
It is expected that at the energies of the BNB neutrino beam, the intrinsic ν_eCC contamination occurs at the rate of $\sim$ 500 ν_eCC/y, while a possible LSND-like oscillation signal will produce a few hundred ν_eCC/y ($\sim$ 170 events per year for Δm^2=0.43 eV^2 and $\sin^2 2\theta$) [58][59].

The cosmic ray background on the far detector will be very high, the whole ICARUS-T600 it is expected to observe a rate of $\sim$ 25 kHz events. The cosmic muon rates in coincidence with the beam trigger window of 1.6 μs will be 0.83×10^6 cosmic events per year, in particular, based on the ICARUS measurements on surface level, during the 1 ms readout window of the TPC, $\sim$ 11 cosmic rays tracks are expected over the full T600.
In Figure 2.13 (*left*) it is presented the total ν_eCC events background spectrum expected after an exposure to 6.6×10^{20} protons on target. The picture on the right describes the same ν_eCC background spectrum with a 95% cosmic ray tracks identification.

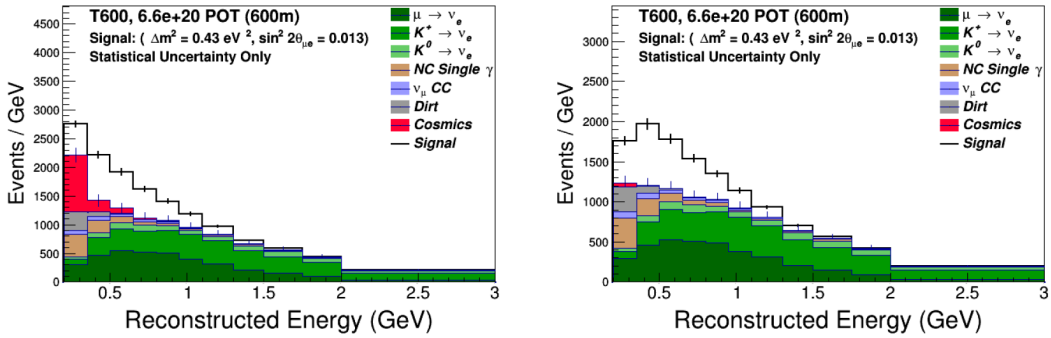

Figure 2.13: Electron neutrino charged current candidate distribution in ICARUS as a function of reconstructed neutrino energy. On the left the cosmic ray induced background is present. On the right, the same distribution is shown with a 95% cosmic tracks identification.

2.6.3 The cosmic background

One of the most important sources of background to the ν_e analysis is created by cosmogenic photons produced by cosmic muons propagation through the detector and nearby surrounding materials. This background can be produced first of all by cosmogenic events in coincidence with the beam spill, *"Timing case A"*, but also by interactions occurring anytime within the acquisition time corresponding to the maximum electron drift time: in fact if a cosmogenic photon interacts anywhere inside the drift time and a different cosmogenic event is in coincidence with the beam spill, the photon could be mistaken for the in-spill event, *"Timing case B"*. The potential cosmogenic backgrounds can be also categorised on the basis of the presence, *"Topology I"*, or absence, *"Topology II"*, of the parent particle in the TPC active volume (AV).
If we gather category A and category B events with at least one photon shower above 200 MeV in the active volume, $\sim 4 \times 10^5$ events are expected in a three years data acquisition run. Three different offline selections, tested on Monte Carlo simulations, can be performed in order to reduce this number:

- A fiducial volume cuts of 25 cm from the sides of the active volume, 30 cm from the upstream face and 50 cm from the downstream; from simulations, 62% of the photons survive.
- Study of the dE/dx in the initial part of the shower to discriminate photons from electrons; a reduction of the photon component by a factor ∼10 is expected.
- Distance from the muon track: rejecting event candidates with a reconstructed vertex inside a cylindrical volume of 15 cm radius around each muon track; it's expected a rejection of $> 99\%$ of the background photons above 200 MeV.

In Table 2.2 the expected background is presented per each category before and after topological cuts. The selection cuts reduce the cosmogenic background to 200 events, over a 3

Interaction description	Timing	Topology	Before cuts	After cuts
γ in spill, primary μ enters AV	A	I	32600	21
γ in spill, primary misses AV	A	II	11	<5
γ in drift, primary misses AV	B	I	225000	179
γ in drift, primary misses AV	B	II	60	<8
Total cosmogenic γ backgrounds			258000	200
Intrinsic ν_e CC			1500	1500
Signal ν_e CC near best fit			∼500	∼500

Table 2.2: Background rates, before and after topological cuts, assuming 3 years of data taking for a total of 6.6×10^{20} pot, delivered in 1.32×10^{8} beam spills equaling 211 seconds of beam time. Events with at least one photon shower above 200 MeV converting in the fiducial volume are counted in all the γ entries.

Figure 2.14: Picture of the PMTs installation behind the wire plane.

years period of data taking to be compared with the intrinsic ν_e background.
In order to obtain the proposal sensitivity to the $\nu_\mu \rightarrow \nu_e$ appearance channel, a 95% cosmic ray track identification is required. To this end ICARUS-T600 requires three new features:

- a new light collection system, to allow a better event timing and more precise localization;
- a more precise beam-related trigger system, to exploit the BNB bunched beam structure;
- an external cosmic ray tagging system, to identify entering charged tracks with position and timing information.

2.6.4 New light collection system

The ICARUS TPC requires a light collection system able to detect efficiently the prompt scintillation light from event with energy depositions down to $\sim$ 100 MeV.

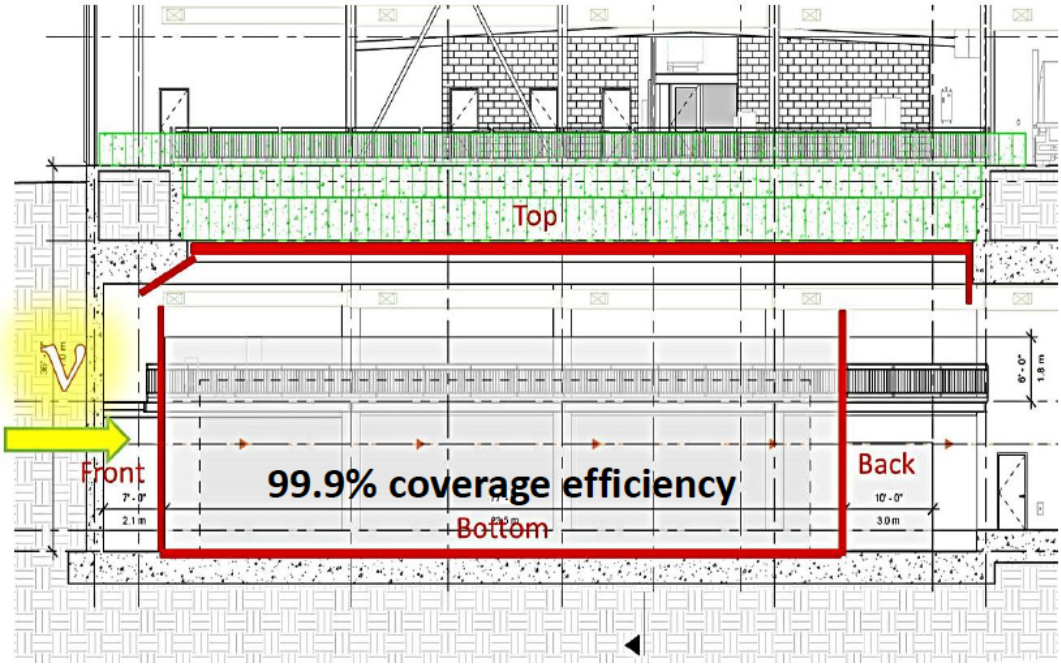

Figure 2.15: 4π geometry of the far detector CRT system.

The light collection system has to allow the localization of the tracks associated with every light pulse along the 20 m of the longitudinal detector direction, with an accuracy better than 50 cm, which is smaller than the expected average spacing between cosmic muons in each TPC image. In this way, the light collection system would be able to provide the absolute timing for each track, and to identify the events in coincidence with the neutrino beam spill. The timing resolution of the incoming event is expected to be at 1 ns level.
The solution for the photo-detection system will rely on large surface Photo-Multiplier Tubes (PMT) with hemispherical glass window of 200 mm diameter, manufactured to work at cryogenic temperatures. As SBND, the far detector TPCs will rely on the Hamamatsu R5912-mod PMTs.
The light collection system consists in 360 Hamamatsu PMT installed behind the wire planes. In Figure 2.14 it is presented a picture of the PMTs deployment on the side of one of the TPCs.

2.7 The Cosmic Ray Tagger

The *Cosmic Ray Tagging system* (CRT), represented in Figure 2.15, is a sub-detector external to the LArTPC whose task is to identify charged tracks before they reach the TPC. It will consist in a 4π geometry plastic scintillator detector and it will have to provide a 99.9% coverage in order to provide, together with the other sub-detectors, a combined cosmic ray track identification of 95%.

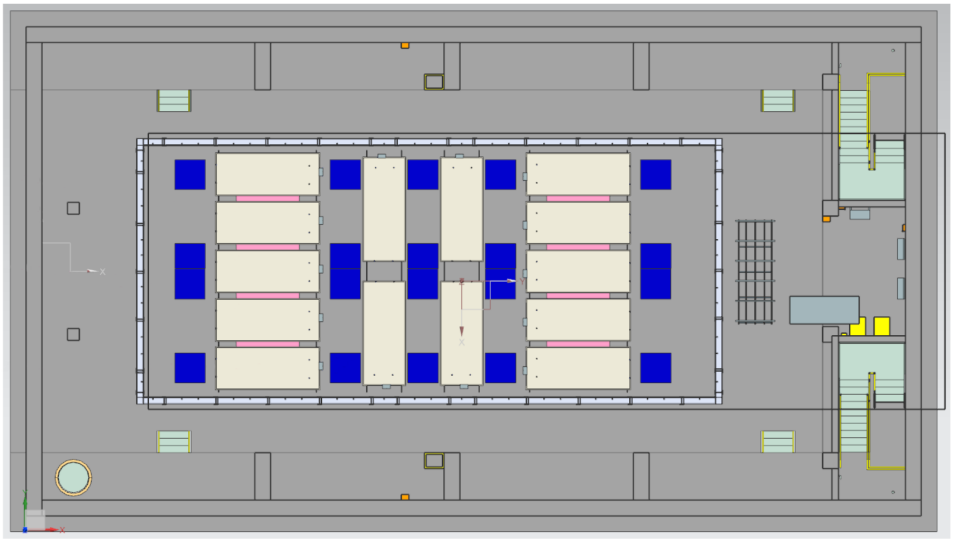

Figure 2.16: Bottom CRT layout, each scintillation module is illustrated as a yellow rectangle.

The CRT system is divided into three different sub-systems, each covering a different region of the TPC: Top CRT (covering the top side), Side CRT (covering the sides) and Bottom CRT (covering the bottom). Each sub-system will be different according to the expected cosmic ray frequency. The cryostat will be covered with $\sim$ 1100 m^2 of plastic scintillators.
The CRT system will have to provide spatial and timing coordinates of the tagged particle, these information will be gathered in the data acquisition system and they will be matched with the corresponding track in the TPC.
A detailed description of the Top CRT will be provided in the next chapter.

2.7.1 Bottom CRT

The Bottom CRT, whose layout is shown in Figure 2.16, consists of 14 modules situated under the warm vessel. The modules are the same ones used for the Double Chooz veto, they consist of two layers of parallel scintillator strips, each 5 cm wide. A wavelength shifting fibre is placed in the center of each strip to collect scintillation light and to guide it towards the PMT. Each module is composed by 32 strips read out by a 64-pixel multi-anode PMT. The overall dimensions of each module is 4 m $\times$ 1.6 m $\times$ 3.2 cm.
The modules where shipped from France to Fermilab in spring 2017 and were installed in summer 2017, Figure 2.17.

2.7.2 Side CRT

The Side CRT system will provide the coverage of the four sides of the detector: north, east, west and south, a representation is presented in Figure 2.18.
The scintillators are the same used for the MINOS cosmic veto. Each module's dimensions

Figure 2.17: Picture of the currently installed Bottom CRT modules.

are 8 m × 80.5 cm × 1 cm. They are composed of 20 bars per module (each 4 cm wide). The bars are glued to and wrapped in a light-tight aluminum skin. Light is collected by one wavelength shifting fibre per bar, readout on both ends. On the long sides and on the north side (beam exit) the panels will be mounted in two parallel layers to allow for noise reduction. Position resolution along the bar will come from time difference between readout signals on both ends.
Each fibre is read by a SiPM (Hamamatsu S14160-3050HS). The front end electronic will be common to the MicroBooNE CRT, SBND CRT and to the Top CRT system.

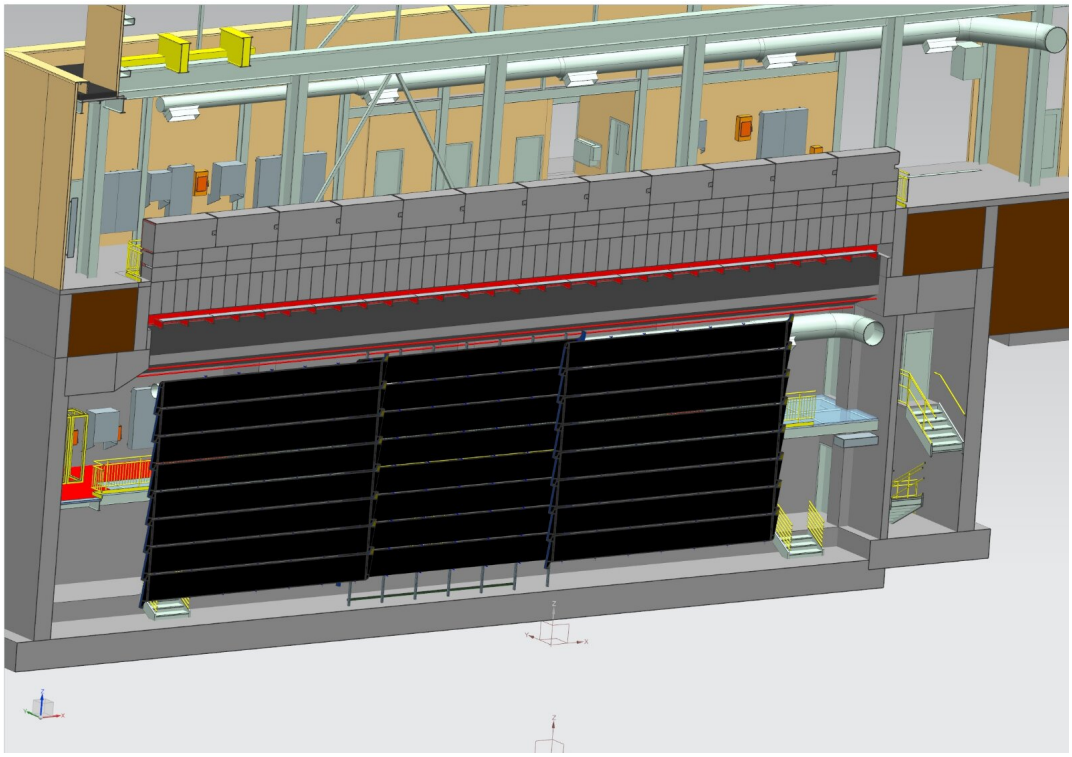

Figure 2.18: Section of the far detector facility with west Side CRT highlighted (black).

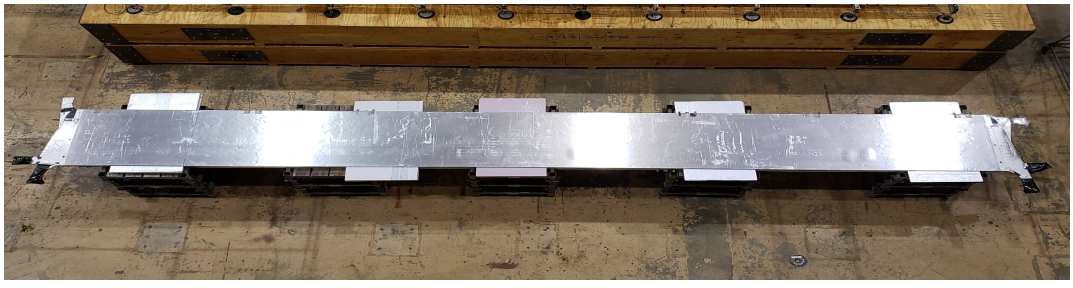

Figure 2.19: Picture of one of the Side CRT modules.

Chapter 3

Cosmic Ray Tagger

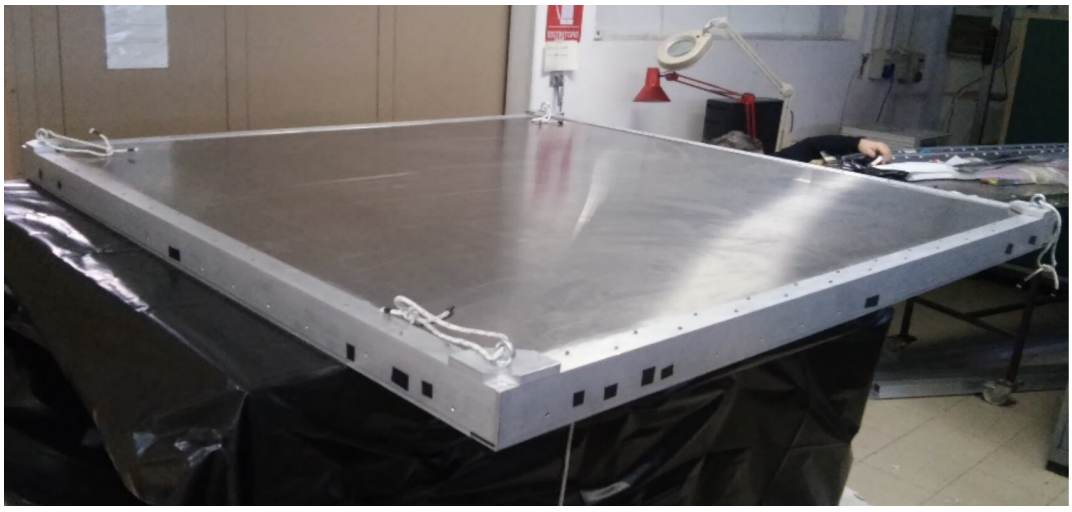

Figure 3.1: The CRT prototype assembled in Bologna laboratories.

The Top CRT sub-system development is entrusted to the CERN and INFN groups. The first prototype assembled in Bologna is shown in Figure 3.1.
The Top CRT is designed to intercept 80% of the cosmic muons that will produce background events in the ICARUS LArTPC, the expected rate of $\sim$ 25 kHz [50]. The coverage of the ICARUS TPC will be provided by 123 CRT modules: 84 modules to cover the top of the cryostat and 39 modules will be installed vertically to cover the top perimeter of the TPC; a scheme of the planned installation is Figure 3.2.
This thesis is focused on the activities I performed on the CRT sub-detector under the supervision of the Bologna group.

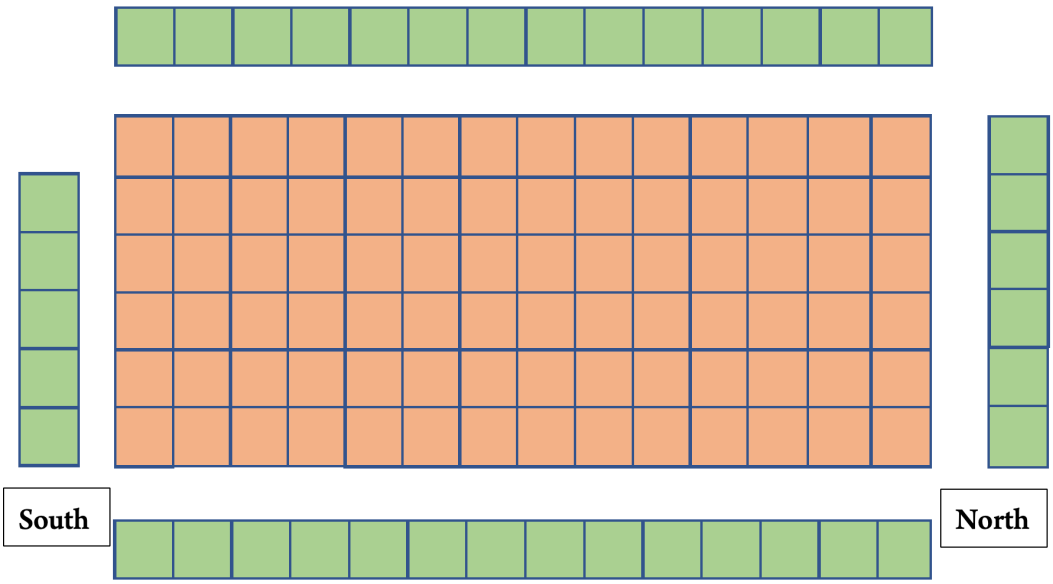

Figure 3.2: Illustration of the CRT modules that will be installed at the far detector facilities. Orange modules will be placed horizontally on top of the cryostat, green modules will be installed vertically.

3.1 The CRT modules

The assembly of the CRT modules is done at the Frascati National Laboratories (LNF). A sketch of the CRT module is shown in Figure 3.3. The bottom of the module consists of a 1.86 $\times$ 1.86 m^2 squared aluminum base (2 mm thick) riveted to an underlying aluminum support. The bottom layer perimeter is covered in black sponge-like tape in order to cover the rivets and prevent light from coming through their holes. A black foam-like plastic sheet separates the scintillator layers from the aluminum structure. In Figure 3.4 (a) and (b) A picture of the bottom layer of the CRT and a detail of the covered rivet holes is presented in Figure 3.4 (a) and (b).
Underneath the aluminum sheet, micro-coaxial cables are connected to a PCB patch panel at one end and at the other they pass through dedicated holes in the aluminum base, ready to be connected to the scintillators. The first scintillator layer is composed of eight 15 mm thick ISMA scintillators. Once the bars are in place, a PCB is connected to the SiPM pins and to the micro-coaxial cables. Pictures of the first layer of scintillator bars and details of the PCB connection are shown in Figure 3.5. As it can be seen in Figure 3.5 (a), each scintillator has a barcode and two labels referring to the glued Silicon Photomultipliers (SiPMs). As it will be explained later on, the information of each module will be stored in a common database. A second layer of black foam-like plastic sheet covers the first scintillator layer. Eight 10 mm thick scintillators produced by NUVIA are placed orthogonal to the first layer compose the second scintillator layer. SiPM-PCB connections are made also on the top layer.
The scintillator bars sides are wrapped with black Tedlar strips to prevent reflected light from reaching the scintillators and the SiPMs. The strips are then taped and the top layer is

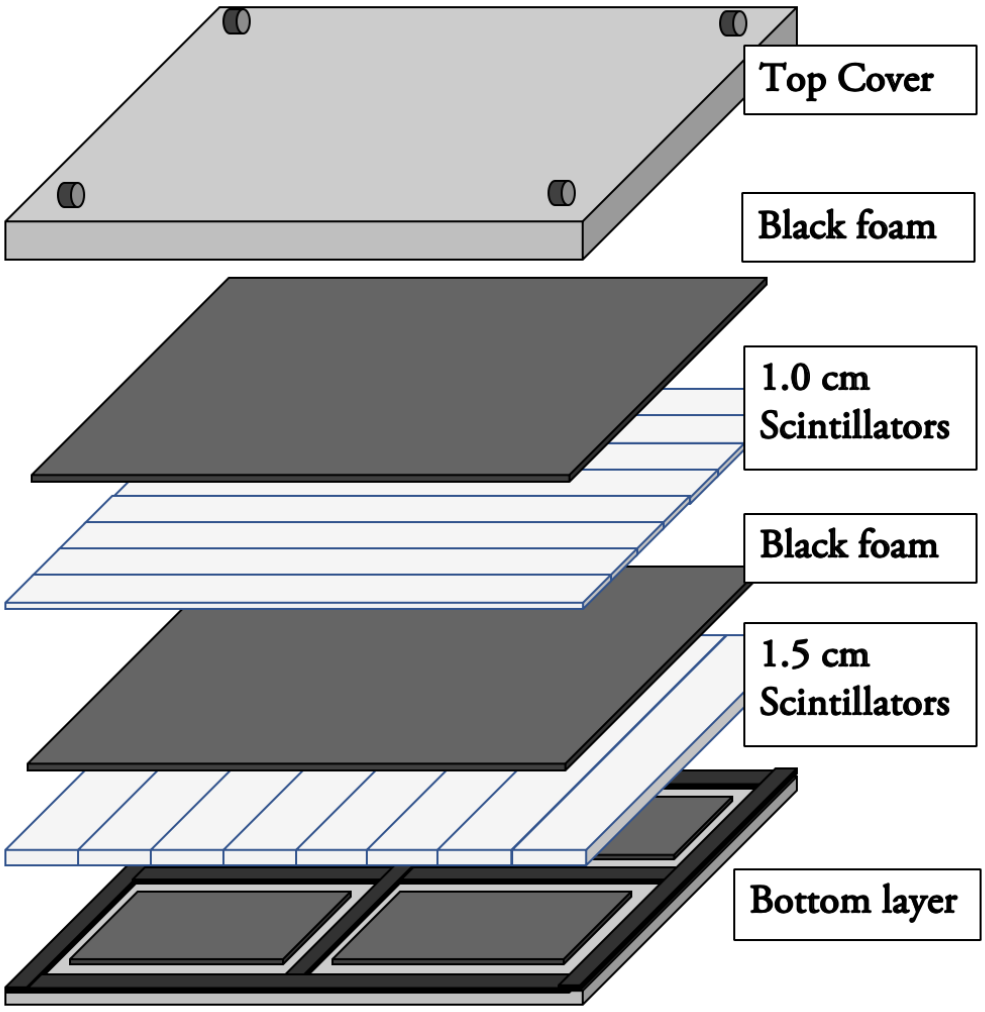

Figure 3.3: CRT module with its different components.

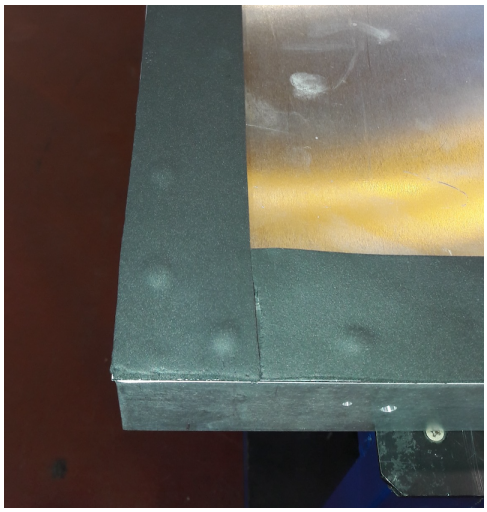

(a)

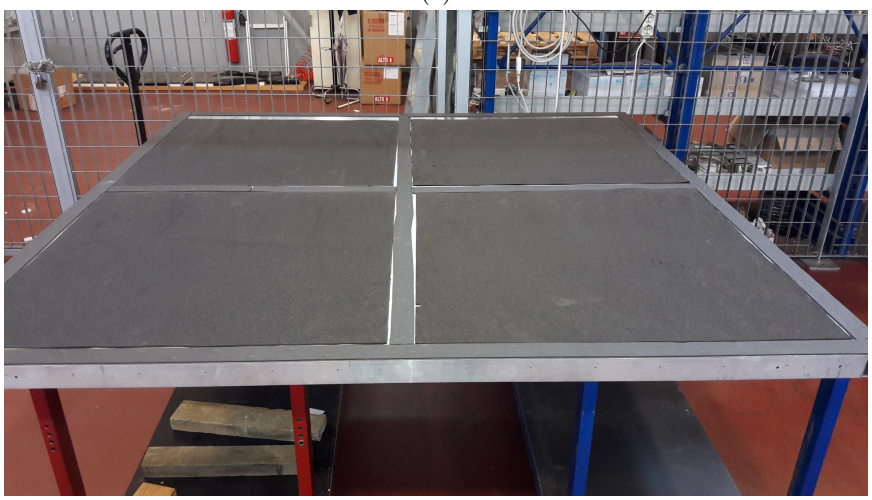

(b)

Figure 3.4: (*a*) Detail of the the black sponge-like tape covering the rivet holes, (*b*) the bottom layer.

covered with black foam-like plastic sheet. A picture of the two scintillator layers wrapped in Tedlar and ready to be closed is shown in Figure 3.6.
Once the two scintillator layers are wrapped, the top cover of the CRT module is then slowly laid down to match the packed scintillator and firmly tightened with plugs and several screws per side. The completed module weights $\sim$ 160 kg and it has to be moved by an overhead travelling crane in the construction hall.
Once a CRT modules is completed and successfully tested, it is assigned a barcode number and its informations are stored in a dedicated SQL database. The modules are then placed in dedicated racks ready to be moved for the transportation. A picture of a completed rack, which hosts a maximum of ten modules, is shown in Figure 3.7.

(a)

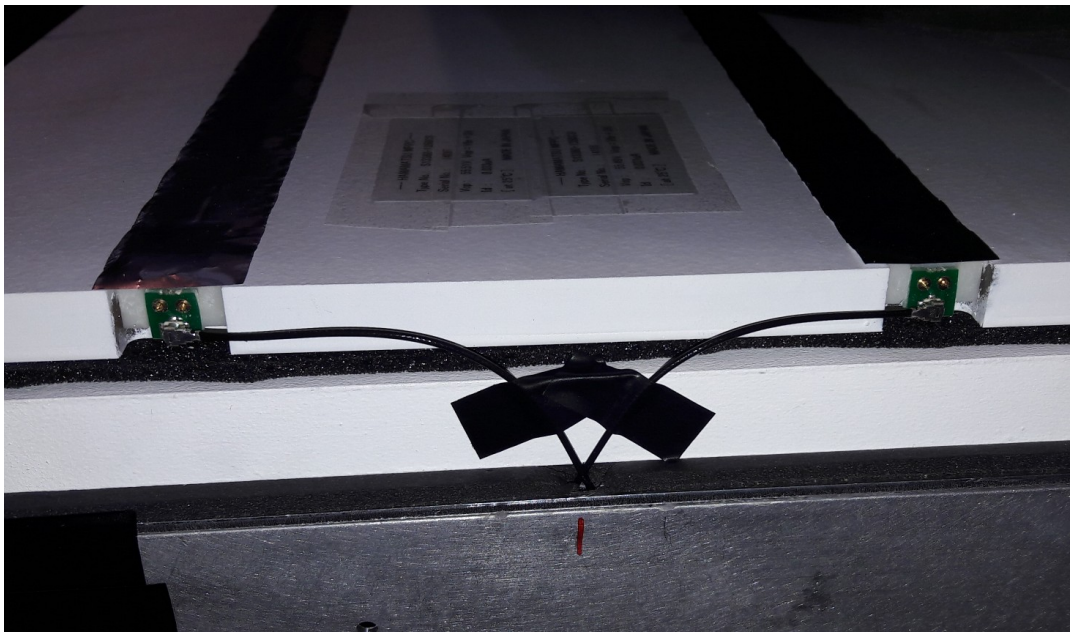

(b)

Figure 3.5: Pictures of (*a*) the first layer of scintillator bars and (*b*) a detail of the connection of the micro-coaxial cables to the SiPM PCB.

3.2 Scintillators

Scintillators are materials that exhibit the property known as luminescence, when they are exposed to certain forms of energy as such as light, heat or radiation, they absorb and reemit the energy in the form of visible light. Generally, these detectors are coupled to light collection devices as such as PMTs or SiPMs. Above a certain minimum energy, most scintillators behave in a near linear fashion with respect to the deposited energy, hence the light output

Figure 3.6: Picture of the two scintillator layers wrapped in Tedlar and black foam-like plastic sheets.

of a scintillator is directly proportional to the exciting energy.
The readout of the CRT modules is performed on one end of the scintillator thanks to two SiPMs per bar.
The two scintillator layers differ both in terms of thickness and of materials. The top scintillator are 23 cm wide, 184 cm long and 10 mm thick, produced by the NUVIA company in Czech Republic. A picture of the 10 mm scintillators is shown in Figure 3.8 with a detail of the SiPM connector and socket.
The bottom polyvinyltoluene scintillators are 23 cm wide, 184 cm long and 15 mm thick, they are produce by the Institute for Scintillation Materials (ISMA) in Ukraine.
Overall, $\sim$ 2000 plastic scintillators will be used for the CRT.

3.3 Wavelength Shifting fibres

Wavelength Shifting (WLS) optical fibres are used to collect the light produced in each scintillator strip. In wavelength shifters a fluorescent organic molecule (*dopant*) absorbs a short-wavelength incident photon and isotropically emits a secondary photon with a longer wavelength. This reemission process can be exploited in order to inject light into a fibre through its sides. The WLS fibre consists of two components: a core with a refractive index of n_{core} $\sim$1.60 and a cladding with $n_{cladding}$ 1.49. Only $\sim$4% of the light is trapped by the fibre. An illustration of the light absorption and reemission inside a WLS fibre is shown in

Figure 3.7: Picture of a full rack of ten completed CRT modules in the assembly hall at LNF.

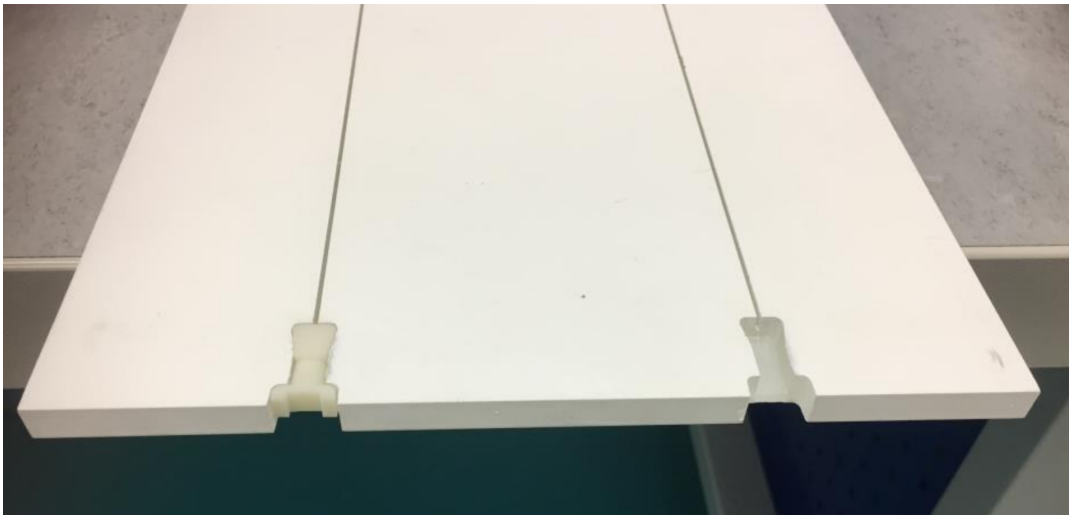

Figure 3.8: Picture of the 10 mm Nuvia scintillators, with a detail of a SiPM connector on the left and the empty socket on the right.

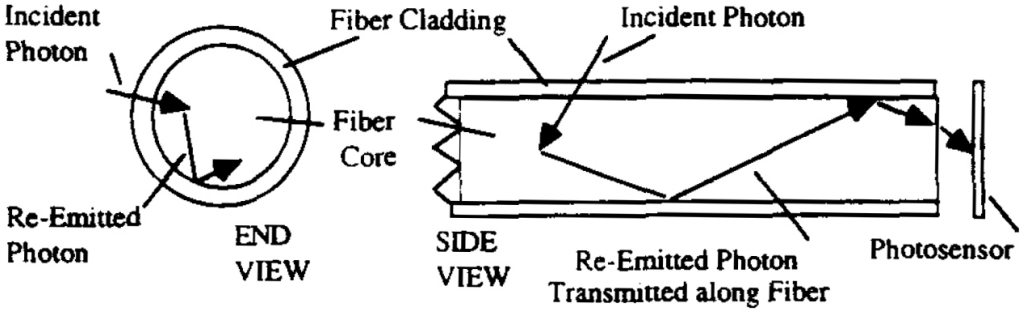

Figure 3.9: Schematic illustration of light absorption and reemission within a WLS fibre.

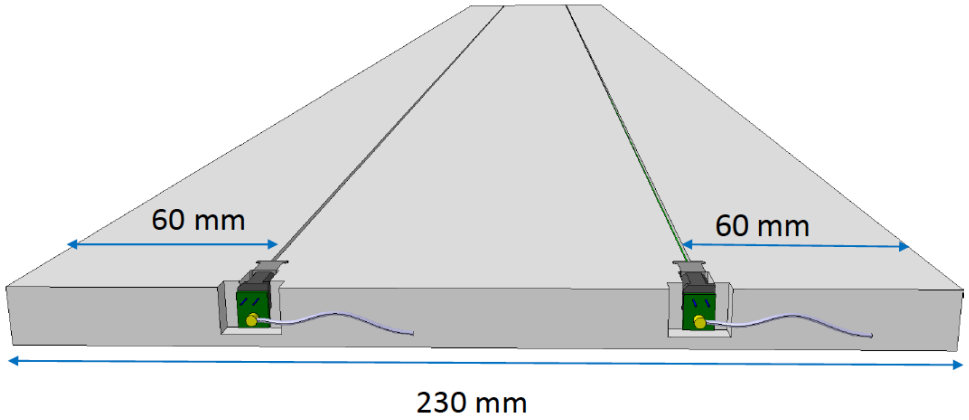

Figure 3.10: Illustration of the fibres disposition along the scintillator bar.

Figure 3.9.
The WLS fibres used in the CRT scintillators are Kuraray Y-11(200), with an absorption peak at 430 nm, an emission peak in the green at 476 nm and an attenuation length greater than 3.5 m [60]. The fibres are read-out only from one end, the opposite end-side of the fibre is mirrored in order to enhance the light yield. The mirroring consists in polishing the end of the fibre and then coating it with aluminum reflective layers of a few micron thickness by aluminum spattering in vacuum.
An illustration of the WLS fibres embedded in the CRT scintillator bars is sketched in Figure 3.10: two fibres, each one distant 60 mm from the edge of the scintillator, are glued in 2 mm deep grooves in the bar.
A total number of $\sim$ 7400 m fibres will be used for the CRT system.

3.4 Silicon Photo-Multipliers

SiPMs are single photoelectron sensitive devices based on single-photo avalanche photodiodes arrays (APDs), placed on a common silicon substrate. Each APD is called *pixel*, it is reverse-biased above the breakdown voltage V_{br} and it operates in Geiger mode. When a photon of sufficiently high energy reaches the depleted region of the photodetector, it produces an electron-hole pair due to the photoelectric effect, an electric field is then used to separate and drift the carriers. The Geiger discharge is obtained when the electric field generated within the depletion region is sufficiently high that the drifted carriers produce secondary ionization along their drifting path, this leads to an high gain, typically $G \sim 10^6$. An illustration of an avalanche photodiode is shown in Figure 3.11 (a). Each pixel, or microcell, is coupled with the others by a metal quenching resistor that limits the current drawn by the photodiode during the breakdown discharge, and hence lowers the reverse voltage to a value below the diode breakdown voltage. The cycle of breakdown, avalanche, quench and subsequent reset of the bias to a value above background is illustrated in Figure 3.12.
Each pixel, in parallel with the others, detects photons independently. The sum of the discharge current from each cell combines to form a quasi-analog output and it can provide

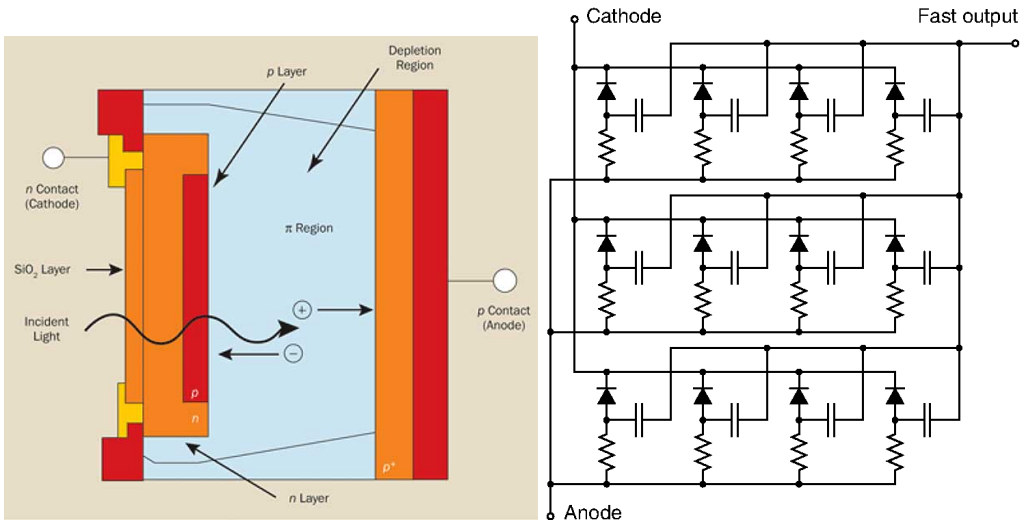

(a) (b)

Figure 3.11: (*a*) Sketch of an APD and (*b*) the electric circuit of an array of microcells.

informations on the magnitude of an incoming photon flux, hence the output signals have an amplitude proportional to the number of detected photons. A simplified circuit that describes an array of microcells is shown in Figure 3.11 (*b*).
With respect to the PMTs, SiPMs have several advantages:

- insensitivity to magnetic fields;
- low bias voltage, typically $\sim$ 50 V;
- sensitivity to single photons;
- low cost.

SiPMs operates at an over-voltage $\Delta V_{ov} = V_{bias} - V_{br}$ from 1 to 5 V over the V_{br}.
The Photon-Detection Efficiency (PDE) of the SiPMs is limited by several contributes:

- the geometric efficiency of the cell (fill factor F), which is defined as the ratio between the active area and the total area of the sensor, which depends on the gaps between the microcells;
- the quantum efficiency, which is the probability of a photon generating an electron-hole pair in the active region of the detector;
- the probability that a carrier triggers an avalanche;
- the recovery time of the pixel.

The gain of a cell is the ratio of the output charge to the charge of an electron. The output charge can be calculated from the over-voltage and the micro-cell capacitance C:

$$G = \frac{C\Delta V_{ov}}{q} \quad . \tag{3.1}$$

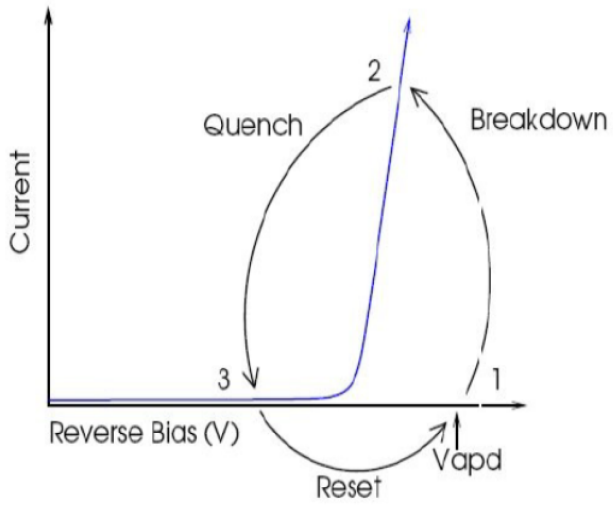

Figure 3.12: Breakdown, quench and reset cycle of a photodiode working in Geiger mode.

Each detected photon results in a highly quantized output pulse. An ADC can integrate the pulse, the resulting peaks due to the successive numbers of detected photons will be clearly visible in the spectrum. An example of photo-electrons spectrum, obtained during a test run on one of the SiPMs used for the CRT bars, is shown in Figure 3.13. From the spectrum, it is possibile to easily distinguish the different peaks, corresponding to a different number of detected photoelectrons. As it will be described in upcoming sections, one of the analysis performed during this thesis project consisted in obtaining Light-Yield measurements from the photo-electron spectra of different scintillator bars.

3.4.1 SiPM noise

The main source of noise that limits the SiPM single photon resolution is the dark current. The dark current is due to the thermally generated electrons that trigger an avalanche in the high field region, hence they generate a signal which is indistinguishable from a photon generated one. The probability of thermally generating electrons is proportional to the temperature T:

$$P(T) = CT^{3/2}e^{-\frac{E_g}{2K_BT}} \quad . \tag{3.2}$$

Another important source of noise is the optical cross-talk between microcells. This noise arises when photons emitted during the breakdown avalanche in one cell travel to the neighbour cells and trigger a second avalanche, as illustrated in Figure 3.14. This process happens instantly and single photons may generate signals equivalent to multi photon events. The optical cross-talk probability is proportional to the SiPM over-voltage.
Another possible source of noise are after-pulses. This phenomenon happens when carriers trapped in metastable traps during a discharge are released with a certain delay and they

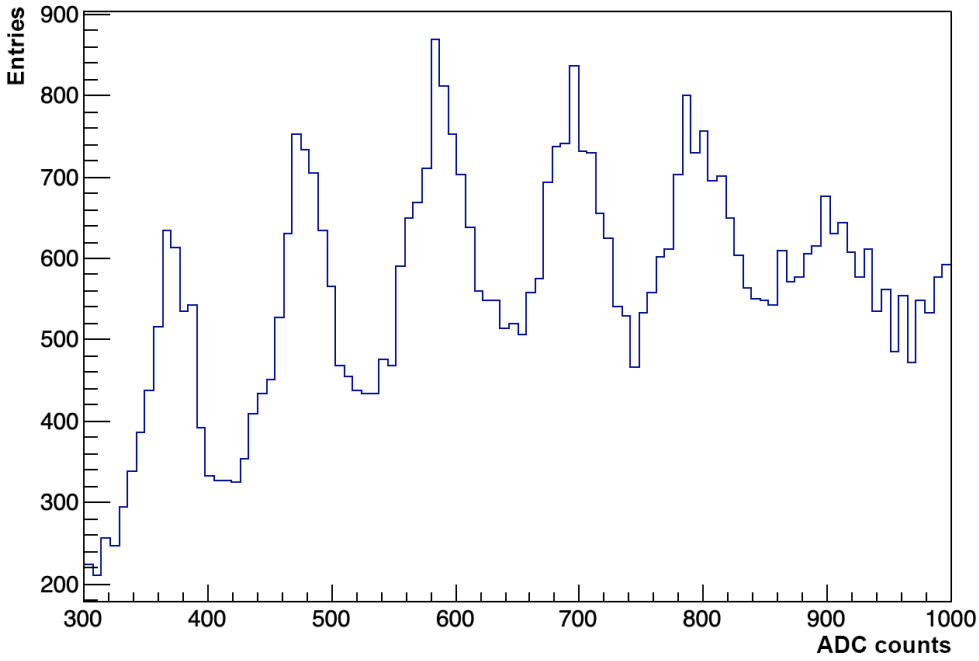

Figure 3.13: Photo-electrons spectrum of one SiPM installed in one bar of the CRT scintillators.

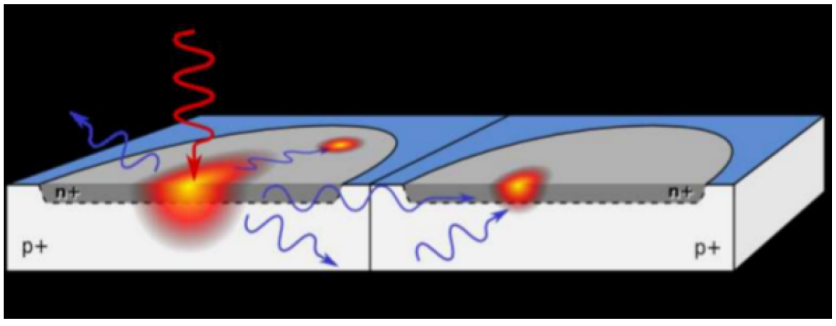

Figure 3.14: Illustration of the optical cross-talk phenomenon.

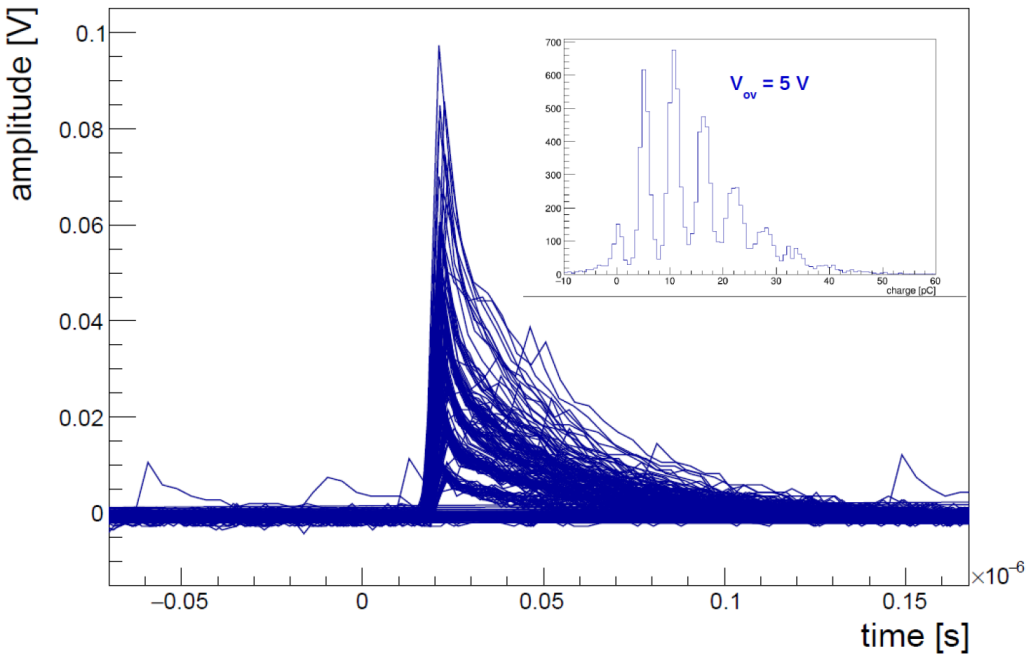

Figure 3.15: Hamamatsu SiPM test using pulsed light from a LED with a frequency of 10 kHz.

trigger a new avalanche. The resulting output signal of the SiPM presents a first pulse followed by a second one with a delay that can last from nanoseconds up to several microseconds.

3.4.2 CRT SiPMs

The SiPMs used on the CRT scintillators are the Hamamatsu S13360-1350CS Multi-Pixels Photon counters, with an active area of 1.3 × 1.3 mm^2 [61]. The pixel pitch is 50 μm, for a total of 676 cells per SiPM. The fill factor F is 74% and the V_{br} is 53 ± 5 V. The cross-talk probability is ∼ 3% and the photon detection efficiency is ∼ 40% at 450 nm. The SiPMs were tested at CERN by measuring the dark current rate (∼90 kHz) and the gain. This latter measurement was performed by illuminationg them with a pulsed light from a LED with a frequency of 10 kHz. A superimposition of the illuminated SiPM waveforms is shown in Figure 3.15, the signals of consecutive numbers of photoelectrons are clearly visible.
Overall, 4000 Hamamatsu SiPMs will be used and tested during the construction of the CRT system.
The SiPMs are glued to a SiPM-holder connected to the scintillator bar and to the wavelength shifting fibre. SiPMs pins are connected to a PCB and routed via 50 Ω micro-coaxial cables 1.8 m long, carrying both signal and bias voltage to a PCB patch panel connected to the Front End Board. In Figure 3.16 (a) and (b) an illustration of the fibre-SiPM coupling and a picture of the Hamamatsu SiPM are presented.

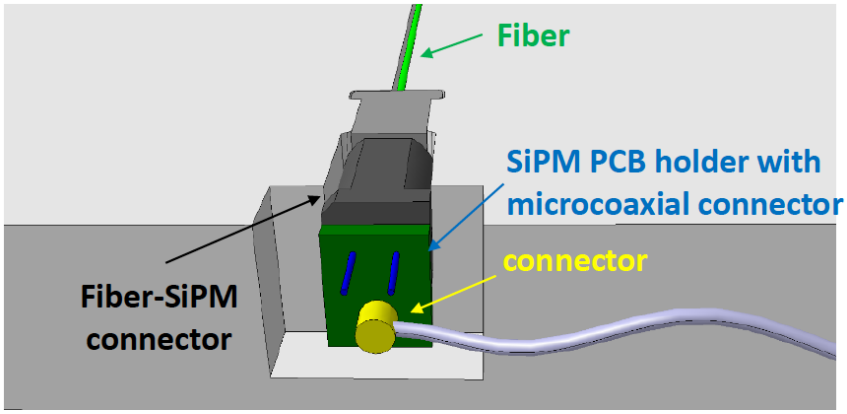

(a)

(b)

Figure 3.16: (*a*) Illustration of the SiPM connection scheme to WLS fibre, (*b*) picture of the Hamamatsu SiPM.

3.5 Front End Board

The Front End Board (FEB) used in the CRT modules is common to the Side CRT and to the SBND CRT system. The board is a multi-channel custom design developed by the Albert Einstein Center for Fundamental Physics of the University of Bern for the readout of 32 SiPMs used in veto system of liquid argon neutrino experiments [62]. The developed FEB was commercialised by CAEN [63].
The analog input signal is processed by a 32-channel ASIC (*CITIROC*). For each channel the chip provides charge amplifier with configurable gain, fast shaping with the peaking time of 15 ns and slow shaping with configurable peaking time in the range of 12.5 ns to 87.5 ns. Signal from the fast shaper is discriminated at configurable level and produces digital signals (T0-T31) for event triggering. These 32 signals are routed to a XILINX Spartan-6 FPGA chip, where the basic input coincidence and triggering logic is realized. The board comunicates with the host computer through ethernet protocol.
Two pictures of the FEB are shown in Figure 3.17 (*a*) and (*b*).

(a)

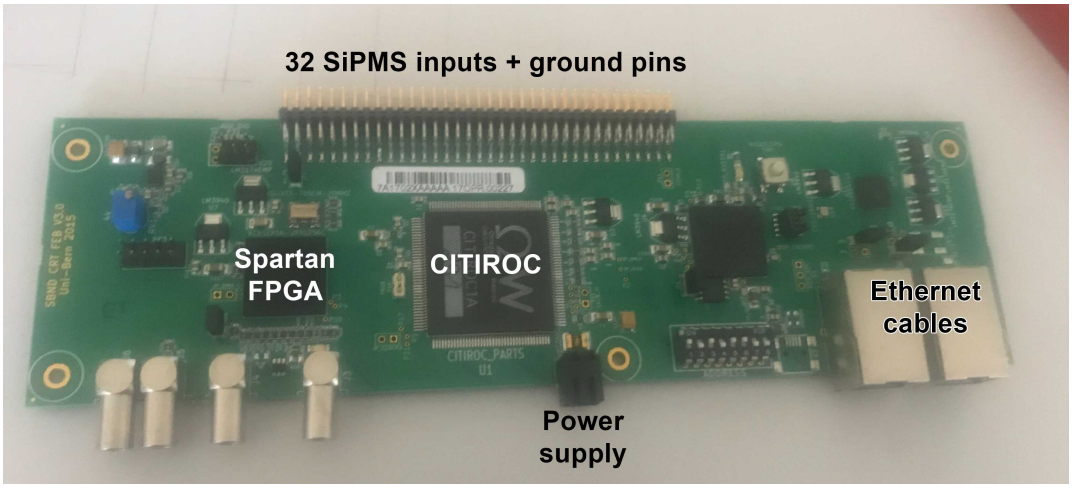

(b)

Figure 3.17: Picture of (a) the FEB in it's case and (b) the FEB internal components.

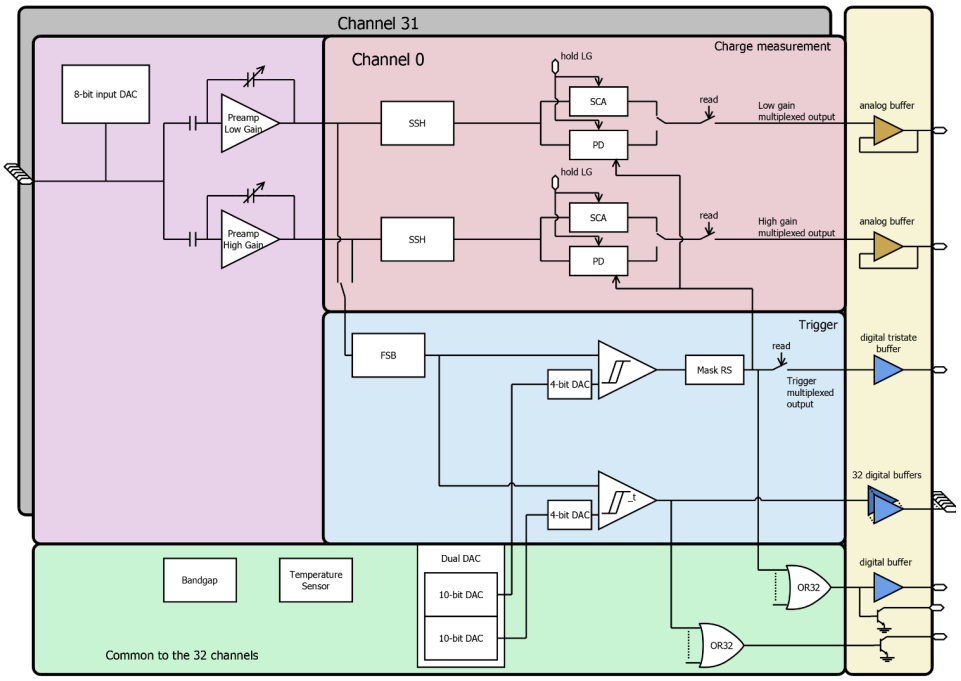

Figure 3.18: Architecture of the front-end CITIROC

3.5.1 CITIROC

The *Cherenkov Imaging Telescope Integrated Read Out Chip* (CITIROC) is a 32 channels fully analog front end ASIC dedicated to readout of SiPM detectors. CITIROCs are the evolution of EASIROC chips and, as the name suggests, they were first developed for SiPMs used in Cherenkov imaging. The processing of the analog signal takes place in the front-end channels of the device, while the read-out is handled at the internal back-end of the ASIC. Two separate electronic chains allow for high-gain and low-gain simultaneous processing of the analog signal.
Each of the two chains, whose architecture is presented in Figure 3.18, is composed of an adjustable preamplifier followed by a tunable shaper (SSH, slow shaper), a track-and-hold circuit (SCA, switched capacitor array) and an active peak detector (PD, peak detector) to capture and hold the maximum value of a signal. Fine-tuning of each pixel gain is obtained by adjusting the voltage applied to the SiPM through an 8-bit digital-to-analog converter ranging from 0 V to 4.5 V.
A third chain implements the trigger channel generation using a fast shaper (FSB, bipolar fast shaper) with fixed shaping time of 15 ns. All CITIROC main parameters can be programmed by downloading a configuration bit-string through a slow control-serial line.

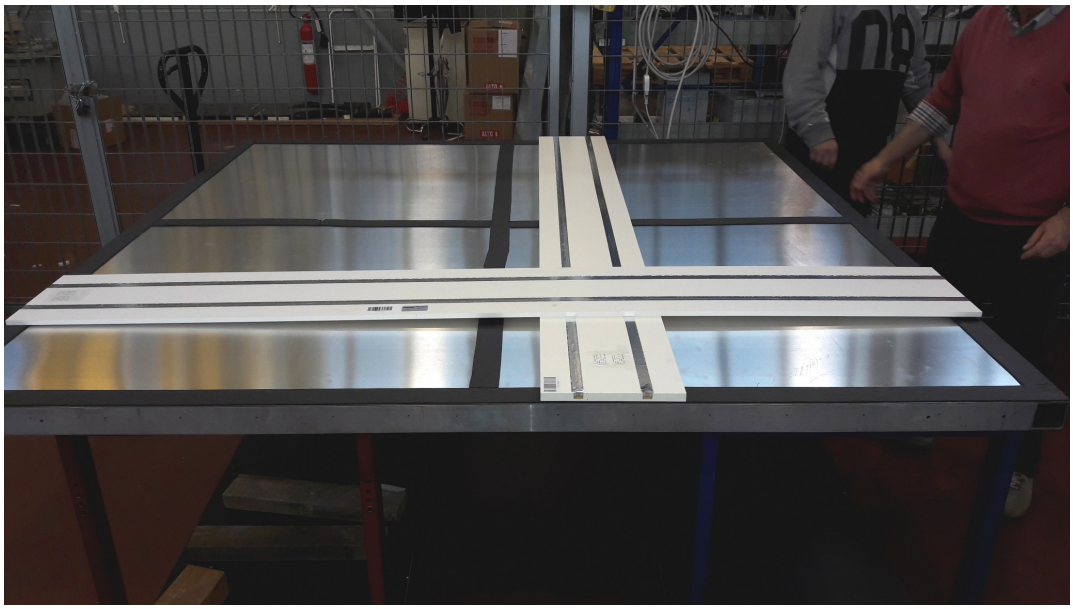

Figure 3.19: Picture of a possible geometrical coincidence of crossing bar within the CRT module.

3.5.2 Triggering logic

One of the main features of the CRT modules will be providing detailed topological informations of crossing muons. By using and X-Y scintillator layers configuration, it is possible to obtain 64 23 $\times$ 23 cm^2 coincidence of crossing bars (windows) within the module, since each layer is composed by 8 bars. A possible coincidence window inside the CRT module is shown in Figure 3.19 as the cross of two orthogonal scintillator bars that trigger after the passage of a cosmic muon.
The block-scheme of the trigger formation circuit is presented in Figure 3.20. For each of the 32 channels, the CITIROC ASIC provides a charge amplifier with a configurable gain and dynamic range of 1 to 2000 p.e., the amplified signal goes through a fast shaper of 15 ns and the shaped signal is then binarized with a discriminator. The threshold for the discriminator is is supplied by 10-bits DAC, common for 32 channels plus 4-bits DAC, individual for each of the 32 channels for fine tuning. The 32 trigger signals (C0 to C31) are in LVCMOS logic (3.3V active state) and they are routed to the FPGA where they are paired with AND logic to form coincidence signals for each of the two fibres from the same scintillator bar (coincidences of even-odd channels, e.g. C0&C1, C2&C3, etc...).

The primary event trigger is obtained as the OR of the resulting coincidences of even-odd channels of a scintillator layer in an AND coincidence with the OR signals of the other layer. Within the FPGA this signal triggers the generation of a time stamp for the event. Each of the 32 discriminators can be individually enabled or disabled by the CITIROC configuration bit stream. The bit stream is produced by on-board CPU on the basis of the configuration command, received via Ethernet link from the host computer.
In Figure 3.21 it is presented the triggering diagram of the circuit. The primary event trigger, after a delay of 50 ns, triggers a HOLD signal to memorize instantaneous signal levels at all

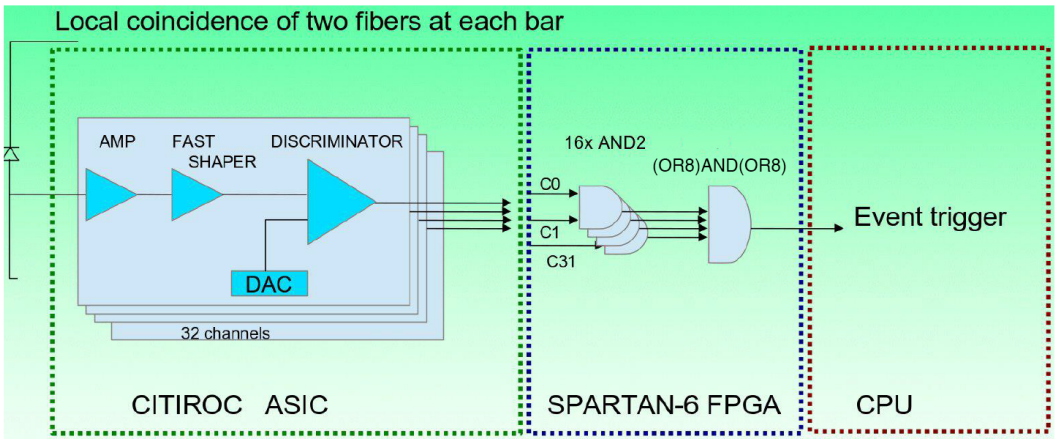

Figure 3.20: Block-scheme of FEB triggering circuit.

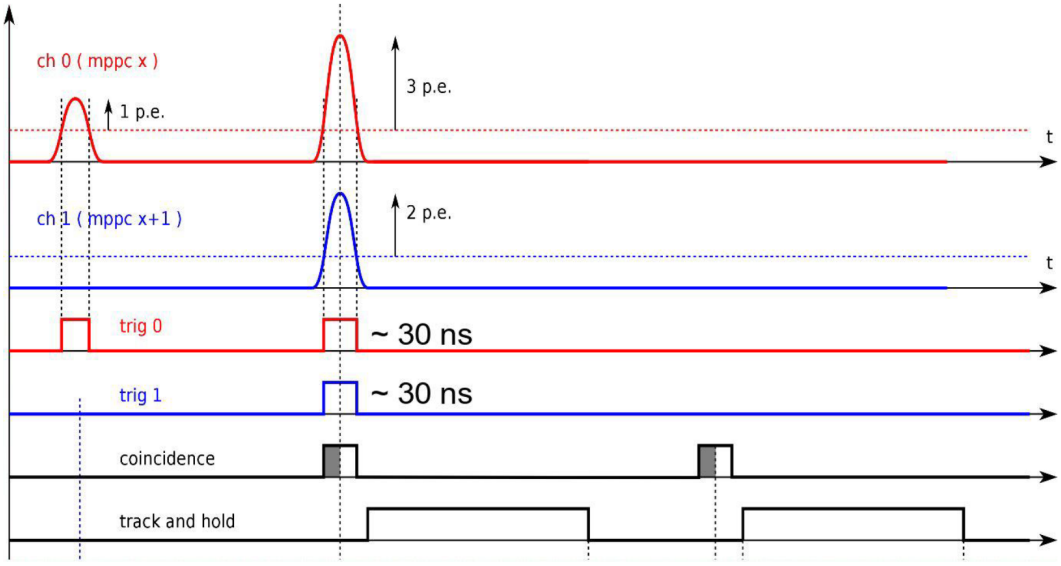

Figure 3.21: Timing diagram of the triggering circuit.

32 channels at moment of the top of the peak, the same signal is sent to the *TOUT* LEMO connector on the FEB. The HOLD signal defines the read-out window of the FEB, it is kept in an active state for at least 150 ns. If during this period the circuit detects high level at the input *TIN* LEMO connector on the FEB, the event is considered valid and the HOLD signal is kept high for 22 μs until the CPU finishes digitization cycle and reset it to its initial state. If no TIN signal is received, the HOLD signal is reset by the FPGA and the event is discarded. TOUT is always reset to low state after 150 ns.
An additional feature of the triggering logic is the possibility to select an individual channel trigger where the primary event trigger is the logic OR of the active channels (e.g. C0||C1||...||C31).

3.5.3 Time stamp

The TDC (Time to Digits converter) of the time stamp generator is composed of a coarse counter working at the clock frequency of 250 MHz and a delay-chain interpolator that improves accuracy down to 1 ns. For each event, the FEB is capable of recording two independent time stamps with reference to a positive signal on the *T0* and the *T1* LEMO connectors. The T0 input accepts PPS (Pulse Per Seconds) signals coming from a GPS.
Each time stamp is a 32-bits word, having time information in 30 LSBs (Least Significant Bytes), two MSB (Most Significant Bytes) are used for flagging special events. Two different special events are foreseen.
The first special events corresponds to the arrival of the reference signal to one of the T0 or T1 inputs. At such event, the time passed from the previous analogous event is recorded and the timing circuit is reset to zero. This allows to measure the period between reference signal and, in case the real period is stable and accurate, the measured period allows to derive deviation of the internal on-board oscillation frequency from nominal values.
The second special events happens in the absence of the reference pulse for more than 1074 ms, which leads to an overflow of the coarse counter. This special event can be used for offline software analysis to invalidate the time stamp for the next period, until the reference pulse is restored.

During the SBN program data acquisition runs, it will be possibile to use the *White Rabbit* as the time reference on T0. The White Rabbit is an open source system that relies on ethernet technology, it exploits a hierarchy-like structure between the nodes of a network: a designated node operate as a *master* and it is responsible for keeping all the other nodes synchronised. The external time is fed into the master from high-precision atomic oscillators via GPS satellites, this exact time is digitally attached to data packages that constantly are exchanged in the network. By sending the time tags back and forth between nodes, the system can calculate the time delays it takes for data to travel through the cables and correct them, keeping all the nodes in synchronisation with the correct time and ensuring experimental events are kept coordinated.

3.5.4 Standalone DAQ

In order to perform a real time testing of the CRT modules, a simplified version of the data acquisition software based on the ROOT toolkit is used. In the upcoming sections of this thesis, it will be referred to this simplified software as *Standalone DAQ*, as it works on one FEB only at the time, in order to distinguish it from the *Multifeb DAQ*, that can work on

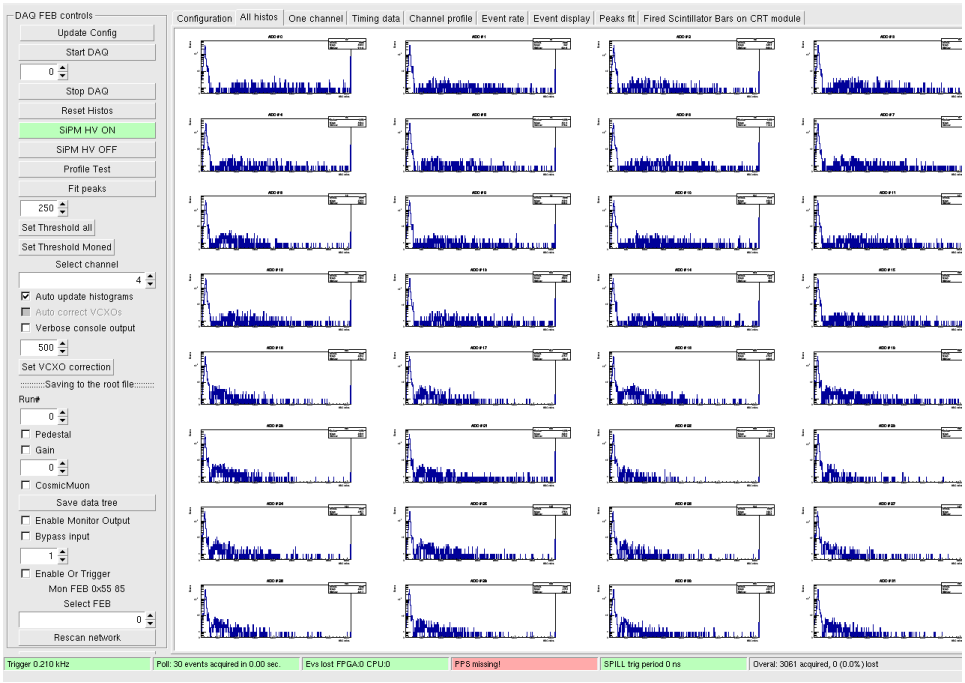

Figure 3.22: A screenshot of the user interface of the standalone DAQ software. The charge integrated spectra of all the 32 SiPMs channels obtained in a the test run of the CRT prototype are displayed.

multiple-FEBs connected in daisy chain via Ethernet cables.
The standalone DAQ is provided of a GUI, a screenshot of which is presented in Figure 3.22. Once the FEB is connected to the computer via Ethernet cable, the standalone DAQ downloads a default CITIROC file configuration in the FEB which loads the values for the SiPM gain and bias and enables channels amplifier of the channels that participate in the trigger. Using the GUI it is possibile to easily modify the parameters of the CITIROC configuration file. In Figure 3.23 (a) and (b) two screenshots that highlight how to modify some of the parameters during the data acquisition are shown. The standalone DAQ can provide a real time monitoring of all 32 of the SiPMs, as was shown in Figure 3.22, or a single channel visualization, as it's shown in Figure 3.24. Several plots from single channel monitoring will be presented in the upcoming sections of this thesis, for clarity the *ADC value* is referring to the ADC counts, where 200-215 digits corresponds to 0.5 photoelectrons. The first photoelectron peaks is around 400 ADC counts.
Different trigger configurations can be obtained with the standalone GUI, but they are all limited by the FPGA internal logic. In Figure 3.25 an example of trigger on a single geometrical coincidence of two crossing bars is presented. In this DAQ run, the trigger was obtained as the coincidence of one scintillator of the top layer (channels 4 and 5) and one scintillator of the bottom layer (channels 24 and 25).
Thanks to the standalone GUI it is easily possible to turn on and off the High Voltage of the SiPMs as well as starting and interrupting the DAQ. Another useful feature is the possibility

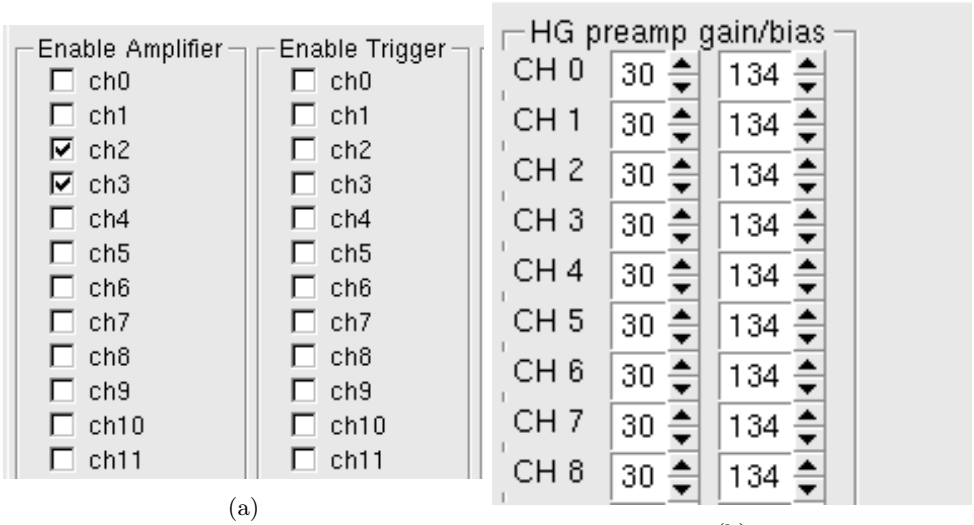

(a) (b)

Figure 3.23: GUI details of (*a*) the amplified channel selection and (*b*) the single channels pre-amplification and gain expressed in ADC counts.

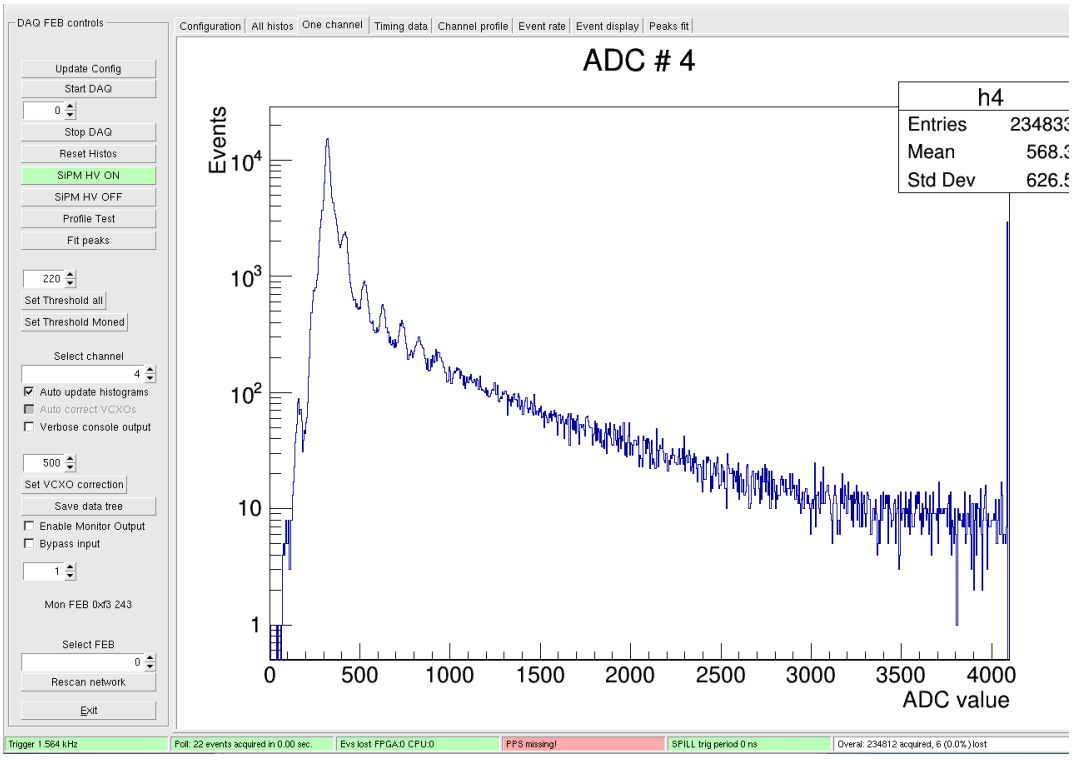

Figure 3.24: Screenshot of single channel monitoring tab.

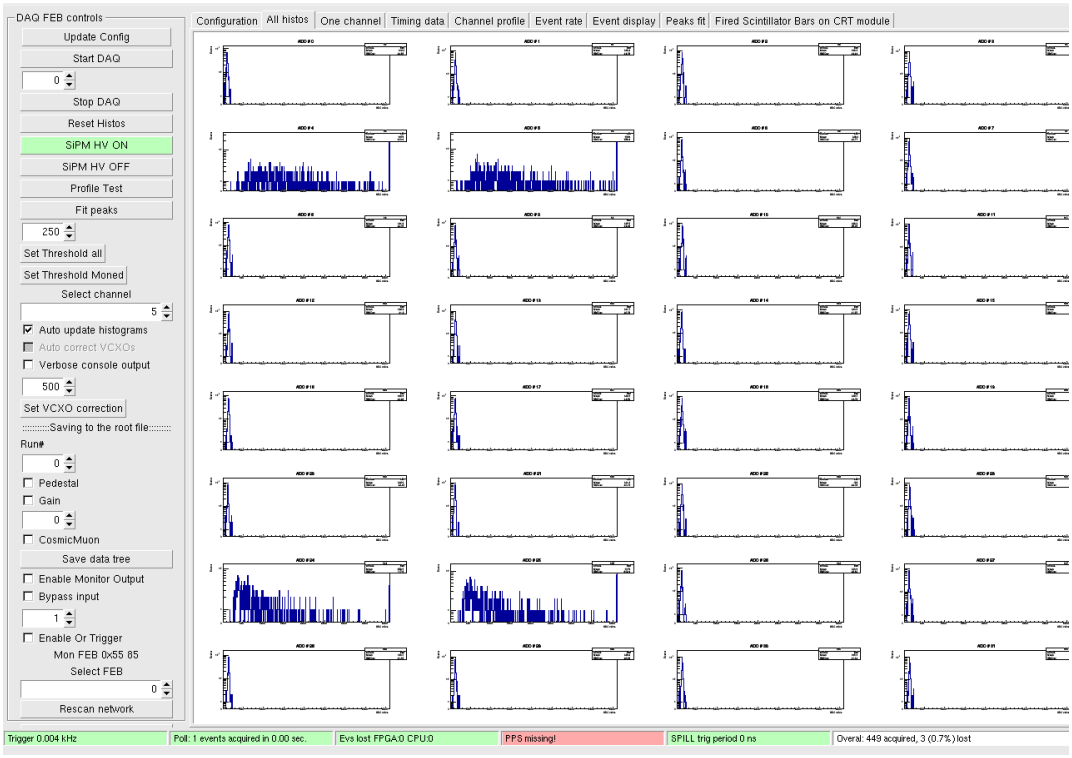

Figure 3.25: Screenshot of a channel monitoring where the trigger is the AND of channels 4-5-24-25 only.

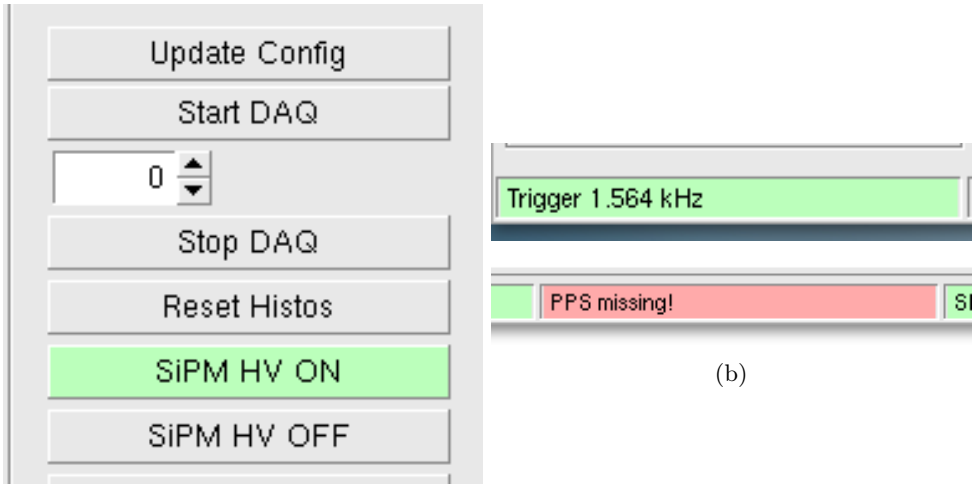

(a) (b)

Figure 3.26: GUI details of (*a*) buttons for switching on/off the SiPM High Voltage (green if HV turned on) and start/stop the standalone DAQ. (*b*) CRT trigger rate (top) and presence of PPS signal in T0 (bottom), in this case no PPS is sent to the FEB.

	CRT Barcode	CRT Assembly date [YYYY-MM-DD]	FEB Barcode	Barcode of Scintillator	Barcode of SiPMs		FEB Channel numbers		Electronics Functionality	Pedestal Scan	Calibration Scan	Cosmic Muon	Efficiency	Name	DB Update	Citiroc Config
1	CRT00001	2019-03-21	FEB00001	10216Scin	15827	15830	0	1	YES	NO	NO	NO	94	Laura	Update Modoule	Citiroc SC
				10212Scin	16675	16648	2	3								
				10215Scin	15801	15841	4	5								
				10226Scin	16591	16590	6	7								
				10171Scin	15842	15803	8	9								
				10188Scin	15813	15857	10	11								
				10164Scin	16572	16568	12	13								
				10165Scin	16584	16583	14	15								
				11270Scin	13840	13815	16	17								
				11272Scin	14053	14052	18	19								
				11256Scin	14121	14136	20	21								
				11264Scin	13834	13833	22	23								
				11271Scin	13801	13805	24	25								
				11275Scin	14064	14058	26	27								
				11101Scin	13747	13742	29	29								
				11117Scin	13767	13766	30	31								

Figure 3.27: Screenshot of the dedicated database containing all the information of the CRT modules and its CITIROC file configuration.

to monitor the event rate and the presence of a PPS signal in T0. These details are shown in Figure 3.26.
At the end of a data acquisition via GUI it is possibile to store the acquired data in a root file. The data tree contains one entry per event and it provides information on the FEB number (*mac5*), integrated charge for each of the 32 channels (*chg*), time stamps (*T0* and *T1*), the triggered channels (*coincidence*) and special event flags.

3.5.5 Multifeb DAQ

The multifeb DAQ is an application that allows to controll, configure and receive data from a chain of connected FEB via ZeroMQ sockets. Differently from the standalone DAQ, the multifeb does not have an interactive GUI. The multifeb DAQ allows to manually download a different CITIROC file for each connected FEB in daisy chain. Changes in the DAQ parameters as such as trigger configurations, SiPMs thresholds, gain or bias have to be manually done by modifying the CITIROC configuration file.
Once a CRT module is completed and its informations are stored in the database, as reported in Figure 3.27, a CITIROC configuration file containing all the correct SiPM parameters is automatically produced and it can be downloaded into the FEB to test the module functionality.
At the beginning of the data acquisition, a feature of the multifeb DAQ is the possibility to change the data polling period. Each data polling contains a variable number of FEB events where the maximum number of event of the poll is a product of the number of connected FEB by the board buffer capacity (2014 events). Each event has the same structure of those acquired by the standalone DAQ application. The acquired data consist of variable-size messages, each of them corresponding to one data poll period. The data structure inside each poll period is described in Figure 3.28.
Once the acquisition is stopped, the multifeb DAQ can store the data in a binary file containing a data tree, a macro is then used to convert it into a root file.

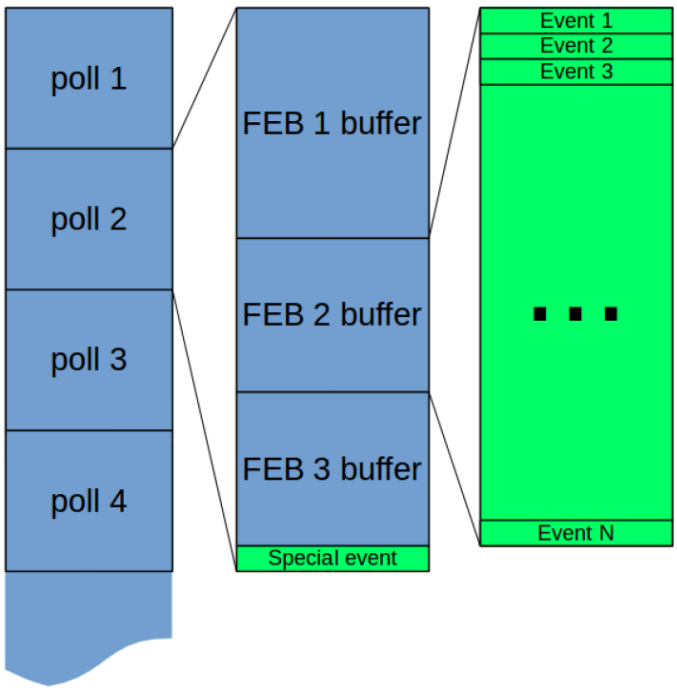

Figure 3.28: Structure of the data flow during active poll loop.

Chapter 4

Cosmic Ray Tagger measurements

The module evaluation techniques were first developed on the prototype at the Bologna laboratories and then applied to the assembled modules at LNF. The evaluation methods summarized in this chapter are referred to the light yield measurements of the prototype and one of the assembled modules. A timing resolution measurement was additionally performed on the prototype.
A brief description of the functionality tests performed during the module assembly is provided.

4.1 CRT Module 0

The CRT engineering prototype, or Module 0, was built at the INFN Bologna facilities in 2018, with the purpose to define the last choices for the production as well as to test the construction procedures. As an example, the list of different gluing techniques are shown in Table 4.1.

15 mm scintillators:	**Technique:**	**10 mm scintillators:**	**Technique:**
1	Bluesil glue + EJ glue	9	not glued SiPM
2	Bluesil glue + EJ glue	10	Bluesil glue+ EJ glue
3	Bluesil glue	11	Bluesil glue+ EJ glue
4	Bluesil glue	12	Bluesil glue+ EJ glue
5	Bluesil glue	13	Bluesil glue+ EJ glue
6	Bluesil glue + EJ glue	14	not glued SiPM
7	EJ glue	15	EJ glue
8	EJ glue	16	EJ glue

Table 4.1: List of the different glue composition used for the bars of the Module 0. Bluesil is a two component silicon based glue, EJ is an epoxy based hard glue. The combination of Bluesil and EJ glue is obtained by gluing the SiPM with the soft glue, while using the hard one for the WLS fibre.

4.1.1 Light yield measurement

Using the geometry of the hodoscope, where the scintillator of one plane crosses all the scintillators of the other plane, it is easy to arrange appropriate coincidence triggers, to collect cosmic muons crossing each scintillator in a square 22×22 cm^2. Data were collected for each scintillator slab, using the standard FEB and biasing the SiPM at 58.15 V. The light yield measurements are performed by analysing the charge integrated spectrum in each channel of the FEB in a 150 ns window. The light yield (LY) of a single channel is obtained with the equation:

$$LY(p.e.) = \frac{MPV - Ped}{G} \ , \tag{4.1}$$

where MPV corresponds to the most probable value of the charge distribution of the tested channel, Ped is the pedestal value of the channel and G is its gain. The MPV for each SiPM was obtained by fitting the corresponding channel integrated charge spectrum with a Landau convoluted with a gaussian function.
The convoluted gaussian and Landau fits for a channel of the 10 mm scintillators and one of the 15 mm scintillators are presented in Figure 4.1 (a) and (b) respectively.
The pedestal value of each channel is obtained by fitting with a gaussian the charge distribution of the channels not interested by the coincidence, as shown in Figure 4.2 for one channel. The gain was obtained as the average distance between the quantized photoelectron peaks in the integrated charge spectrum of cosmic muons obtained by triggering a single coincidence at the time. The quantized photoelectrons peaks were fitted by using multiple gaussian functions, the gain was obtained by averaging the distance between two subsequent peaks. Multiple gaussians fits of photoelectron peaks of a cosmic muon run for a channel of the 10 mm scintillators and one of the 15 mm scintillators are presented in Figure 4.3 (a) and (b) respectively. The distributions are the same of Figure 4.1, but only the first part of the spectrum is highlighted.

The result of the light yield measurements on the Bologna CRT Module 0 are summarized in Table 4.2. The light yield plots of the Module 0 measurement are shown in Figure 4.4 (a) and (b).
The charge integrated spectrum of channels 0 and 21 did not allow to distinguish the photoelectron peaks, hence it was not possibile to measure their gain.
The average light yield measured on the 15 mm scintillators is 24 photoelectrons, while the average value measured in the 10 mm ones is 10 photoelectrons.

4.1.2 Timing measurements

During the data analysis of the SBN experiment, it will be crucial to associate each cosmic muon tagged by the CRT system with the relative interaction in the TPC, this operation will be only possibile with a timing resolution of ∼ns. By measuring the timing difference between the events observed by the PMTs in the LArTPC and the external CRT trigger with a ∼ns resolution, it will be possible to determine if the particle was originated on the outside (cosmic background) or from a interaction inside the TPC.
A cosmic muon that crosses the CRT module and triggers a coincidence, produces a signal in two different scintillator bars. The FEB generates a trigger with a delay depending on the position of the cosmic muon event along the scintillator bar. In order to measure the time resolution of the FEB coincidence generation, different timing measurements have been

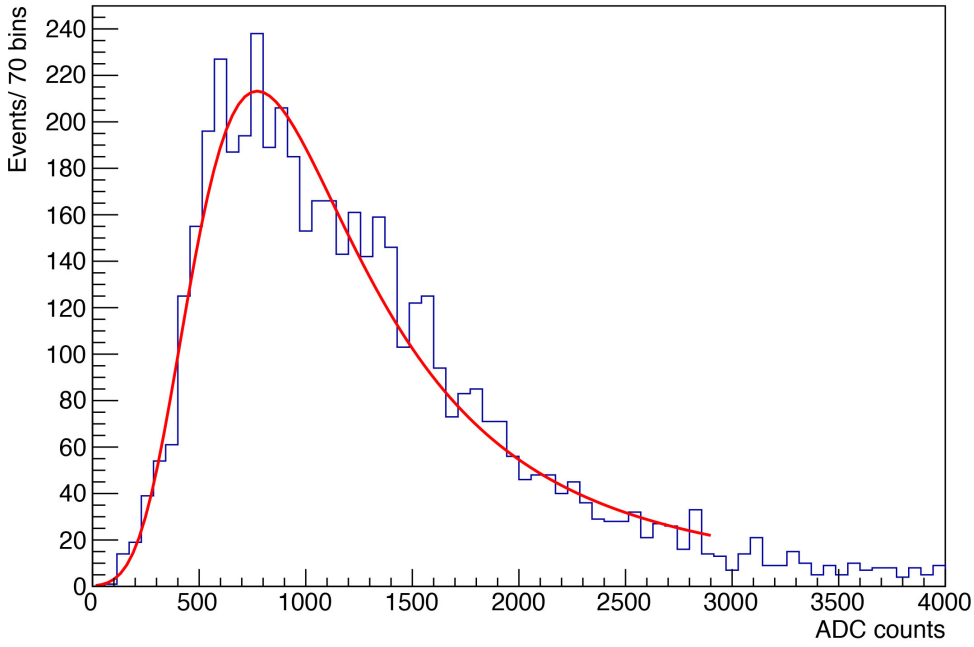

(a)

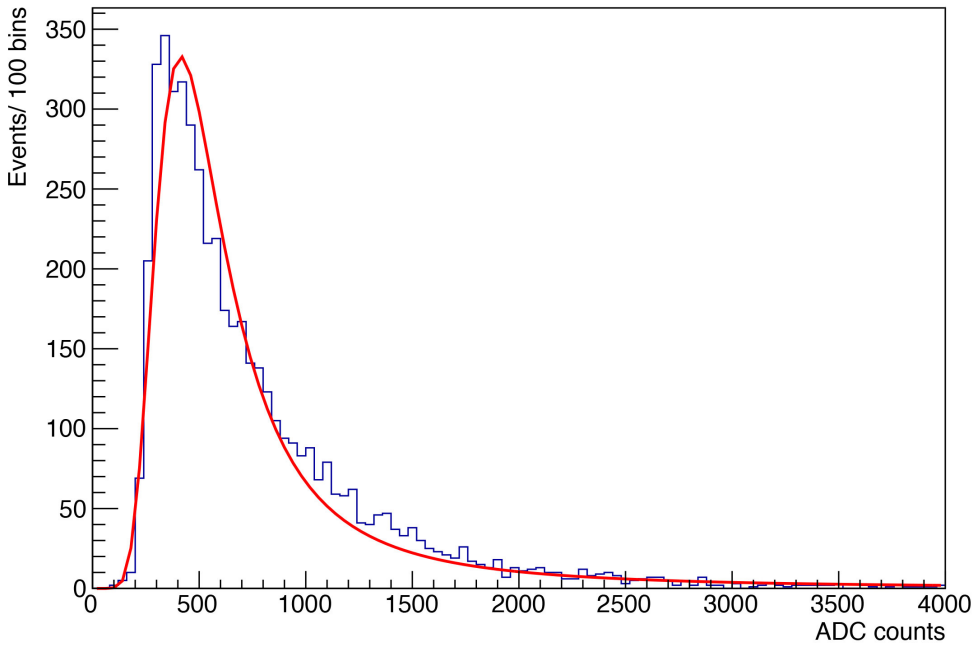

(b)

Figure 4.1: Charge distribution for a channel of a 15 mm scintillator bar (a) and a channel of a 10 mm one (b) fitted with a gaussian convoluted with a Landau. The corresponding MPV are 919 and 459 ADC counts respectively.

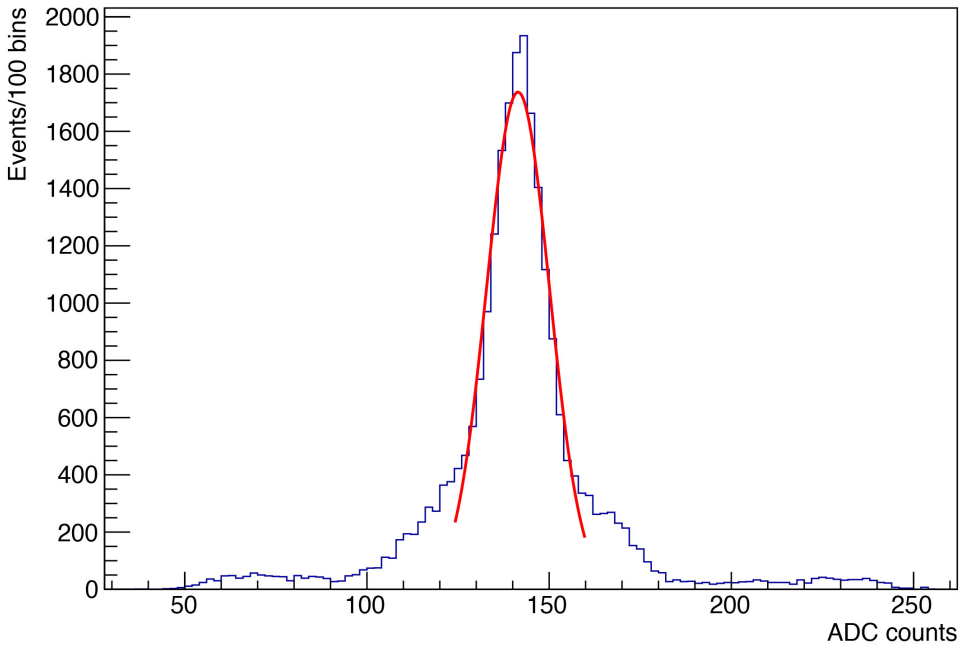

Figure 4.2: Pedestal distribution of one channel fitted with a gaussian function. The mean value of the fit is taken as pedestal value.

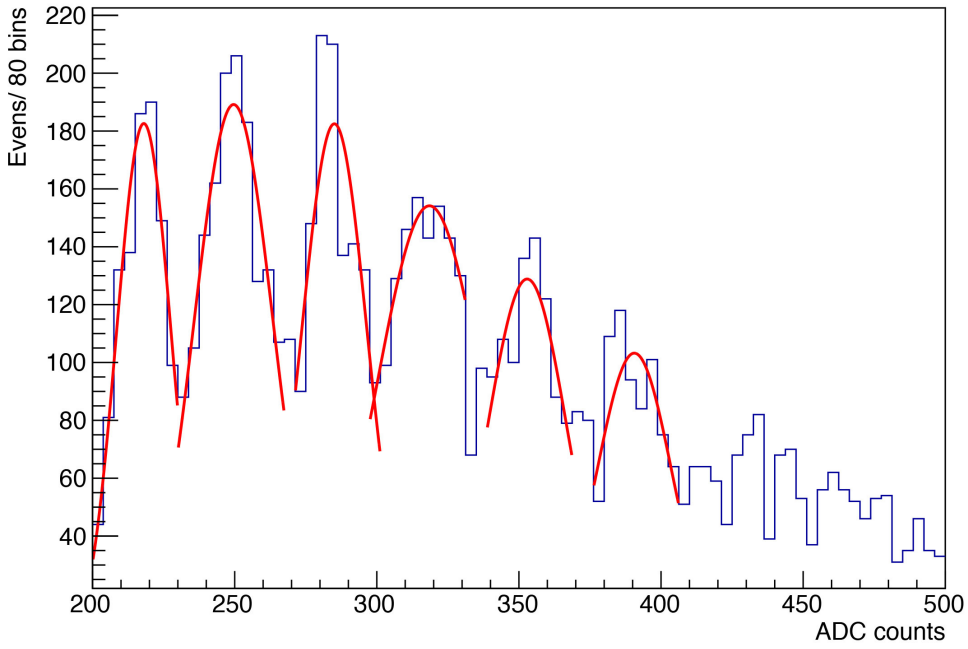

(a)

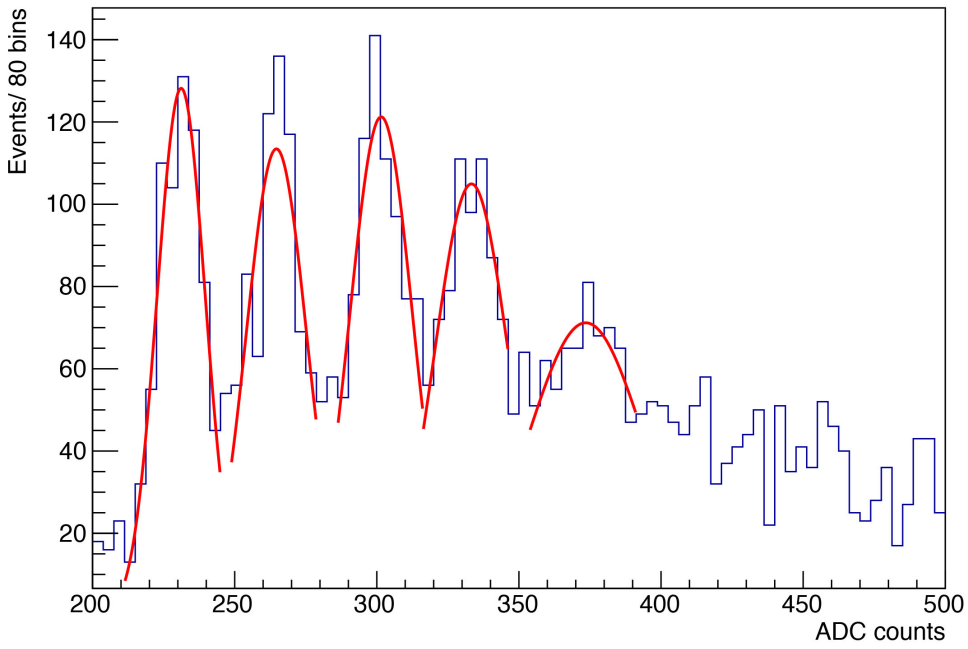

(b)

Figure 4.3: Charge distribution in a channel of a 15 mm scintillator bar (a) and a channel of a 10 mm bar (b). Multiple photoelectron peaks are fitted with gaussian distributions.

Channel	MPV (ADC counts)	Pedestal (ADC counts)	Gain (ADC counts)	LY (p.e.)
0	1518	115	NA	NA
1	919	122	35	23
2	804	126	30	23
3	878	126	32	24
4	930	137	34	23
5	857	119	34	22
6	1213	117	39	28
7	961	119	33	26
8	731	134	30	20
9	857	115	32	23
10	1157	130	39	26
11	943	114	33	25
12	981	136	34	25
13	856	121	34	22
14	1081	115	35	28
15	791	116	31	22
16	463	128	30	11
17	459	115	32	11
18	484	120	32	11
19	511	124	31	12
20	450	114	30	11
21	693	120	NA	NA
22	398	121	32	9
23	425	126	33	9
24	478	109	30	12
25	483	120	33	11
26	375	107	32	8
27	392	112	40	7
28	426	129	32	9
29	425	112	33	9
30	428	124	38	8
31	443	123	33	10

Table 4.2: Summary of the light yield measurement obtained on the CRT Module 0 in the Bologna Laboratories.

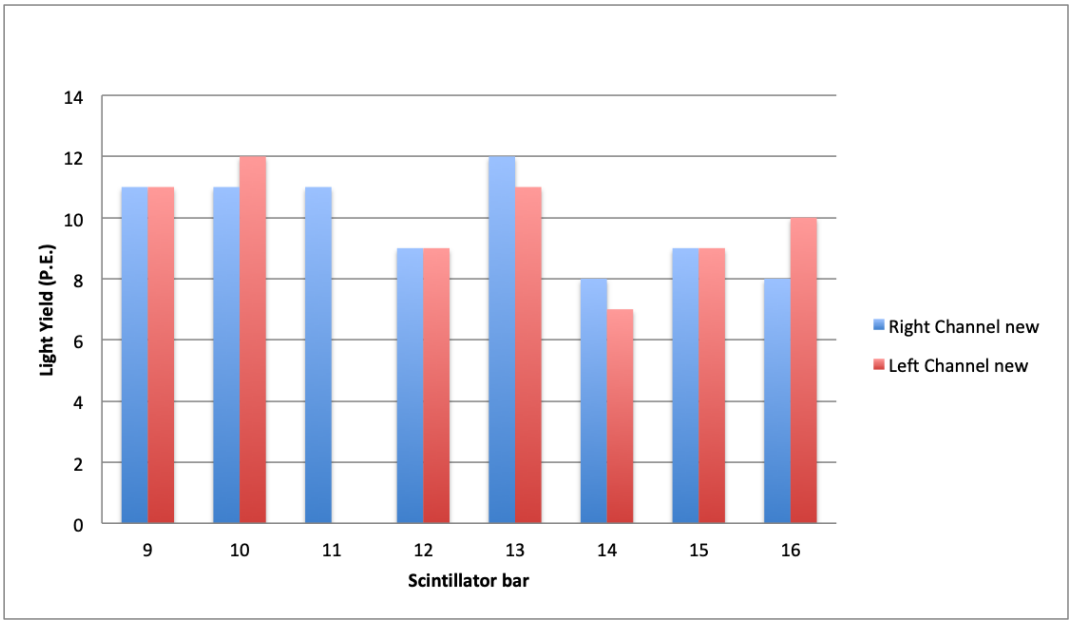

(a)

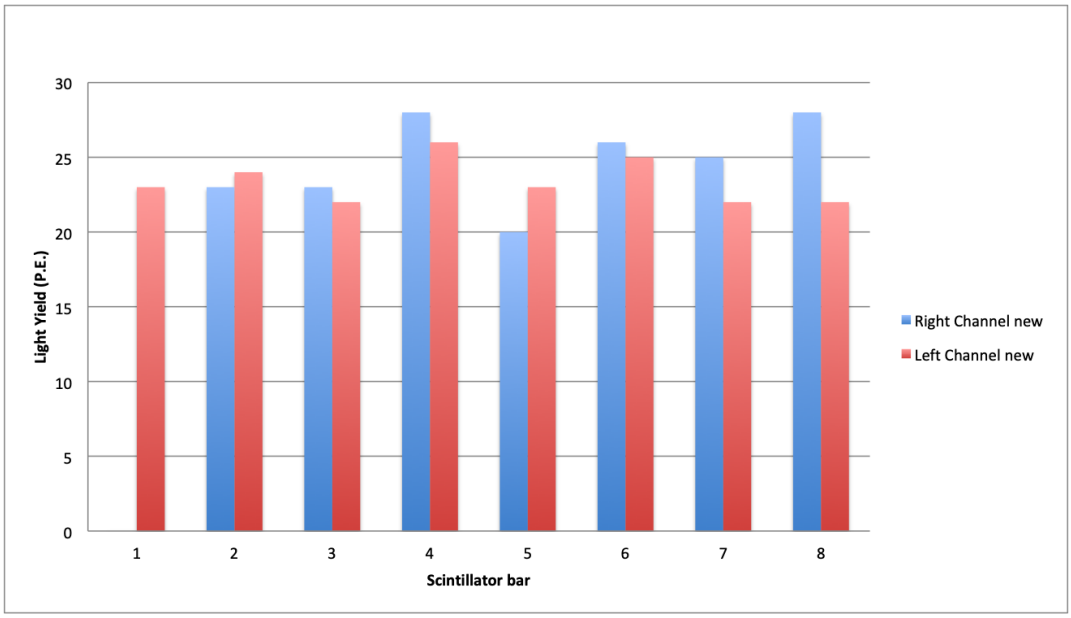

(b)

Figure 4.4: Module 0 light yield measurements in (*a*) 10 mm scintillators and (*b*) 15 mm scintillators.

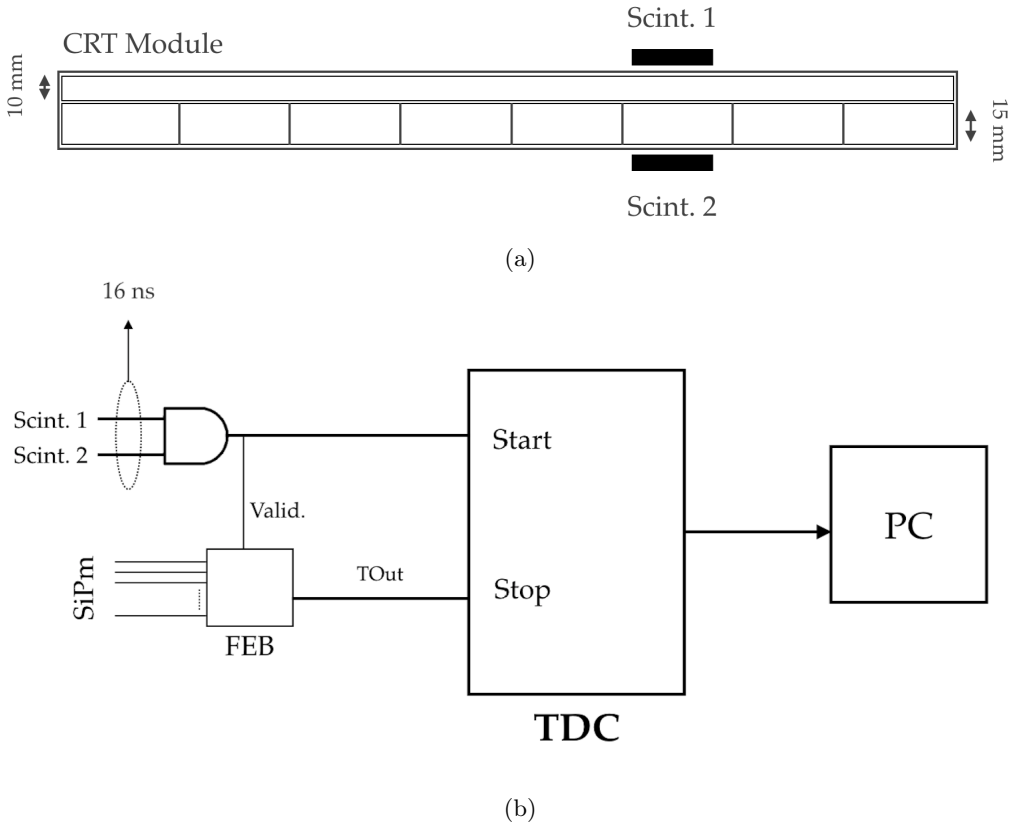

Figure 4.5: Illustration of (*a*) the measurement setup and of the (*b*) measurement logic circuit.

taken across the prototype module.
In order to perform time measurements of the trigger coincidence formation, two external scintillators were used to provide an external trigger. The two scintillators were connected to one PMT each. The outputs of the PMTs were then discriminated with a NIM module with a threshold set to 40 mV. The AND logic of the discriminated signals was used as the logic trigger. The coincidence was then sent to the trigger input of the CAEN V1290 VME TDC. The discriminated signal of the top scintillator was used as the *Start* of the TDC. The coincidence of the two PMTs was sent to the TIN of FEB and its TOUT was used as the *Stop* of the TDC module.
With this setup, the TDC measures the delay between the external trigger signal and the formation of the trigger within the FEB. The data from the TDC were acquired using a dedicated VME DAQ readout software. The illustration of the setup used to perform the time measurements on the CRT Module 0 is shown in Figure 4.5.
In total ten measurements were performed along the CRT module, corresponding to ten different sectors of the module. In Figure 4.6 a mapping of the time measurement positions across the module its presented.
Due to the low rate of cosmic rays on the 23 $\times$ 23 cm^2 regions of the module ($\sim$8 Hz), the

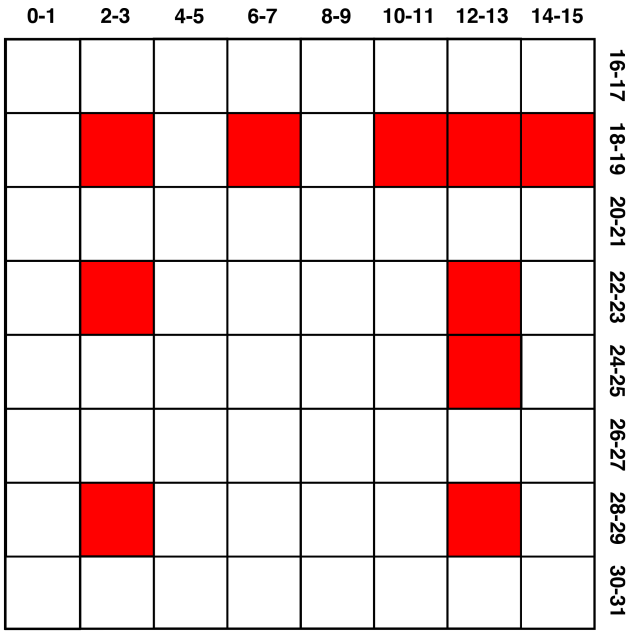

Figure 4.6: Timing measurement mapping positions of the prototype module.

data acquisitions were performed during night time and during the weekends. Two examples of resulting timing measurement distributions for different sectors are presented in Figure 4.7. The first plot corresponds to a data sample of a whole weekend (∼12000 events), while the second one corresponds to a night long acquisition (∼4000 events).

The timing distributions obtained for every coincidence window tested were fitted with gaussians to obtain the most probable value. The MPV of the timing distribution measured along different position of the bar with channels 18-19 (10 mm scintillator) are plotted in Figure 4.8 (a), those for the channels 12-13 (15 mm scintillator bar) are plotted in Figure 4.8 (b).

The analysis of the MPV distribution along the scintillator are in accordance with the hypothesis that a cosmic event that triggers far away from the SiPMs, produces a slow coincidence, with respect to a cosmic event close to SiPMs.

A conservative prediction on the FEB coincidence timing resolution can be made by averaging the different standard deviations in each timing measurement. The conservative result is $\bar{\sigma} = 2$ ns. More precise measurements can be obtained with different setups and they will be the subject of future studies.

4.2 CRT modules at the Frascati National Laboratories

The CRT modules are currently under construction at the INFN LNF. The module construction began on March 2019 and it is expected to be completed by the end of the year.

Currently three main activities are performed at LNF: scintillator gluing station, aluminum boxes construction and modules assembly and testing. Some pictures of the different activi-

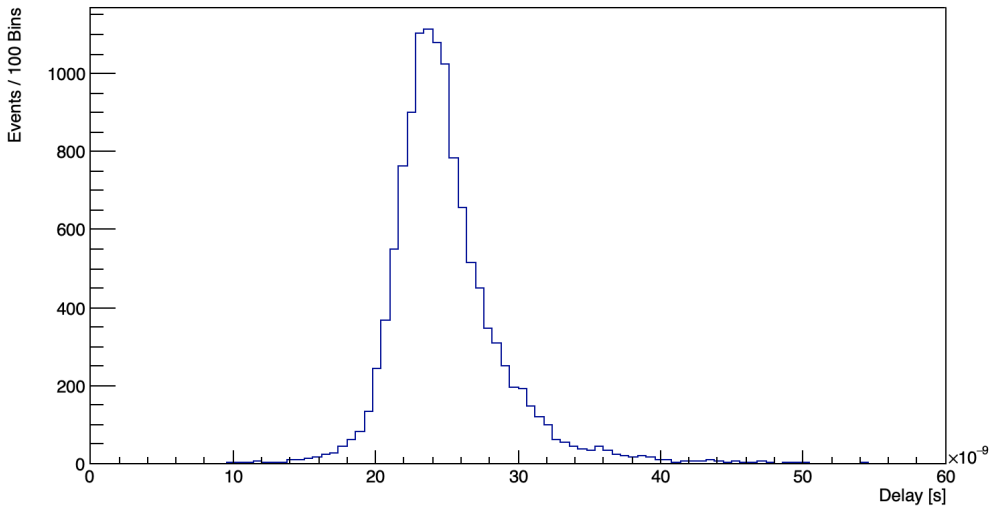

(a)

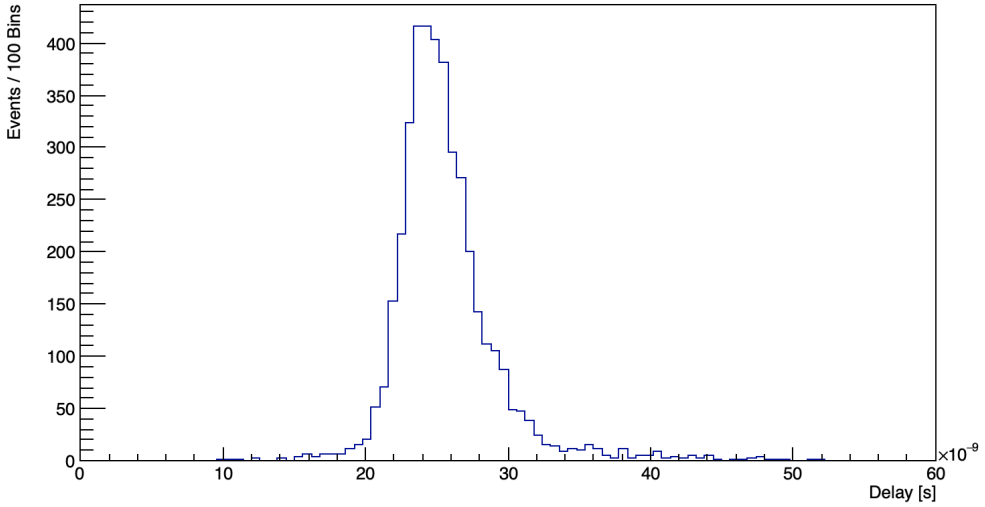

(b)

Figure 4.7: Timing distribution measured for (a) the 2-3-18-19 channels coincidence and for (b) the 12-13-28-29 channels coincidence.

ties are presented in Figure 4.9.
Based on the experience developed with the FEB electronic on the Module 0, I actively participated in the modules assembly and testing at LNF. The module assembly procedure was described in section 3.1.

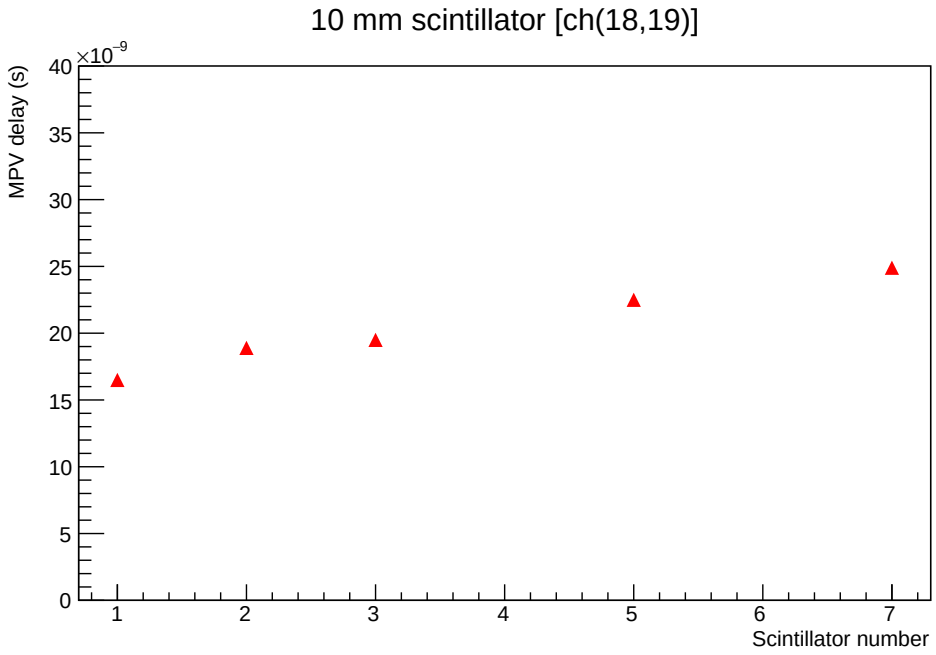

(a)

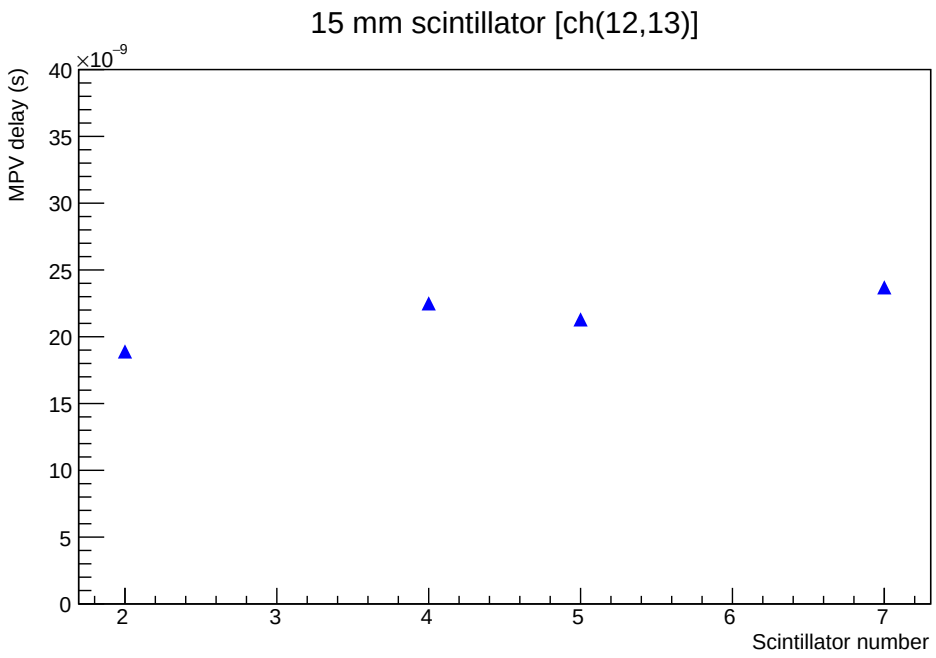

(b)

Figure 4.8: Time for the formation of a coincidence along a scintillator bar in case (a) of the 10 mm layer and (b) the 15 mm layer.

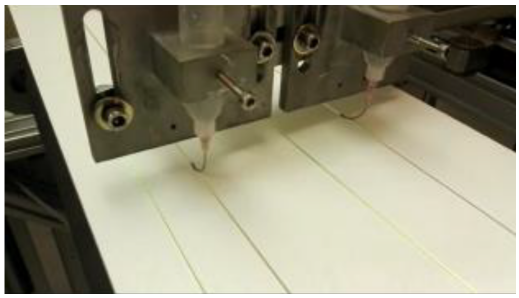

(a) Gluing station

(b) Boxes construction

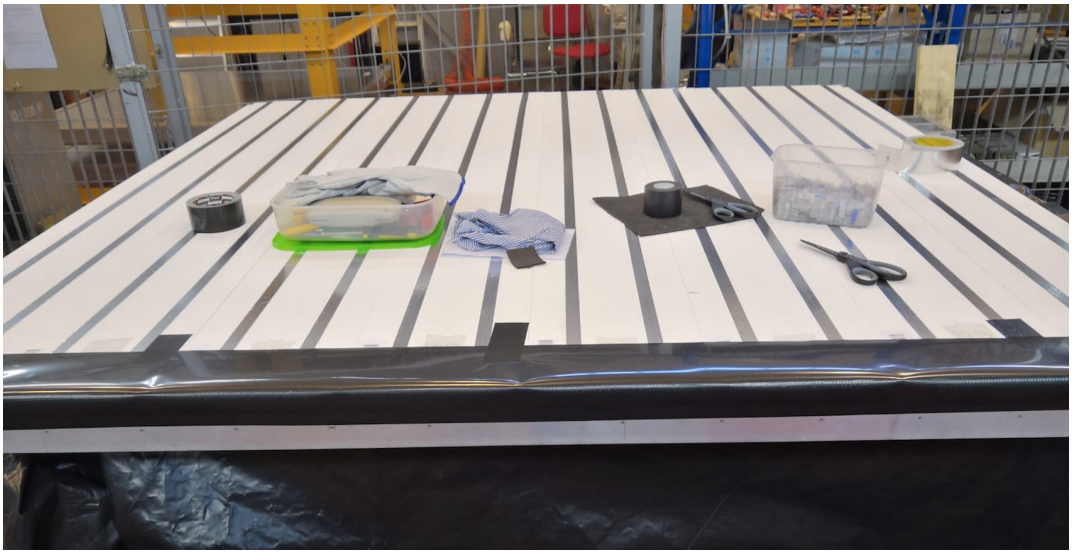

(c) Assembly station

Figure 4.9: Pictures of different working stations at LNF.

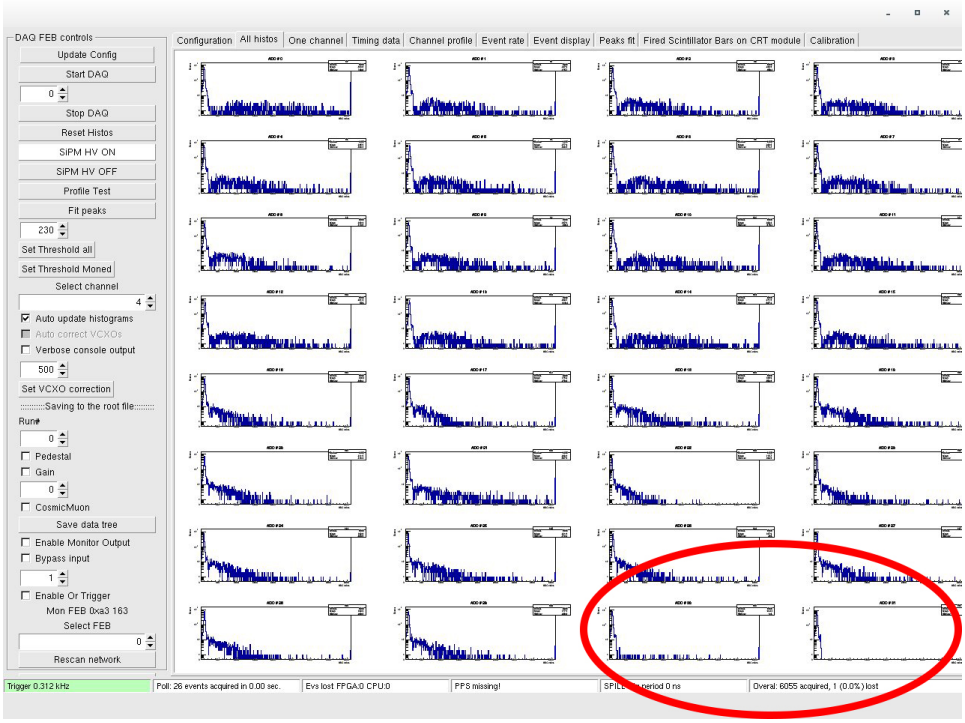

Figure 4.10: Screenshot of the channel monitor with an example of broken channel.

4.2.1 CRT functionality tests

During the assembly of each module, several functionality tests have to be performed before definitively closing and approving the modules.
The first test is the Electronic Functionality Test and it is performed once the top layer of the module is covered with the black foam-like plastic sheet. Using the Standalone DAQ and providing the High Voltage to all the SiPMs it is possibile to verify the correct functionalities of all 32 photodetectors. In case of problematics, several evaluation steps are performed to identify the problem and find a solution. An example of an encountered problematic is shown in Figure 4.10, the electronic functionality test highlighted a problematic in the channel 31, in this particular case the corresponding channel on the FEB was broken, the problem was solved by using a different board.
A second test is performed once the top of the aluminum box is laid on the two scintillator layers, by using the Standalone DAQ and monitoring the event rate across the module while illuminating corners and other sensitive points with a torch. If no light leakage are present the rate of the module is stable at $\sim$550 Hz, which is expected from the cosmic rays. If the rate increases while moving a torch along the module, there is a possible light leakage that has to be fixed with black tape.
Once the module is tested and closed, it is moved the Test Stand where further measurements

Figure 4.11: Picture of the Test Stand in the CRT assembly hall.

are performed. A picture of the Test Stand filled with three of the eight available slots is shown in Figure 4.11.
Once the Test Stand is full, using the Multifeb DAQ it is possible to download in each module the corresponding CITIROC file configuration. Once this is done the modules are ready for the efficiency measurements which will be discussed int the next chapter.
While in the Test Stand, by downloading the correct CITIROC file using the Standalone DAQ, special Pedestal Scans can be run. The Pedestal Scans are performed by enabling triggering on all the channels in OR logic mode. The resulting root file is then processed with a macro that fits every channel integrated charge distribution and extracts each pedestal mean value in a text file.

4.2.2 CRT modules light yield measurements

Light yield measurements as described in section 4.1.1 are time consuming and due to the tight schedule, it is not possibile to interrupt the assembly line and perform the same measurement for every module in the Test Stand. The light yield calibration of each module will then be performed at Fermilab once all the module will be completed.
Although it isn't possible to calibrate each module due to time costraints, it can be done for a limited sample and once the same calibration will be performed in Fermilab, it will be

possibile to estimate the effects of the shipment on the scintillator bars performances.
Based on my previous light yield measurements on the Module 0, I performed the same calibration on the CRT module number 46. The only difference between the new measurement and the previous one, is that this time the gain was evaluated from a linear fit of the quantized photoelectron peak positions and the pedestal was obtained from the Pedestal Scan described in the previous section. With respect to the Bologna prototype, the 15 mm layer and the 10 mm layer will be connected to the opposite channels of the FEB, hence channels 0-15 are referring to the 10 mm thick bars and channels 16-31 are referring to the 15 mm ones.
The measurements were performed on a night long cosmic muon run. Distribution of integrated charge are shown in Figure 4.12 from 300 to 1000 ADC counts and in Figure 4.13 in the entire range for 10 mm scintillator bars (a) and the 15 mm thick one (b). In the former the consecutive photoelectron peaks are fitted with gaussian distributions. From the latter the MPV of the fit of a Landau convoluted with a gaussian os obtained. 10 mm scintillators are characterized by an expected lower light yield and the most probable value is collocated at $\sim$5 photoelectrons peak. 15 mm scintillators, on the other hand, are characterized by an higher light yield of $\sim$20 p.e., hence the most probable value is way over the first photoelectron peaks.

The light yield measurements of the CRT module number 46 are summarized in Table 4.3, which shows the mean number of photoelectrons for each channel. The light yield plot for the two scintillator layers are presented in Figure 4.14. The average light yield value for the 10 mm scintillators is 6 photoelectrons and it is 20 photoelectrons for the 15 mm ones.
Analogous measurements will be done on other CRT modules in the upcoming months.

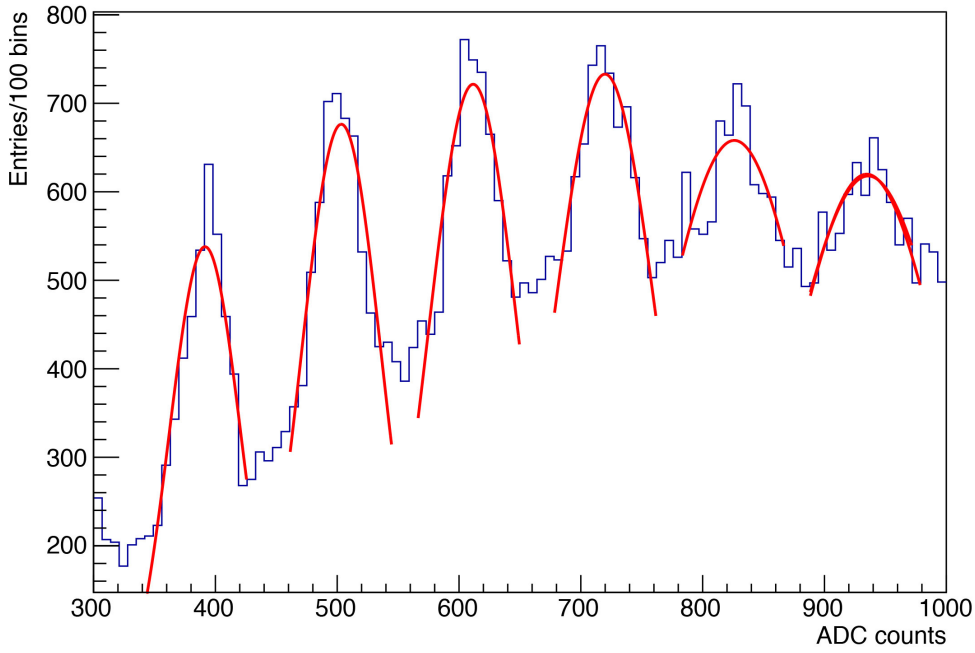

(a) 10 mm scintillator channel

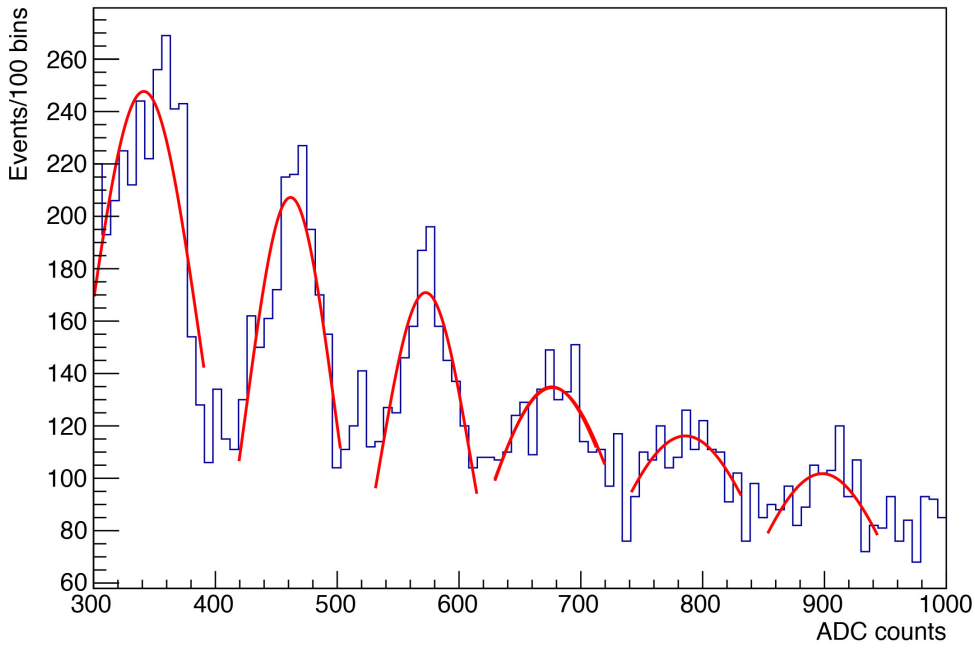

(b) 15 mm scintillator channel

Figure 4.12: Plot of the multiple photoelectron peaks fitted by gaussians in (*a*) a channel of a 10 mm scintillator bar and (*b*) a channel of a 15 mm one.

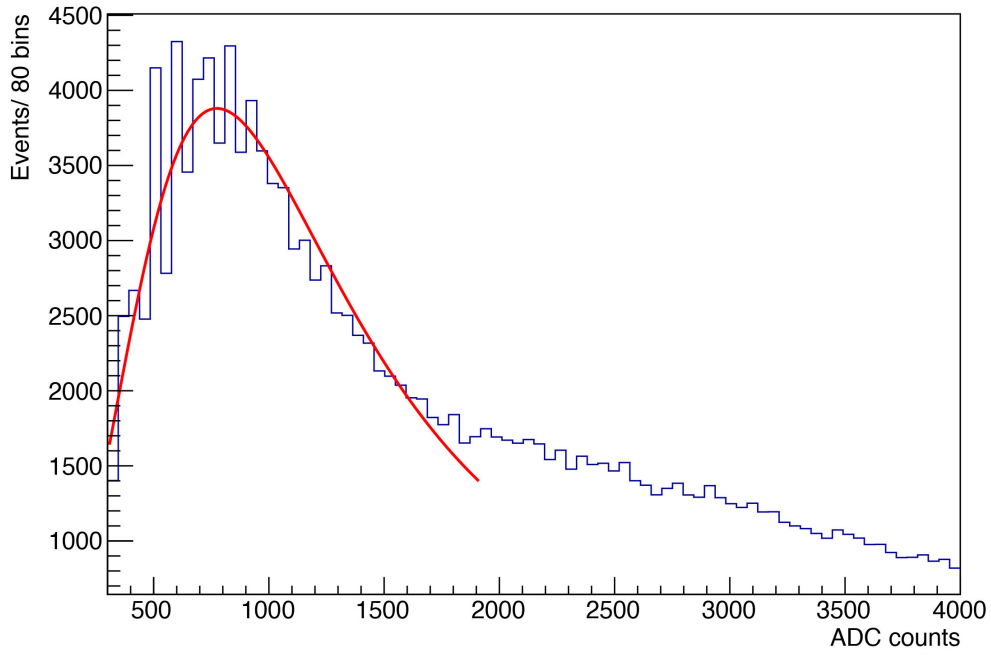

(a) 10 mm scintillator channel

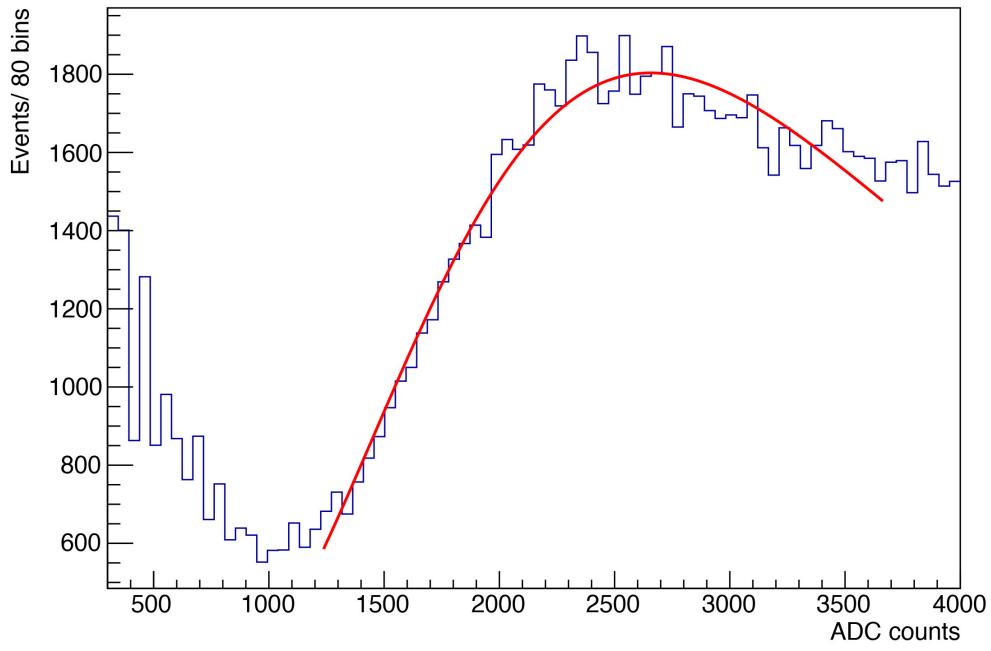

(b) 15 mm scintillator channel

Figure 4.13: Charge distribution for a channel of a 10 mm scintillator bar (a) and a channel of a 15 mm one (b) fitted with the convolution of a gaussian and a Landau. The corresponding MPV are 872 and 2735 ADC counts respectively.

Channel	MPV (ADC counts)	Pedestal (ADC counts)	Gain (ADC counts)	LY (p.e.)
0	892	166	106	7
1	907	180	109	7
2	797	187	107	6
3	722	164	107	5
4	794	175	106	6
5	965	177	105	8
6	885	174	104	7
7	944	170	105	7
8	864	148	106	7
9	769	158	103	6
10	906	168	105	7
11	896	143	104	7
12	865	181	101	7
13	803	163	102	6
14	684	169	103	5
15	621	174	102	4
16	1998	206	100	18
17	2060	158	103	19
18	2613	158	106	23
19	2652	175	108	23
20	2158	152	107	19
21	2118	175	103	19
22	2022	156	109	17
23	1987	179	104	17
24	2499	169	102	23
25	2537	178	106	22
26	1995	184	110	16
27	2043	163	112	17
28	2120	177	108	18
29	2410	167	114	20
30	2786	145	114	20
31	2735	156	109	24

Table 4.3: Summary of the light yield measurement obtained from the CRT module 46.

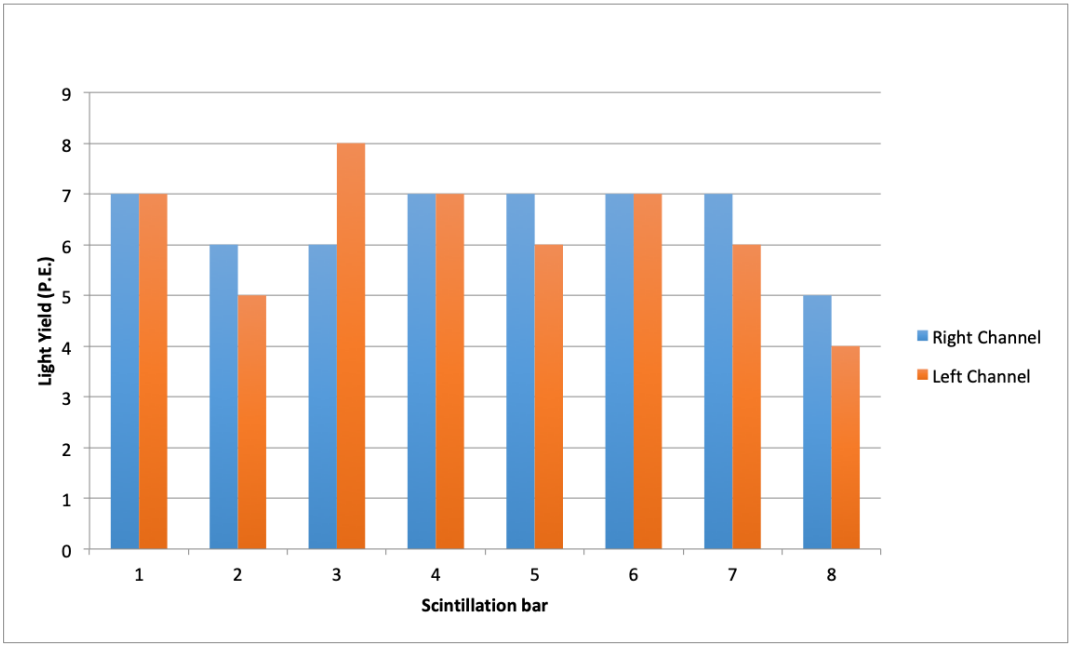

(a)

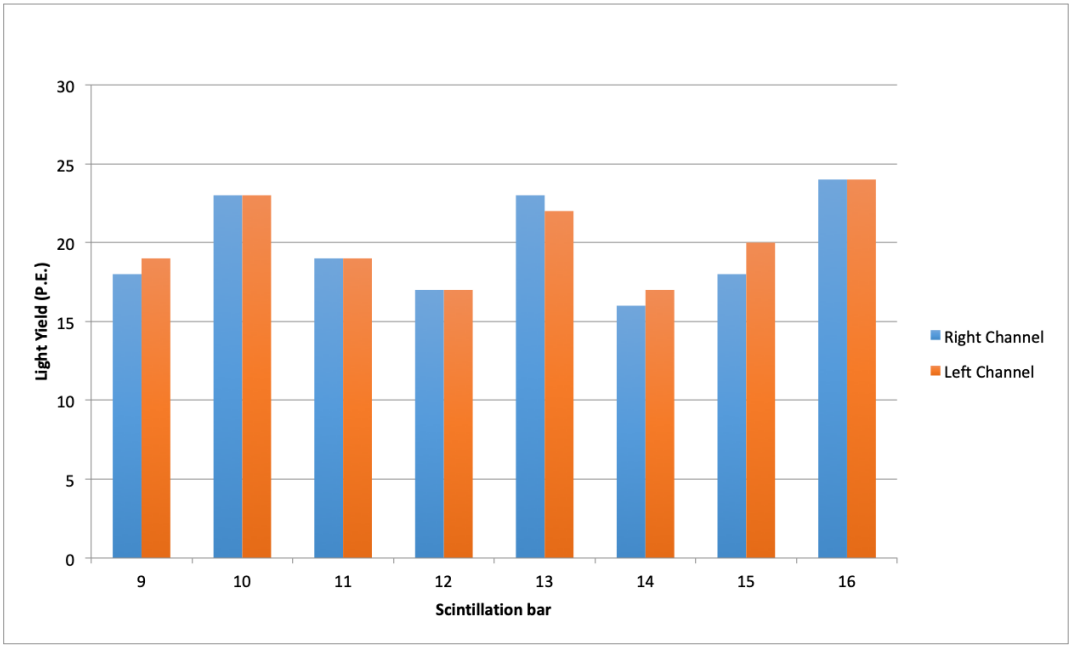

(b)

Figure 4.14: CRT module number 46 light yield measurements in (a) 10 mm scintillators and (b) 15 mm scintillators.

Chapter 5

Efficiency measurements

One of the most important features of the Top CRT system will be its high tagging efficiency. As previously said, an expected rate of $\sim$ 25 kHz of cosmic rays will reach the ICARUS TPC from the detector roof. An high cosmic ray tagging efficiency will be crucial for a correct and precise analysis of the tracks reconstructed in the LAr-TPC.
In order to map different regions of the module, preliminary efficiency measurements based on an independent external trigger were performed on the CRT Module 0 in Bologna. Due to the long acquisition time needed to characterise the efficiency of all the coincidence regions within the module, a faster measurement technique was developed based on an external trigger provided by the coincidence of multiple FEBs. The technique was first tested in Bologna by using pairs of orthogonal scintillators placed on the top and on the bottom of the prototype and connected to two FEBs. The same measurement was replicated at the production site in Frascati by using the assembled modules. The new technique allows an average efficiency measurement of the whole module in a single acquisition run.
Thanks to more precise measurements, efficiency inhomogeneities in the scintillator bars were observed along the direction perpendicular with respect to the fibres.
An additional technique was studied in order to perform efficiency measurements of each of the coincidence regions of multiple modules at the same time. This technique is based on an offline reconstruction of the events in multiple modules by comparing the data stream of different FEBs. During the development of the technique some problems caused by the FEB firmware were observed and reported to the manufacturer.

5.1 Preliminary Module 0 measurements

A preliminary efficiency measurement was performed on the CRT Module 0 in Bologna by analysing the same data-set acquired during the timing measurement described in section 4.1.2. The measurement setup is sketched in Figure 4.5.
The external trigger consisted of two scintillators placed on an aluminum support and coupled to two PMTs. The aluminum support was moveable, but due to its limited extension, it was not possible to test with the same setup inner positions of the prototype. Using the *standalone DAQ*, only the SiPM channels of the CRT module corresponding to a particular coincidence region were supplied with the high voltage. For each measurement the external trigger was placed in the center of the scintillators coincidence tested. The mapping of the

15 mm Scin. Channels	10 mm Scin. Channels	Efficiency (%)
14-15	18-19	97.8
12-13	18-19	98.6
10-11	18-19	98.5
6-7	18-19	98.0
2-3	18-19	98.0
12-13	22-23	80.4
2-3	22-23	81.9
12-13	24-25	98.0
12-13	28-29	97.9
2-3	28-29	95.0

Table 5.1: Summary of the efficiencies measured for some of the scintillator coincidences of the Module 0.

measurements is reported in Figure 4.6.
The efficiency was evaluated as the ratio of the events acquired by the *standalone DAQ* to the triggered events in the TDC DAQ after a minimum of seven hours of data acquisition. The efficiency values for the tested coincidences are reported in Table 5.1.
Due to the current FEB electronic, it is not possible to test single fibres of the scintillator bars because the FPGA-provided trigger requires the logic AND of both the scintillator channels. The efficiencies of the tested bars are all above 95%, except the one corresponding to channels 22-23 which has an efficiency of ∼81%. A possibile explanation of the lower value will be described in the following section.

5.2 Test Stand efficiency measurement

In order to map the efficiency of the whole module with the setup described in the previous section, multiple measurements and long data-acquisition runs have to be to performed. This measurement technique cannot be replicated at the Test Stand in Frascati, in fact the long exposure times needed would significatively delay the production line. In order to perform a faster efficiency measurement suitable for the available setup at the production site, a new technique that allowed to obtain an average efficiency across the whole module was developed on the Bologna prototype.
The efficiency measurement at the Test Stand is performed using the setup sketched in Figure 5.1. By having multiple modules on top of each other and enabling all the coincidence regions, an external trigger can be obtained as the logic AND of the TOUT signals of the top and the bottom modules FEBs. The new external trigger is then sent to the TIN LEMO connector of the tested modules and to a channel of a scaler, in order to count the *external coincidences*. A logic AND of the external trigger and the tested module TOUT signal is obtained and sent to another channel of the scaler to provide the *double coincidence* counts. The overall efficiency of the module is calculated as the ratio of the *double coincidence* to the *external coincidence* counts.
This technique was first tested in the Bologna laboratories, but, since the only module available was the Module 0 itself, two pairs of scintillator bars of the same type required for

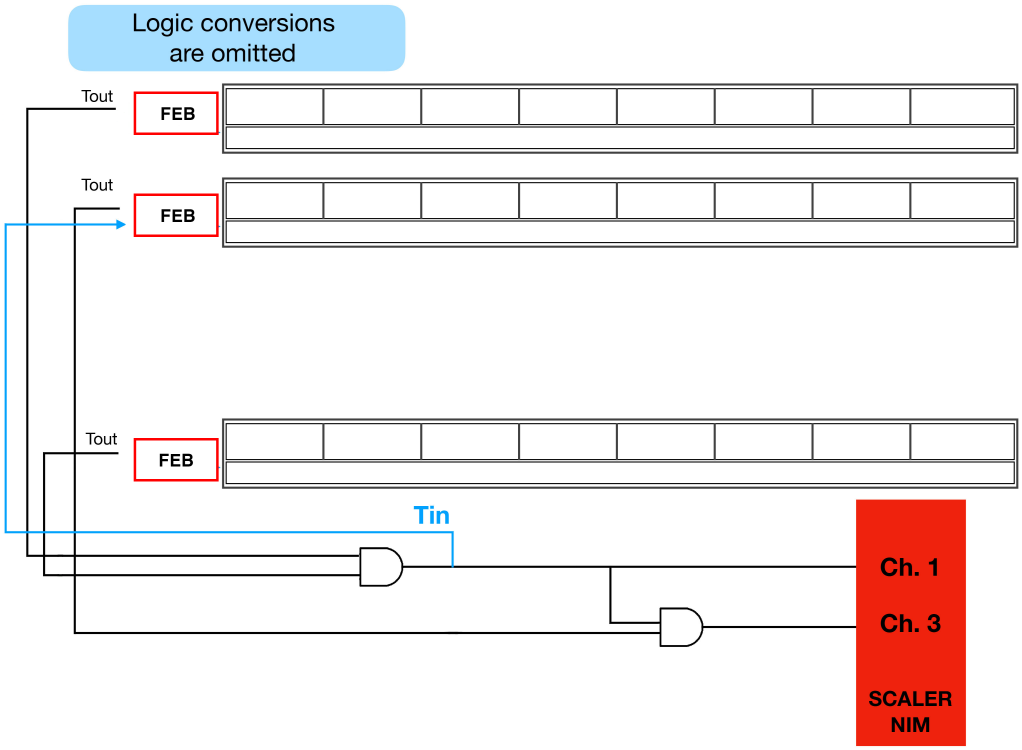

Figure 5.1: Illustration of the setup used in the efficiency measurement performed at the Test Stand in Frascati.

the assembly of the CRT modules were used as trigger. The four bars have been covered with black paper and black tape in order to ensure the light tightness. In each pair the scintillator bars (10 mm and 15 mm thick) were placed orthogonally one to the other in order to reproduce the geometrical coincidences of the CRT modules. A pair of scintillators was placed on the top of the prototype, the other was placed on the floor and parallel to the top one at a distance of ∼1.20 m.
Since this measurement was merely a test of the procedure to be performed in LNF, only the coincidence corresponding to channels 2-3-28-29 was tested. This coincidence was chosen in order to compare the result with the corresponding efficiency of 95% previously calculated during the preliminary measurements.
Each pair of scintillators were connected to a FEB each by using the same micro-coaxial cables used for the modules assembled in Frascati in correspondence to the same channels enabled in the Module 0. The three FEBs were connected in daisy chain via ethernet cables and the data acquisition was performed by using the *multifeb DAQ*. The measurement setup is illustrated in Figure 5.2. In accordance to the other setup shown in Figure 5.1, the efficiency was calculated as the ratio of the *double coincidence* to the *external coincidence* counts. Due to the distance between the external coincidences (∼1.20 m), only very straight cosmic muons were selected and the observed rate was of few events per minute. In order to

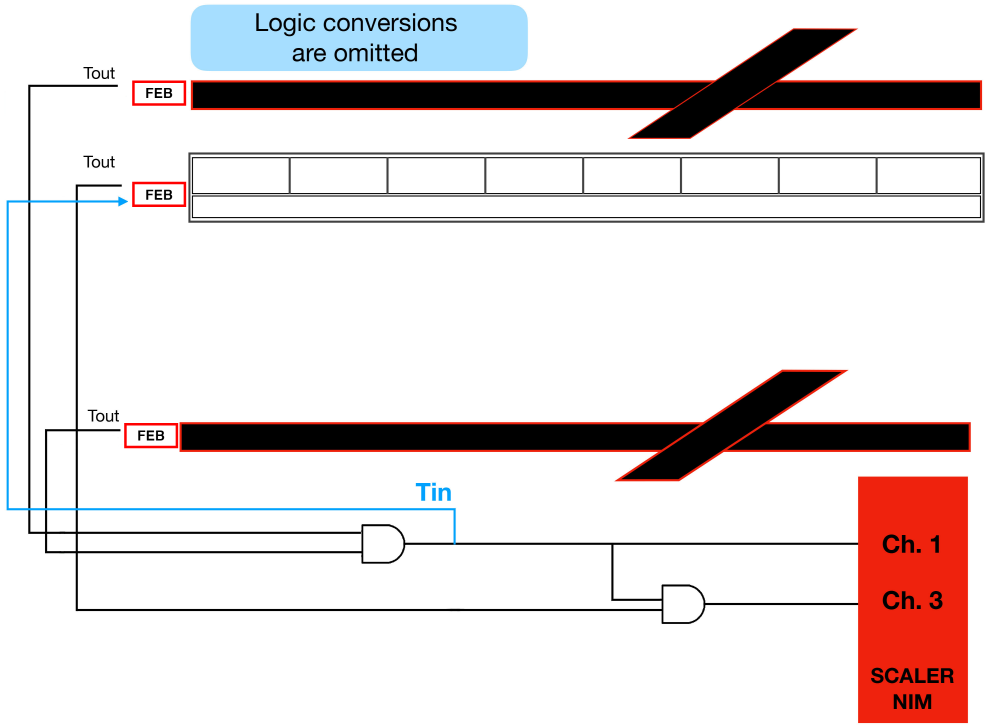

Figure 5.2: Illustration of the setup used in the efficiency measurement performed with the scaler on the CRT Module 0.

acquire enough statistics long data acquisition runs were needed.
In a first measurement a threshold of 0.5 p.e. was set for both the external trigger and the prototype module and the HV of the SiPMs corresponding to the channels 2-3-28-29 only was enabled. A night long data acquisition run was performed and a low efficiency of 57.9% was measured. The low efficiency was imputed to the fact that the external FEBs and the attached micro-coaxial cables were not shielded from the noise induced from the laboratory instrumentation, while those of the Module 0 were protected by the aluminum casing of the box.
In order to prevent the triggering on the noise, a further test was performed by rising the threshold of the external trigger FEBs to ∼4 photoelectrons and after a night long data taking a 92.3% efficiency was obtained.
The test described in the previous section measured an efficiency of 95.0% on the same coincidence. If we assume a perfect alignment of the three coincidence regions in the latter test, the difference between the two measurements can be imputed to the smaller triggering area of the 13 cm (L)×5 cm (W) scintillators used in the preliminary measurement, with respect to the 23 cm × 23 cm region triggered in the last one.
The trigger used in the preliminary measurement was placed at the center of the tested coincidence, hence only particles with an impact point at the center of the bar with respect to the two fibres are triggered. On the other hand, the trigger obtained with the CRT

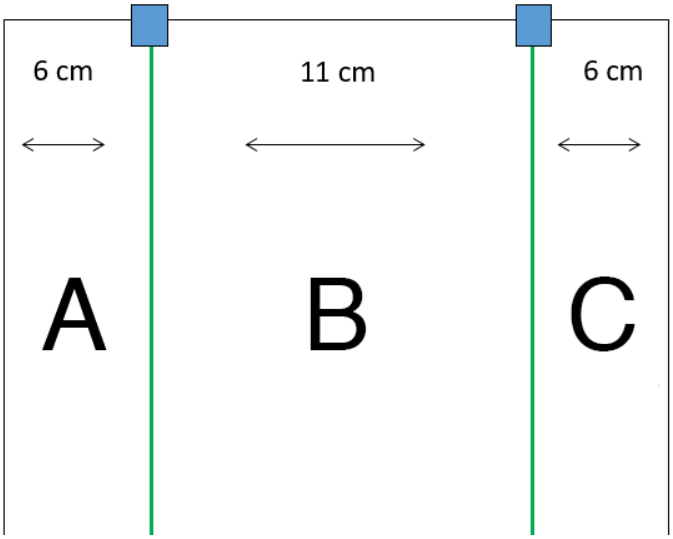

Figure 5.3: Efficiencies regions tested (A, B and C) along the transverse direction of the 10 mm scintillator bar.

scintillator bars allow to select also particles that crossed the edges of the bars, where the amount of light collected among the two fibre is different.
As reported in section 4.2.2, the light yield measured for the 10 mmm thick bars is on average ∼6 p.e., much lower than the 20 p.e. measured in the 15 mm thick ones. Hence in the thinner bars the signal on one fibre could be under threshold in case of events that crossed the edge of the scintillator far from that fibre, so that the event is not triggered. This phenomenon causes efficiency inhomogeneities along the transverse direction of the bars.
An additional test was performed in order to measure the efficiency in different regions of the 10 mm scintillator bar along the transverse direction. This measurement was obtained by using an external trigger made of 3 cm × 3 cm plastic scintillator tiles coupled to PMTs. The PMTs signals were sent to a discriminator with a threshold set to 30 mV and then put in coincidence to trigger the acquisition of a waveform digitizer. The trigger was positioned on three different regions of the bar as sketched in Figure 5.3, in which region B is the one where the trigger of the preliminary measurements was placed. The SiPMs of the 10 mm bar were connected to one FEB together with those of the 15 mm bar as it was done for the previous measurement. This setup allowed to trigger the coincidence of channels 2-3-28-29 in the FEB and to acquire the corresponding TOUT signal, which was sent to the digitizer together with the non-discriminated signals of the two PMTs. The sketch of the setup used is shown in Figure 5.4. The efficiency was computed as the ratio of the number of events with a TOUT signal in the digitizer to the number of total triggered events.

The efficiencies measured in the three different regions along the transverse direction of the 10 mm bar are listed in Table 5.2. As expected, regions A and C have lower efficiencies with respect to the inner region B. This difference can be imputed to the fact that in case of particles with an impact point in regions A or C, the light collected by the farther fibre is not enough to produce a signal over the threshold. Due to the current FEB triggering logic

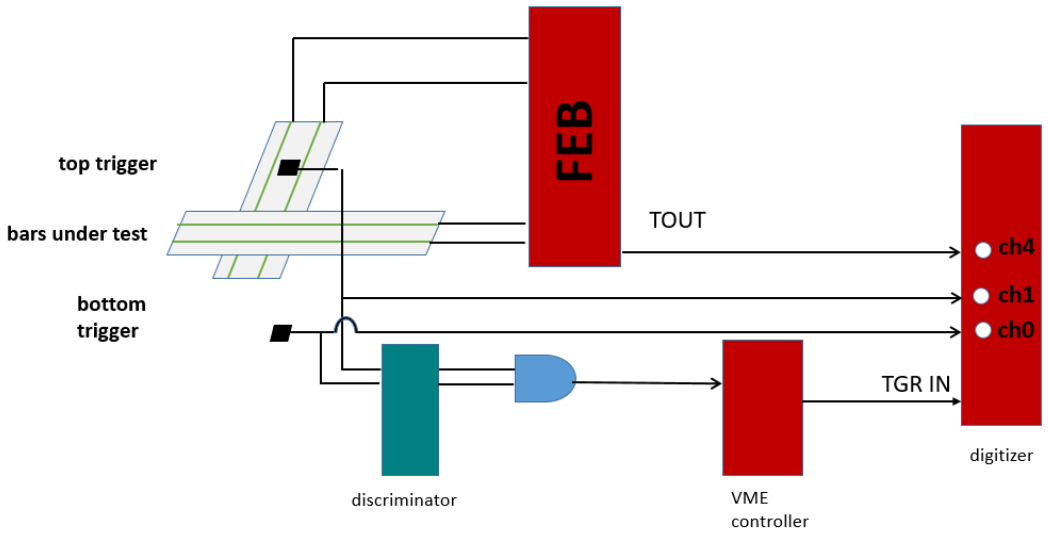

Figure 5.4: Sketch of the setup used to measure the efficiency in different regions of a bar using external 3×3 cm^2 scintillator tiles.

Region A	Region B	Region C
85%	97%	85%

Table 5.2: Results of efficiency measurements in the three tested regions of the 10 mm scintillator bar.

described in section 3.5.2, the logic AND of the two channels would not allow the formation of the trigger.
The efficiency inhomogeneities observed in the 10 mm bar can explain the low ∼81% efficiency measured on the channel 22-23 scintillator by assuming that the external trigger was placed in the A or C region of the bar.
In order to increase the efficiency of the coincidences within the CRT modules, a possible solution can be provided by implementing in the triggering logic the OR of the two fibres of the same scintillator.

The test in Bologna was a benchmark for the efficiency tests at the Test Stand in Frascati, where the same measurements were obtained using CRT modules as external triggers, as shown in Figure 5.5. The shielding of the aluminum casing of the modules allowed the FEBs to work in a noise-free environment, hence the fine tuning of the SiPM thresholds was not needed.
The Test Stand has eight slots available, 20 cm apart one from the other, with an overall distance between the top and the bottom slot of ∼170 cm. For continuity between different measurements, the top and the bottom slots are always occupied by the same modules. The top module used for the efficiency measurement is the CRT number 14, which has an efficiency of 98%. The CRT number 3 was used as the bottom one, with an efficiency of 96%. The CRT numbers are referred to the module assembly order.

Figure 5.5: Test Stand with the NIM crate used for the efficiency measurement on the right.

The high rate across the whole $\sim 185 \times 185$ cm^2 module is on average 550 Hz and it allows to obtain an high statistics of ∼300000 events with a data taking of about 10 minutes. By using the setup described in Figure 5.1, due to the limited number of available channels on the scaler, only one module at a time can be tested. The resulting efficiency measurements correspond to the average efficiency of the module.
Currently, 58 out of the 125 modules have been completed and tested. Efficiencies measured per each module are shown in Figure 5.6.

The average CRT modules measured efficiency is 96.0%. The lowest efficiencies are 92.0% and 91.6%, while the best ones are 98% and 97.8%. The statistical error per each efficiency measurement is ∼0.5%.

5.3 Offline event reconstruction

The average efficiency measurement currently performed at the Test Stand in Frascati is a limiting factor for a correct characterization of the efficiencies regions within the modules. A great improvement can be provided by reconstructing all of the cosmic muon events that cross the eight modules in the Test Stand and measuring the tagging efficiency of all the coincidences regions of the modules in a single data acquisition run.
Along with the measurements on the prototype in Bologna and at the Test Stand, I worked on the development of an offline efficiency measurement tool based on the reconstruction of cosmic muon events.
Offline efficiency reconstruction is based on the identification of the same cosmic muon event

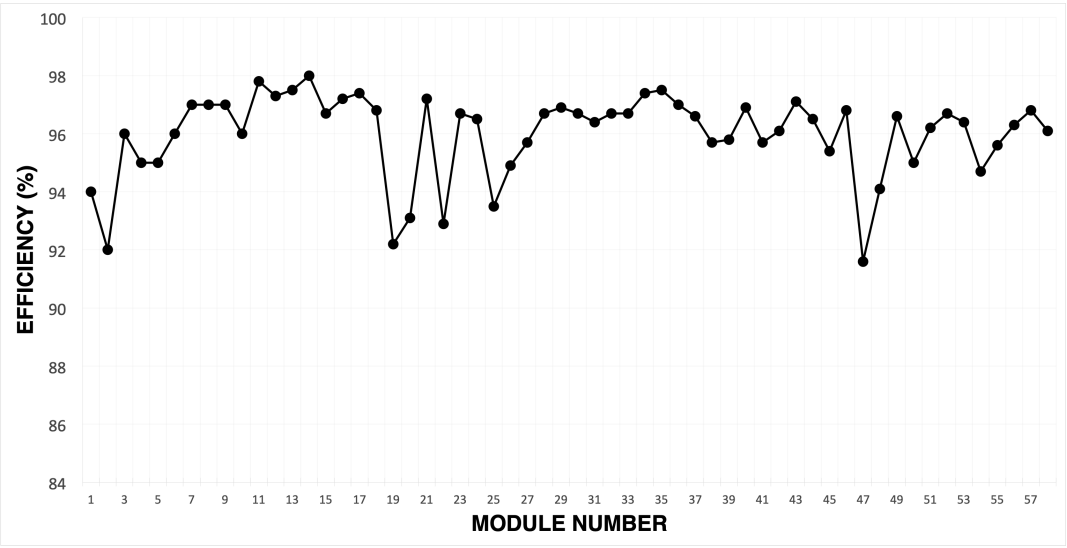

Figure 5.6: Efficiencies measured for each assembled CRT module in LNF.

that crosses multiple modules in a Test Stand-like setup by comparing the timestamps and the trigger informations stored in the output file acquired by the *multifeb DAQ*. The timestamp used for the reconstruction is the one referring to the T0 signal, which is supplied with a PPS signal coming from a GPS. The informations of the triggered channels are extracted from the *coincidence* branch in the output root file.
The efficiency tool was first developed for the analysis of the data taken with the Module 0 and then adapted to the root files acquired in Frascati.
The experimental setup used in Bologna is described in Figure 5.7. If we compare it with the one presented in Figure 5.2, the only difference is the presence of the PPS signal to reset the T0 counter. In this measurement only the coincidence of channels 2-3-28-29 was tested.

The offline efficiency reconstruction is divided in multiple steps. The first step is the comparison of the number of events triggered by the FEBs. Data from the different daisy-chain connected FEBs are sequentially contained in each data poll as described in Figure 3.28. By selecting the specific mac address for each FEB, it is possible to obtain a data-set for each of them. Special reset events are excluded from computation of the efficiency and are used to calculate a global reference time as it will be explained in the following. A preliminary evaluation of the average efficiency of the module can be obtained as the ratio of the number of events acquired by the tested module to the number of events measured by the FEBs that provide the external trigger.
The second step of this analysis is based on the comparison of the event timestamps in the different FEBs data-set. Each timestamp recorded by the FEB corresponds to the time passed since the last reset event, with a resolution of 1 ns. The clock of the FEB is reset every second with the PPS signal. An efficiency measurement, based only on timing informations, was performed by aligning events in the three different FEBs according to global timestamps and selecting those separated by a maximum of 25 ns one from the other (corresponding to a maximum of 50 ns between an event of the top coincidence and one of the bottom one). This selection was very conservative, since it corresponds to the time of flight of the muon

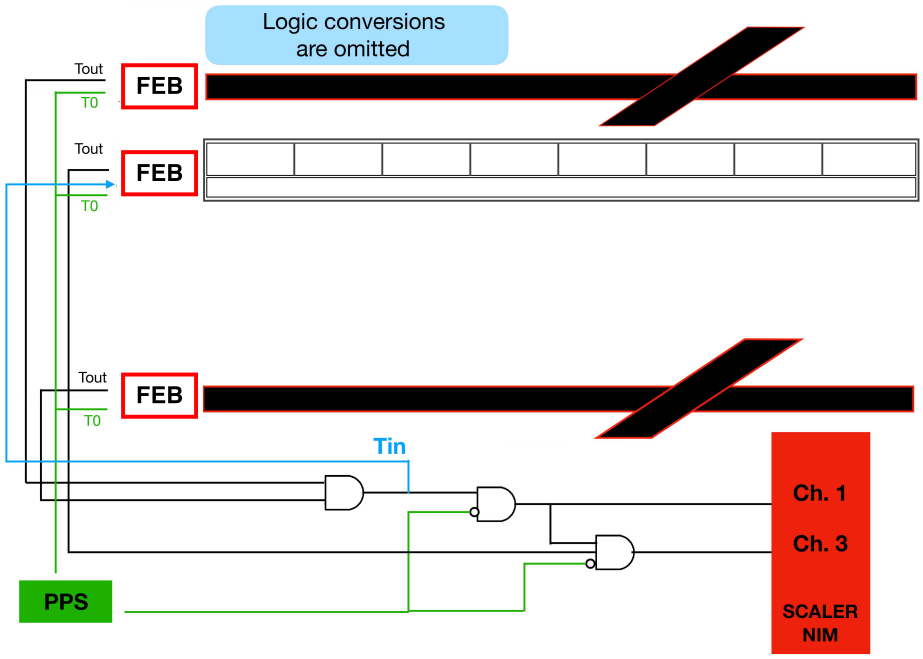

Figure 5.7: Illustration of the setup used for the offline event reconstruction data taking with a scaler based efficiency measurement as quality control.

travelling a 1.2 m distance between the top and the bottom scintillators. Due to this distance, a low rate of few events per minutes was observed with a threshold of 4 photoelectrons, as described in the previous section. Since the FEB does not produce a timestamp of a global timing reference, a counter based on the reset events was used, by doing so the global timing of an event is obtained as:

$$T_{glob}(ns) = ts0 + N \times 10^9 \ , \tag{5.1}$$

where N is the total number of reset signals prior to the selected event.

An example of timestamps used to align the events are listed in Table 5.3. The first and third column are referred to top and bottom trigger FEBs respectively, while the second column is referred to the inner Module 0. Events that are not triggered by the inner module are defined by a null timestamp. The global timestamps used to reconstruct the events are shown in Table 5.4.

Events with the same T_{glob} within 50 ns are looked for in the data stream of the external FEBs, these event are the *external coincidences*. If a non-null event with the same T_{glob} of the external coincidences is found in the FEB data-set of the inner module, this event counts as the *internal coincidence*. The efficiency is evaluated as the ratio of the *internal coincidences* to the *external coincidences*.

In order to have a quality control efficiency measurement on the same data-set reconstructed offline, a Test Stand-like measurement can be performed by introducing the PPS signal and adapting the logic circuit as illustrated in Figure 5.7. The different circuit logic is necessary because every time the FEB acquires a PPS signal, it produces a TOUT which does not

Timestamp top trigger [ns]	Timestamp inner module [ns]	Timestamp bottom trigger [ns]
484433299	484433318	484433307
676975495	676975499	676975503
144767579	144767575	144767578
609760355	0	609760363
144900843	0	144900847
354277295	354277287	354277291
355466331	355466323	355466315

Table 5.3: Table with the timestamps for each FEB aligned using the reconstruction tool developed.

Timestamp top trigger [ns]	Timestamp inner module [ns]	Timestamp bottom bottom [ns]
1484433299	1484433318	1484433307
3676975495	3676975499	3676975503
11144767579	11144767575	11144767578
12609760355	0	12609760363
13144900843	0	13144900847
13354277295	13354277287	13354277291
15355466331	15355466323	15355466315

Table 5.4: Table with the global timestamps for each FEB aligned using the reconstruction tool developed. The events are the same presented in Table 5.3 and they correspond to the an analysis window of 15 seconds.

represent a triggered event and it will be misidentified as a coincidence between the three FEBS. A possible solution to the problem can be provided by introducing additional logic ANDs with the negated PPS signal. The PPS signal is an active high logic state 100 ms long and the scaler efficiency measurement will be vetoed for this period of time, on the other hand, the FEB electronic is sensitive only to the rising edge of the GPS signal and it will not stop acquiring data during this time.
In the final step of the offline efficiency measurement, the reconstruction is performed by looking at the geometrical informations. Perfectly straight events are reconstructed if in the inner module the triggered coincidence is the same of the external trigger modules. This last step of efficiency measurement based on both timing and topological information will be implemented in a Test Stand like measurement, as it will provide events on multiple coincidence regions, rather than a single one as in the Bologna setup.

The test of the algorithm was performed on the Module 0 and the enabled coincidence region was again the one corresponding to the channels 2-3-28-29, characterized by a previously measured efficiency of 92.5%. The data acquisition was taken during a whole night and it measured an efficiency of 92.5%. The preliminary evaluation measured a consistent efficiency of 92.8%, but the implementation of a more precise reconstruction based on the timing and topological informations failed.
By counting the number of PPS signals sent to the FEB and comparing it with the number of reset events flagged by the board, I observed that the two values were different. After further investigations, this problem was associated with some errors in the firmware of the FEB, which randomly prevents to correctly flag the reset events. Several FEBs were tested and it was observed that the percentage of wrong assignment of the reset event flag ranged

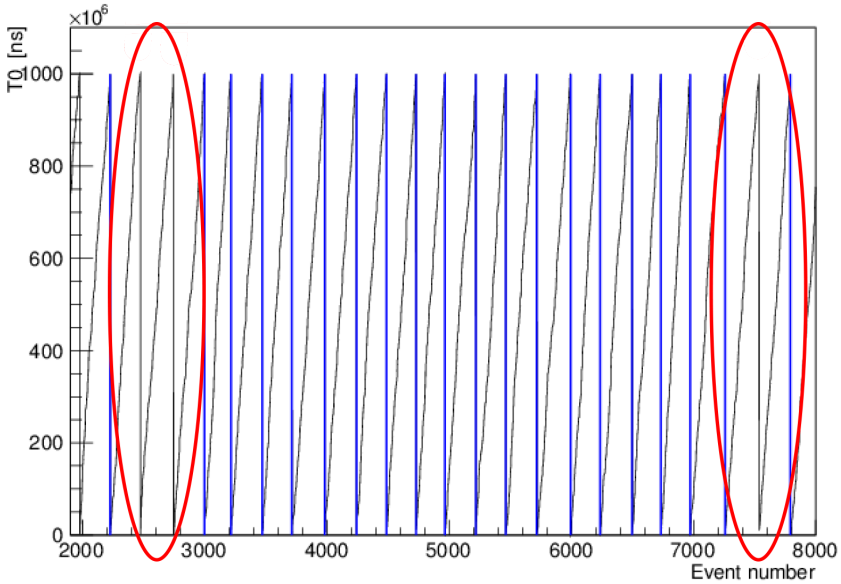

(a)

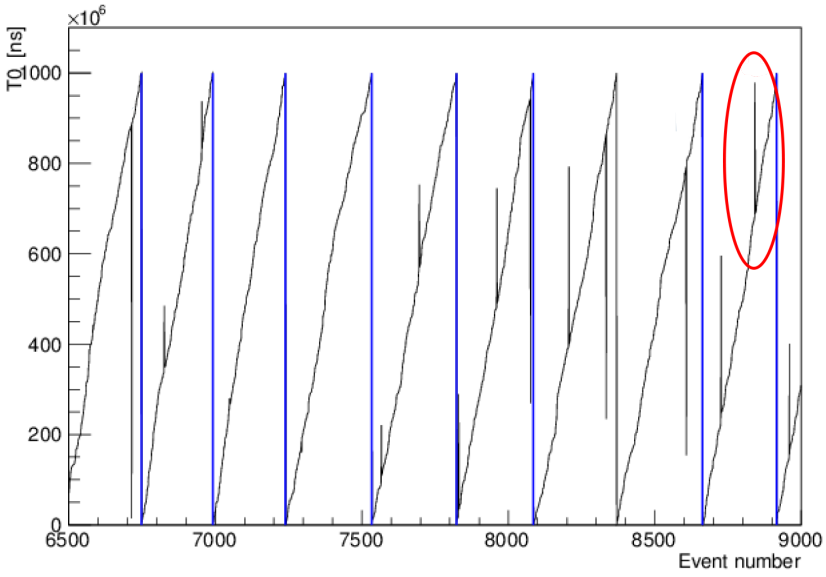

(b)

Figure 5.8: Timestamps vs the event number. Blue lines indicate the correctly identified reset events with highlighted in red (a) the miss-identified reset events and (b) the spikes that can be mistaken for reset events.

between 4% and 13% depending on the board. Out of 9 FEBs tested, only one provided a perfect identification of the reset events. A solution to this problem was implemented by automatically identifying the reset events as events with a timestamp equal to 1 s with 30 ns resolution.
By analysing the timestamp spectrum of the fully enabled Module 0, a new error was observed. As it can be seen in Figure 5.8b, random upward or downward spikes were observed in the timestamp distribution. The spike presence caused misalignments in the offline event reconstruction. This error was investigated and the origin of the problem was again imputed to the firmware of the FEB.
These firmware related errors were reported to the manufacturer and a firmware upgrade is expected in the immediate future.
Once the new firmware will be released, the offline reconstruction of the events will allow the characterization of all the 64 triggered coincidences of the Test Stand modules with a single data acquisition run.

Conclusions

The construction and the measurements of the performances of the engineering prototype of the CRT (Module 0) built in Bologna, besides validating the mechanical design, the components and the procedures for the mass production, have shown that the CRT meets and exceeds the requirement for the SBN experiment.
It is shown that the light output for each of the two fibres of the 16 scintillators in the module has an average light yield > 10 (24) photoelectron for the 10 (15) mm scintillators, with a low spread.
Such a light output will ensure a high system efficiency for detecting cosmic rays, with the residual inefficiency originating from the geometry, like gaps among the modules and frame material.
It is also shown that the timing resolution of the system is $\sigma \leq 2$ ns at any point of the hodoscope, comfortably within the SBN requirements.
The experience gained with the Module 0 has greatly informed the set up of the production line at the LNF, where modules are currently being built, tested and prepared for being shipped to Fermilab.
The construction is foreseen to complete at the end of 2019, with the installation on SBN starting in Spring 2020.
In particular, the availability of many modules allows a very precise measurement of the module efficiency for cosmic rays, by stacking them in a telescope and using the most external ones as a trigger. As expected from the prototype results, we have measured efficiencies on average $\geq 96\%$ which might still be slightly improved by a modification of the FEB firmware currently underway.

Bibliography

[1] J. J. Thomson, "Xl. cathode rays," *The London, Edinburgh, and Dublin Philosophical Magazine and Journal of Science*, vol. 44, pp. 293–316, Oct 1897.

[2] E. Rutherford, "LIV. Collision of α particles with light atoms. IV. An anomalous effect in nitrogen," *The London, Edinburgh, and Dublin Philosophical Magazine and Journal of Science*, vol. 37, no. 222, pp. 581–587, 1919.

[3] L. Metiner and O. Hahn, "Über die verteilung der beta-strahlen auf die einzelnen produkte des aktiven niederschlags des thoriums," *Phys Z.*, vol. 13, p. 390, 1912.

[4] J. Chadwick, "The intensity distribution in the magnetic spectrum of beta particles from radium (B + C)," *Verh. Phys. Gesell.*, vol. 16, pp. 383–391, 1914.

[5] J. CHADWICK, "Possible existence of a neutron," *Nature*, vol. 129, pp. 312–312, Feb 1932.

[6] E. Fermi, "Tentativo di una Teoria Dei Raggi β," *Il Nuovo Cimento*, vol. 11, pp. 1–19, Jan 1934.

[7] S. L. Glashow, "Partial-symmetries of weak interactions," *Nuclear Physics*, vol. 22, no. 4, pp. 579 – 588, 1961.

[8] S. Weinberg, "A model of leptons," *Physical Review Letters*, vol. 19, pp. 1264–1266, Nov 1967.

[9] B. Pontecorvo, "Inverse beta process," *Camb. Monogr. Part. Phys. Nucl. Phys. Cosmol.*, vol. 1, pp. 25–31, 1991. [,97(1946)].

[10] F. REINES and C. L. COWAN, "The neutrino," *Nature*, vol. 178, pp. 446–449, Sep 1956.

[11] G. Danby, "Observation of high-energy neutrino reactions and the existence of two kinds of neutrinos," *Physical Review Letters*, vol. 9, no. 1, pp. 36–44, 1962.

[12] K. Kodama and Others, "Observation of tau neutrino interactions," *Physics Letters B*, vol. 504, no. 3, pp. 218 – 224, 2001.

[13] M. L. Perl, "Evidence for Anomalous Lepton Production in $e^+ - e^-$ Annihilation," *Physical Review Letters*, vol. 35, no. 22, pp. 1489–1492, 1975.

[14] D. Decamp and Others, "A search for new quarks and leptons from z0 decay at lep," *Physics Letters B*, vol. 236, no. 4, pp. 511 – 522, 1990.

[15] T. A. collaboration, "Observation of a new particle in the search for the standard model higgs boson with the atlas detector at the lhc," *Physics Letters B*, vol. 716, no. 1, pp. 1 – 29, 2012.

[16] G. B. Franklin, "The KATRIN Neutrino Mass Measurement: Experiment, Status, and Outlook," in *13th Conference on the Intersections of Particle and Nuclear Physics (CIPANP 2018) Palm Springs, California, USA, May 29-June 3, 2018*, 2018.

[17] M. Aker *et al.*, "An improved upper limit on the neutrino mass from a direct kinematic method by KATRIN," 2019.

[18] B. Pontecorvo, "Neutrino Experiments and the Problem of Conservation of Leptonic Charge," *Sov. Phys. JETP*, vol. 26, pp. 984–988, 1968. [Zh. Eksp. Teor. Fiz.53,1717(1967)].

[19] Z. Maki, M. Nakagawa, and S. Sakata, "Remarks on the Unified Model of Elementary Particles," *Progress of Theoretical Physics*, vol. 28, pp. 870–880, 11 1962.

[20] K. Lande and P. Wildenhain, "The homestake chlorine solar neutrino experiment—past, present and future," *Nuclear Physics B - Proceedings Supplements*, vol. 118, pp. 49–54, Apr 2003.

[21] J. N. Abdurashitov, E. P. Veretenkin, V. M. Vermul, V. N. Gavrin, S. V. Girin, V. V. Gorbachev, P. P. Gurkina, G. T. Zatsepin, T. V. Ibragimova, A. V. Kalikhov, and et al., "Solar neutrino flux measurements by the soviet-american gallium experiment (sage) for half the 22-year solar cycle," *Journal of Experimental and Theoretical Physics*, vol. 95, pp. 181–193, Aug 2002.

[22] M. Altmann and Others, "Complete results for five years of gno solar neutrino observations," *Physics Letters B*, vol. 616, no. 3, pp. 174 – 190, 2005.

[23] Y. Suzuki, "The super-kamiokande experiment," *The European Physical Journal C*, vol. 79, Apr 2019.

[24] G. Alimonti and Others, "The borexino detector at the laboratori nazionali del gran sasso," *Nuclear Instruments and Methods in Physics Research Section A: Accelerators, Spectrometers, Detectors and Associated Equipment*, vol. 600, pp. 568–593, Mar 2009.

[25] A. Bellerive, J. Klein, A. McDonald, A. Noble, and A. Poon, "The sudbury neutrino observatory," *Nuclear Physics B*, vol. 908, pp. 30–51, Jul 2016.

[26] W. W. M. Allison *et al.*, "Measurement of the atmospheric neutrino flavor composition in Soudan-2," *Phys. Lett.*, vol. B391, pp. 491–500, 1997.

[27] G. Giacomelli, "Neutrino physics and astrophysics with the MACRO experiment at the Gran Sasso lab," *Braz. J. Phys.*, vol. 33, pp. 211–217, 2003.

[28] R. Wendell, "Atmospheric Results from Super-Kamiokande," *AIP Conf. Proc.*, vol. 1666, no. 1, p. 100001, 2015.

[29] F. An and Others, "Measurement of electron antineutrino oscillation based on 1230 days of operation of the daya bay experiment," *Physical Review D*, vol. 95, Apr 2017.

[30] S.-B. Kim, "New results from reno and prospects with reno-50," *Nuclear and Particle Physics Proceedings*, vol. 265-266, pp. 93–98, Aug 2015.

[31] J. I. Crespo-Anadón, "Double Chooz: Latest results," *Nucl. Part. Phys. Proc.*, vol. 265-266, pp. 99–104, 2015.

[32] S. Abe, T. Ebihara, S. Enomoto, K. Furuno, Y. Gando, K. Ichimura, H. Ikeda, K. Inoue, Y. Kibe, Y. Kishimoto, and et al., "Precision measurement of neutrino oscillation parameters with kamland," *Physical Review Letters*, vol. 100, Jun 2008.

[33] S. Boyd, "Recent results from the k2k (kek-to-kamioka) neutrino oscillation experiment," *Nuclear Physics B - Proceedings Supplements*, vol. 98, pp. 175–181, Apr 2001.

[34] J. Evans, "The MINOS Experiment: Results and Prospects," *Adv. High Energy Phys.*, vol. 2013, p. 182537, 2013.

[35] N. Agafonova, A. Alexandrov, A. Anokhina, S. Aoki, A. Ariga, T. Ariga, A. Bertolin, C. Bozza, R. Brugnera, A. Buonaura, and et al., "Final Results of the OPERA Experiment on $\nu\tau$ Appearance in the CNGS Neutrino Beam," *Physical Review Letters*, vol. 120, May 2018.

[36] C. Giganti, "Latest results from T2K and T2K Phase II," in *Proceedings, Prospects in Neutrino Physics (NuPhys2017): London, UK, December 20-22, 2017*, pp. 61–69, 2018.

[37] F. Jediny, "Nova latest results," *Proceedings of The 15th International Conference on Flavor Physics & CP Violation — PoS(FPCP2017)*, Oct 2017.

[38] F. Vannucci, "The nomad experiment at cern," *Advances in High Energy Physics*, vol. 2014, pp. 1–20, 2014.

[39] A. G. Cocco, "Results from CHORUS experiment at CERN," *Phys. Rept.*, vol. 307, pp. 319–324, 1998.

[40] G. Mention, M. Fechner, T. Lasserre, T. A. Mueller, D. Lhuillier, M. Cribier, and A. Letourneau, "The Reactor Antineutrino Anomaly," *Phys. Rev.*, vol. D83, p. 073006, 2011.

[41] C. Giunti and M. Laveder, "Statistical Significance of the Gallium Anomaly," *Phys. Rev.*, vol. C83, p. 065504, 2011.

[42] A. Aguilar, L. B. Auerbach, R. L. Burman, D. O. Caldwell, E. D. Church, A. K. Cochran, J. B. Donahue, A. Fazely, G. T. Garvey, R. M. Gunasingha, and et al., "Evidence for neutrino oscillations from the observation of ν_e appearance in a ν_μ beam," *Physical Review D*, vol. 64, Nov 2001.

[43] A. Strumia, "Interpreting the LSND anomaly: Sterile neutrinos or CPT violation or...?," *Phys. Lett.*, vol. B539, pp. 91–101, 2002.

[44] A. A. Aguilar-Arevalo *et al.*, "Significant Excess of ElectronLike Events in the MiniBooNE Short-Baseline Neutrino Experiment," *Phys. Rev. Lett.*, vol. 121, no. 22, p. 221801, 2018.

[45] C. Giunti and T. Lasserre, "eV-scale Sterile Neutrinos," 2019.

[46] "Sterile neutrino search at the neos experiment," *Physical Review Letters*, vol. 118, no. 12, 2017.

[47] A. P. Serebrov *et al.*, "First Observation of the Oscillation Effect in the Neutrino-4 Experiment on the Search for the Sterile Neutrino," *Pisma Zh. Eksp. Teor. Fiz.*, vol. 109, no. 4, pp. 209–218, 2019. [JETP Lett.109,no.4,213(2019)].

[48] "Sterile neutrino constraints from the stereo experiment with 66 days of reactor-on data," *Physical Review Letters*, vol. 121, no. 16, 2018.

[49] L. Manzanillas, "Performance of the SoLid Reactor Neutrino Detector," *PoS*, vol. ICHEP2018, p. 426, 2019.

[50] M. Antonello *et al.*, "A Proposal for a Three Detector Short-Baseline Neutrino Oscillation Program in the Fermilab Booster Neutrino Beam," 2015.

[51] P. A. Machado, O. Palamara, and D. W. Schmitz, "The Short-Baseline Neutrino Program at Fermilab," *Ann. Rev. Nucl. Part. Sci.*, vol. 69, 2019.

[52] C. Rubbia, "The Liquid Argon Time Projection Chamber: A New Concept for Neutrino Detectors," 1977.

[53] N. McConkey, "Sbnd: Status of the fermilab short-baseline near detector," *Journal of Physics: Conference Series*, vol. 888, p. 012148, Sep 2017.

[54] A. Machado, E. Segreto, D. Warner, A. Fauth, B. Gelli, R. Máximo, A. Pissolatti, L. Paulucci, and F. Marinho, "The x-arapuca: an improvement of the arapuca device," *Journal of Instrumentation*, vol. 13, pp. C04026–C04026, Apr 2018.

[55] R. Acciarri *et al.*, "Design and Construction of the MicroBooNE Detector," *JINST*, vol. 12, no. 02, p. P02017, 2017.

[56] P. Cennini, S. Cittolin, G. Maurin, and Others, *ICARUS II: a second-generation proton decay experiment and neutrino observatory at the Gran Sasso Laboratory : proposal. Imaging Cosmic And Rare Underground Signals II. a second-generation proton decay experiment and neutrino observatory at the Gran Sasso Laboratory : proposal.* L'Aquila: Laboratori Nazionali del Gran Sasso, 1993. Volume I : the physics programme, the results of the CERN-3-ton prototype tests.

[57] A. Fava and I. Collaboration, "Icarus-t600: Results from cngs and future perspectives," 2013.

[58] C. Farnese and on behalf of the ICARUS Collaboration, "The icarus experiment," *Universe*, vol. 5, p. 49, Jan 2019.

[59] C. Rubbia and C. S. Montanari, "Status and plans of WA104/ICARUS," Tech. Rep. CERN-SPSC-2017-012. SPSC-SR-207, CERN, Geneva, Mar 2017.

[60] Kuraray, "Wavelength shifters catalogue."

[61] Hamamatsu, "Hamamatsu 13369 sipm catalogue."

[62] M. Auger, A. Ereditato, D. Goeldi, I. Kreslo, D. Lorca, M. Luethi, C. R. v. Rohr, J. Sinclair, and M. S. Weber, "Multi-channel front-end board for sipm readout," *Journal of Instrumentation*, vol. 11, pp. P10005–P10005, Oct 2016.

[63] CAEN, "32 channel sipm readout front-end board."

[64] ZeroMQ, "http://zeromq.org."